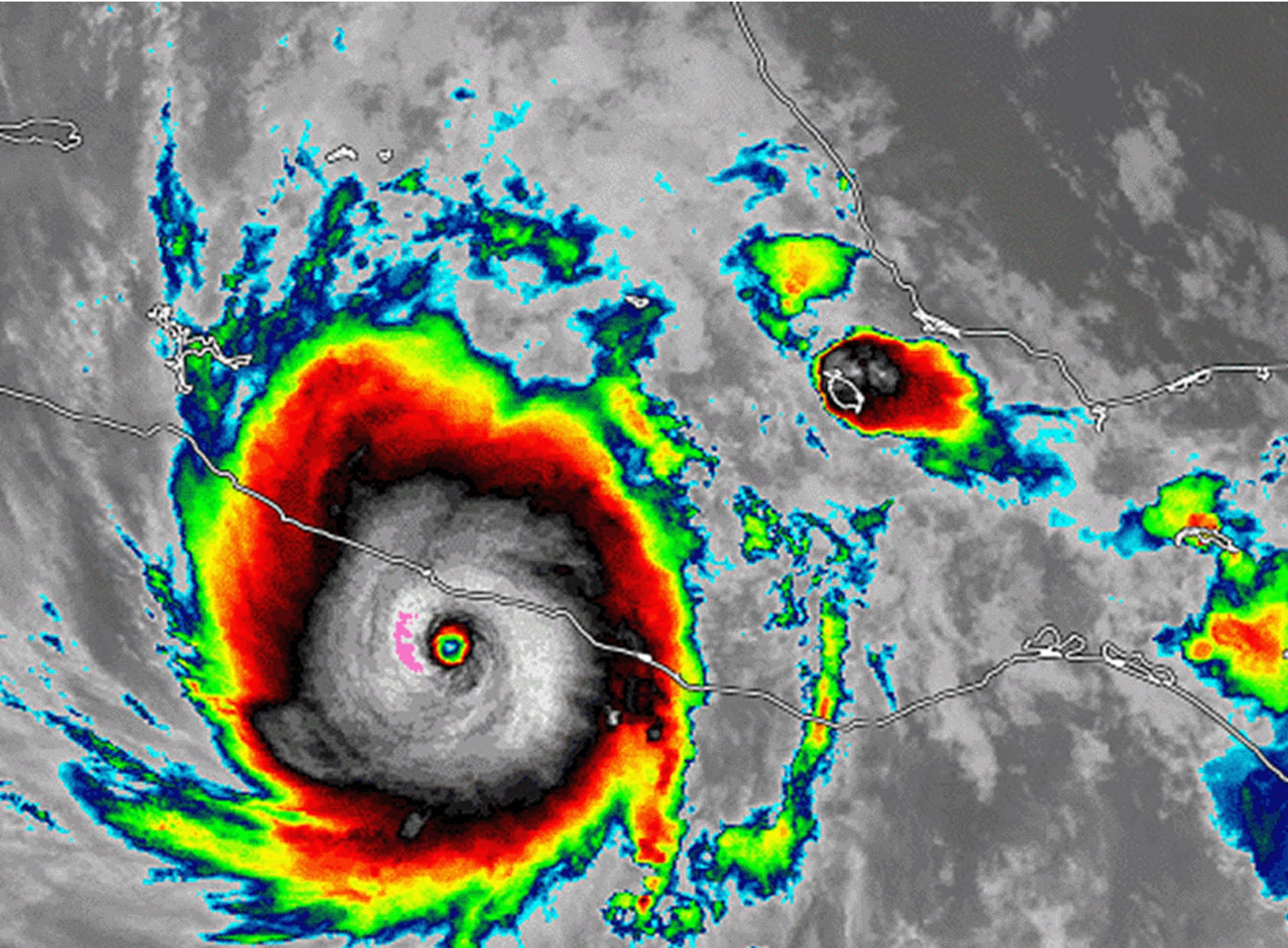# STATE OF THE CLIMATE IN 2023

THE TROPICS

H. J. Diamond and C. J. Schreck, Eds.

Special Online Supplement to the *Bulletin of the American Meteorological Society*, Vol. 105, No. 8, August 2024

STATE OF THE CLIMATE IN 2023
The Tropics

Editors

Jessica Blunden
Tim Boyer

Chapter Editors

Anthony Arguez
Josh Blannin
Peter Bissolli
Kyle R. Clem
Howard J. Diamond
Matthew L. Druckenmiller
Robert J. H. Dunn
Catherine Ganter
Nadine Gobron
Gregory C. Johnson
Rick Lumpkin
Rodney Martinez
Ademe Mekonnen
John B. Miller
Twila A. Moon
Marilyn N. Raphael
Carl J. Schreck III
Laura Stevens
Richard L. Thoman
Kate M. Willett
Zhiwei Zhu

Technical Editor

Lukas Noguchi

BAMS Special Editor for Climate

Timothy DelSole

American Meteorological Society

Cover Credit:

Hurricane Otis 25 October 2023

Hurricane Otis experienced extremely rapid intensification in the 12 hours before it made landfall near Acapulco, Mexico, as a Category 5 storm on 25 October 2023.

Imagery courtesy of CIMSS - Cooperative Institute for Meteorological Satellite Studies, University of Wisconsin-Madison

Editor and Author Affiliations (alphabetical by name)

Allgood, Adam, NOAA/NWS National Centers for Environmental Prediction Climate Prediction Center, College Park, Maryland

Becker, Emily J., Rosenstiel School of Marine and Atmospheric Science, University of Miami, Miami, Florida

Blake, Eric S., NOAA/NWS National Hurricane Center, Miami, Florida

Bringas, Francis G., NOAA/OAR Atlantic Oceanographic and Meteorological Laboratory, Miami, Florida

Camargo, Suzana J., Lamont-Doherty Earth Observatory, Columbia University, Palisades, New York

Cerveny, Randall, Department of Geography, Arizona State University, Tempe, Arizona

Chen, Lin, Institute for Climate and Application Research (ICAR)/KLME/ILCEC/CIC-FEMD, Nanjing University of Information Science and Technology, Nanjing, China

Coelho, Caio A.S., Centro de Previsão do Tempo e Estudos Climáticos/National Institute for Space Research, Center for Weather Forecasts and Climate Studies, Cachoeira Paulista, Brazil

Diamond, Howard J., NOAA/OAR Air Resources Laboratory, College Park, Maryland

Earl-Spurr, Craig, Bureau of Meteorology, Perth, Australia

Fauchereau, Nicolas, National Institute of Water and Atmospheric Research, Ltd., Auckland, New Zealand

Fogarty, Chris, Canadian Hurricane Centre, Dartmouth, Canada

Goldenberg, Stanley B., NOAA/OAR Atlantic Oceanographic and Meteorological Laboratory, Miami, Florida

Harnos, Daniel S., NOAA/NWS National Centers for Environmental Prediction Climate Prediction Center, College Park, Maryland

He, Qiong, Earth System Modeling Center, Nanjing University of Information Science and Technology, Nanjing, China

Hu, Zeng-Zhen, NOAA/NWS National Centers for Environmental Prediction Climate Prediction Center, College Park, Maryland

Klotzbach, Philip J., Department of Atmospheric Science, Colorado State University, Fort Collins, Colorado

Knaff, John A., NOAA/NESDIS Center for Satellite Applications and Research, Fort Collins, Colorado

Kumar, Arun, NOAA/NWS National Centers for Environmental Prediction Climate Prediction Center, College Park, Maryland

L'Heureux, Michelle, NOAA/NWS National Centers for Environmental Prediction Climate Prediction Center, College Park, Maryland

Landsea, Chris W., NOAA/NWS National Hurricane Center, Miami, Florida

Lin, I-I, National Taiwan University, Taipei, Taiwan

Lopez, Hosmay, NOAA/OAR Atlantic Oceanographic and Meteorological Laboratory, Miami, Florida

Lorrey, Andrew M., National Institute of Water and Atmospheric Research, Ltd., Auckland, New Zealand

Luo, Jing-Jia, Institute for Climate and Application Research, Nanjing University of Information Science and Technology, Nanjing, China

Magee, Andrew D., Centre for Water, Climate and Land, School of Environmental and Life Sciences, University of Newcastle, Callaghan, Australia

Pasch, Richard J., NOAA/NWS National Hurricane Center, Miami, Florida

Paterson, Linda, Bureau of Meteorology, Perth, Australia

Pezza, Alexandre B., Greater Wellington Regional Council, Wellington, New Zealand

Rosencrans, Matthew, NOAA/NWS National Centers for Environmental Prediction Climate Prediction Center, College Park, Maryland

Schreck, Carl J., Cooperative Institute for Satellite Earth System Studies, North Carolina State University, Asheville, North Carolina

Trewin, Blair C., Bureau of Meteorology, Melbourne, Australia

Truchelut, Ryan E., WeatherTiger, Tallahassee, Florida

Uehling, John, Cooperative Institute for Satellite Earth System Studies, North Carolina State University, Asheville, North Carolina

Wang, Bin, School of Ocean and Earth Science and Technology, Department of Meteorology, University of Hawaii at Manoa, Honolulu, Hawaii; International Pacific Research Center, Honolulu, Hawaii

Wang, Hui, NOAA/NWS National Centers for Environmental Prediction Climate Prediction Center, College Park, Maryland

Wood, Kimberly M., Department of Hydrology and Atmospheric Sciences, University of Arizona, Tucson, Arizona

Editorial and Production Team

Allen, Jessicca, Graphics Support, Cooperative Institute for Satellite Earth System Studies, North Carolina State University, Asheville, North Carolina

Camper, Amy V., Graphics Support, Innovative Consulting and Management Services, LLC, NOAA/NESDIS National Centers for Environmental Information, Asheville, North Carolina

Haley, Bridgette O., Graphics Support, NOAA/NESDIS National Centers for Environmental Information, Asheville, North Carolina

Hammer, Gregory, Content Team Lead, Communications and Outreach, NOAA/NESDIS National Centers for Environmental Information, Asheville, North Carolina

Love-Brotak, S. Elizabeth, Lead Graphics Production, NOAA/NESDIS National Centers for Environmental Information, Asheville, North Carolina

Ohlmann, Laura, Technical Editor, Innovative Consulting and Management Services, LLC, NOAA/NESDIS National Centers for Environmental Information, Asheville, North Carolina

Noguchi, Lukas, Technical Editor, Innovative Consulting and Management Services, LLC, NOAA/NESDIS National Centers for Environmental Information, Asheville, North Carolina

Riddle, Deborah B., Graphics Support, NOAA/NESDIS National Centers for Environmental Information, Asheville, North Carolina

Veasey, Sara W., Visual Communications Team Lead, Communications and Outreach, NOAA/NESDIS National Centers for Environmental Information, Asheville, North Carolina

3. Table of Contents

4. THE TROPICS

H. J. Diamond and C. J. Schreck, Eds.

a. Overview

—H. J. Diamond and C. J. Schreck

In 2023, the El Niño–Southern Oscillation (ENSO) transitioned to El Niño after three years of La Niña conditions. ENSO-neutral conditions were briefly present in the tropical Pacific between January–March and March–May, before El Niño conditions emerged in April–June. El Niño strengthened steadily through the second half of 2023, with the Oceanic Niño Index reaching a value of +1.9°C in October–December.

For the global tropics (defined here as 20°S–20°N), the NOAA Merged Land Ocean Global Surface Temperature Analysis (NOAA GlobalTemp; Vose et al. 2021) indicates that the combined average land and ocean surface temperature was 0.5°C above the 1991–2020 average, the warmest year for the tropics in the 174-year data record. The six warmest years in the tropics since 1850 have all occurred since 2015. Data from the Global Precipitation Climatology Project indicate a mean annual total precipitation value of 1318 mm across the tropics (20°S–20°N latitude band) over land. This is 86 mm below the 1991–2020 average and was the third lowest for the 1979–2023 period of record.

Globally, 82 named tropical cyclones (TCs; ≥34 kt; or ≥17 m s⁻¹) were observed during the 2023 Northern Hemisphere season (January–December 2023) and the 2022/23 Southern Hemisphere season (July–June 2022/23; see Table 4.2), as documented by the National Hurricane Center and the Joint Typhoon Warning Center in International Best Track Archive for Climate Stewardship Version 4 (Knapp et al. 2010). Overall, this number was below the 1991–2020 global average of 87 TCs and also below the 85 TCs reported during the 2022 season (Diamond and Schreck 2023). The record for most named storms in a single TC season is 104 in 1992.

Of the 82 named storms, 45 reached hurricane strength (one-minute maximum sustained winds ≥64 kt) and 30 reached major hurricane strength (one-minute maximum winds ≥96 kt). Both of these counts were below their 1991–2020 averages. The accumulated cyclone energy (ACE; an integrated metric of the strength, frequency, and duration of tropical storms and hurricanes; Bell et al. 2000) rebounded from the lowest on record in 2022 (since reliable data began in 1981) to an above-normal level in 2023. Four of the seven TC basins were above normal in 2023 in contrast to zero in 2022. The North Indian Ocean had its second highest ACE on record behind 2019, and the North Atlantic had its seventh above-normal season in the last eight years. The western North Pacific had its fourth consecutive season with below-normal activity. A total of seven storms reached Category 5 intensity on the Saffir-Simpson Hurricane Wind Scale (one-minute maximum sustained winds ≥137 kt) during 2023, compared with only three in 2022. All of the basins, except for the Australian and southwest Pacific, had at least one Category 5 storm.

The 20 named storms in the North Atlantic during 2023 was equal with 1933 for the fourth-highest total in the HURDAT2 database (Landsea and Franklin 2013). In contrast, the number of hurricanes and major hurricanes were at their long-term (1991–2020) average of seven and three, respectively. The 2023 hurricane season was classified by NOAA as an above-normal season.

NOAA uses 1951–2020 terciles of ACE to delineate below-normal, normal, and above-normal seasons, and 2023's ACE of 146×10^4 kt^2 places it in the upper tercile. Two storms of particular note this season were Hurricane Otis, which was the strongest landfalling hurricane on record for the west coast of Mexico (see Sidebar 4.1), and Cyclone Freddy in the Southern Hemisphere (see Sidebar 4.2). Freddy is now recognized as the world's longest-lived TC (Earl-Spur et. al. 2024), crossing the full width of the Indian Ocean. Freddy is the first TC since 2000 to form in the Australian region and make landfall on the mainland African coast. Freddy made a total of three landfalls: one in Madagascar and two in Mozambique.

b. ENSO and the tropical Pacific

—E. Becker, M. L'Heureux, Z.-Z. Hu, and A. Kumar

The El Niño–Southern Oscillation (ENSO) is an ocean and atmosphere-coupled climate phenomenon across the tropical Pacific Ocean, with its warm (cold) phases called El Niño (La Niña). NOAA's Climate Prediction Center classifies and assesses the strength and duration of El Niño and La Niña events using the Oceanic Niño Index (ONI, shown for mid-2022 through 2023 in Fig. 4.1). The ONI is the three-month (seasonal) running average of sea-surface temperature (SST) anomalies in the Niño-3.4 region (5°S–5°N, 170°W–120°W), currently calculated as the departure from the 1991–2020 base period mean[1]. El Niño is classified when the ONI is at or greater than +0.5°C for at least five consecutive, overlapping seasons, while La Niña is classified when the ONI is at or less than −0.5°C for at least five consecutive, overlapping seasons.

The time series of the ONI (Fig. 4.1) shows a transition from 2022's La Niña conditions—the third La Niña year in a row—to strong El Niño in 2023, where strong El Niño is defined in this chapter as ONI ≥1.5°C. La Niña developed in July–September 2020 and lasted nearly continuously through December–February (DJF) 2022/23, with a brief period of ENSO-neutral conditions in the summer of 2021. ENSO-neutral conditions were briefly present in the tropical Pacific in 2023, between January–March and March–May (MAM), before El Niño emerged in April–June. El Niño strengthened steadily through the second half of 2023, with the ONI reaching a value of +1.9°C in October–December.
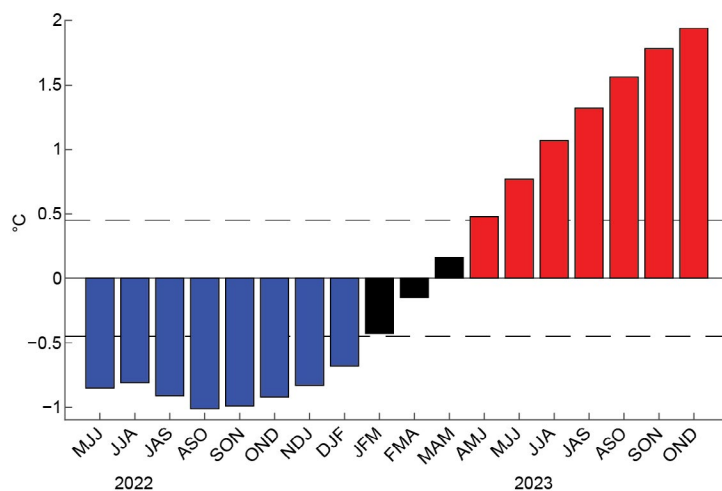

Fig. 4.1. Time series of the Oceanic Niño Index (ONI, °C) from mid-2022 through 2023. Overlapping three-month seasons are labeled on the x-axis, with initials indicating the first letter of each month in the season. Blue bars indicate negative values that are less than –0.5°C. Black bars indicate values between –0.5°C and 0.5°C, while red bars indicate positive values greater than 0.5°C. ONI values are derived from the ERSSTv5 dataset and are based on departures from the 1991–2020 period monthly means (Huang et al. 2017).

1. OCEANIC CONDITIONS

Figure 4.2 displays the mean SST (left column) and SST anomalies (right column) during DJF 2022/23 through September–November (SON) 2023. During DJF, below-average SST anomalies were on the order of –0.5°C to –1.0°C across the central equatorial Pacific (approximately 170°E–260°E), reflecting a weak and waning La Niña (Fig. 4.2b). During MAM, a small region of SST anomalies exceeding +2.5°C developed off the coast of Peru and Ecuador, while most of the tropical Pacific was near average, with a slight positive anomaly (+0.5°C to +1.0°C) in the western Pacific (Fig. 4.2d). By June–August (JJA), positive anomalies spread westward along the equator, with western Pacific SSTs closer to average (Fig. 4.2f). The SST pattern in SON reflects a strong El Niño, with equatorial Pacific anomalies in excess of +1.0°C extending from the dateline to the coast of South America (Fig. 4.2h). Some weak off-equatorial negative SST anomalies in the eastern half of the tropical basin were present from MAM through SON (Figs. 4.2d,f,h). Also of note in SON 2023 was the positive phase of the Indian Ocean dipole (IOD), with negative SST anomalies in the east and positive SST anomalies in the west (Fig. 4.2h).

---

[1] The ONI is an index measuring ENSO, and to highlight its seasonal-to-interannual component, the base period is updated every five years with a rolling 30-year climatology. SSTs in the Niño3.4 region have multi-decadal and longer trends going back to 1950 or earlier. The rolling climatology reduces the influence of trend on the state of ENSO.
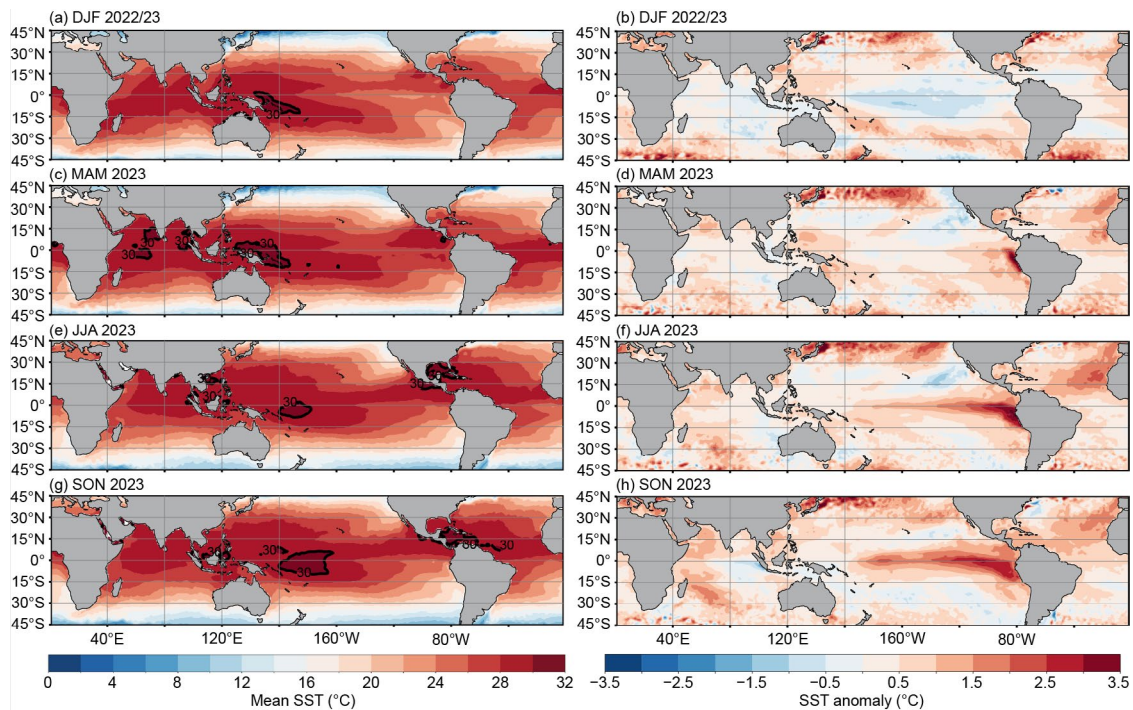
Fig. 4.2. Mean sea-surface temperatures (SSTs; left) and SST anomalies (right) for (a),(b) Dec–Feb (DJF) 2022/23, (c),(d) Mar–May (MAM) 2023, (e),(f) Jun–Aug (JJA) 2023, and (g),(h) Sep–Nov (SON) 2023. The bold contour for SST is for 30°C. Anomalies are departures from the 1991–2020 seasonal adjusted OIv2.1 climatology (Huang et al. 2021).

The weakening La Niña of DJF 2022/23 is also reflected in the subsurface temperature anomalies (Fig. 4.3a). The subsurface temperatures in the eastern Pacific were slightly below average, with a slightly shoaled thermocline. Warm anomalies in the west contributed to a deeper-than-average thermocline, leading to a slightly deeper-than-average west–east thermocline slope (Fig. 4.3a). During the transition from La Niña to El Niño in MAM, the thermocline across the entire basin was deeper than average (Fig, 4.3b). As El Niño strengthened into JJA and SON 2023, the depth of the thermocline in the western Pacific returned to near-average. In the central and eastern equatorial Pacific, the thermocline deepened as warm subsurface anomalies expanded in the central and eastern equatorial Pacific. The slope of the thermocline across the equatorial Pacific was shallower than average during the last half of the year (Figs. 4.3c,d). Overall, the subsurface SST in the western Pacific was warmer than would be expected during strong El Niño events (e.g., Kumar and Hu 2014).

Fig 4.3. Equatorial depth–longitude section of Pacific Ocean temperature anomalies (°C) averaged between 5°S and 5°N during (a) Dec–Feb (DJF) 2022/23, (b) Mar–May (MAM) 2023, (c) Jun–Aug (JJA) 2023, and (d) Sep–Nov (SON) 2023. The 20°C isotherm (thick solid line) approximates the center of the oceanic thermocline. The gray dashed line shows the climatology of the 20°C isotherm based on the 1991–2020 mean. The data are derived from a reanalysis system that assimilates oceanic observations into an oceanic general circulation model (Behringer 2007). Anomalies are departures from the 1991–2020 period monthly means.

2. ATMOSPHERIC CIRCULATION

December–February 2022/23 featured large-scale tropical atmospheric circulation anomalies consistent with La Niña. During La Niña, convection is typically suppressed (positive outgoing longwave radiation [OLR] anomalies, brown shading) over the western and central tropical Pacific and enhanced (negative OLR anomalies, green shading) over the Maritime Continent (Fig. 4.4a). This pattern mostly dissipated by MAM 2023, as ENSO-neutral conditions returned to the tropical Pacific (Fig. 4.4b). Near coastal South America, where strongly above-average SSTs were present, rainfall was enhanced during MAM. By JJA, El Niño's expected atmospheric circulation pattern, with enhanced convection (green) over the warmer waters of the central/eastern Pacific and suppressed convection (brown) over the Maritime Continent, indicated a reduced Walker circulation (Fig. 4.4c). Just north of the equator, enhanced convection stretched from the dateline to the coast of South America. The anomalous dipole of suppressed convection in the western Pacific and enhanced convection in the central and eastern Pacific strengthened in SON (Fig. 4.4d). The positive IOD was also evident in a region of strongly suppressed convection in the central and eastern Indian Ocean (Fig. 4.4d).

Similar to convection, the lower- and upper-level wind anomalies showed the transition from La Niña in DJF to neutral in MAM to El Niño in JJA and SON. The tropical low-level 850-hPa easterly trade winds were enhanced across most of the equatorial Pacific Ocean in DJF 2022/23 (Fig. 4.5a). In MAM, the lack of a coherent low-level wind anomaly pattern reflected ENSO-neutral (Fig. 4.5b). This lack of coherence continued into JJA, despite a developing El Niño and weak convection pattern (Fig. 4.4c). By SON, the low-level trade winds slowed, exhibiting seasonally
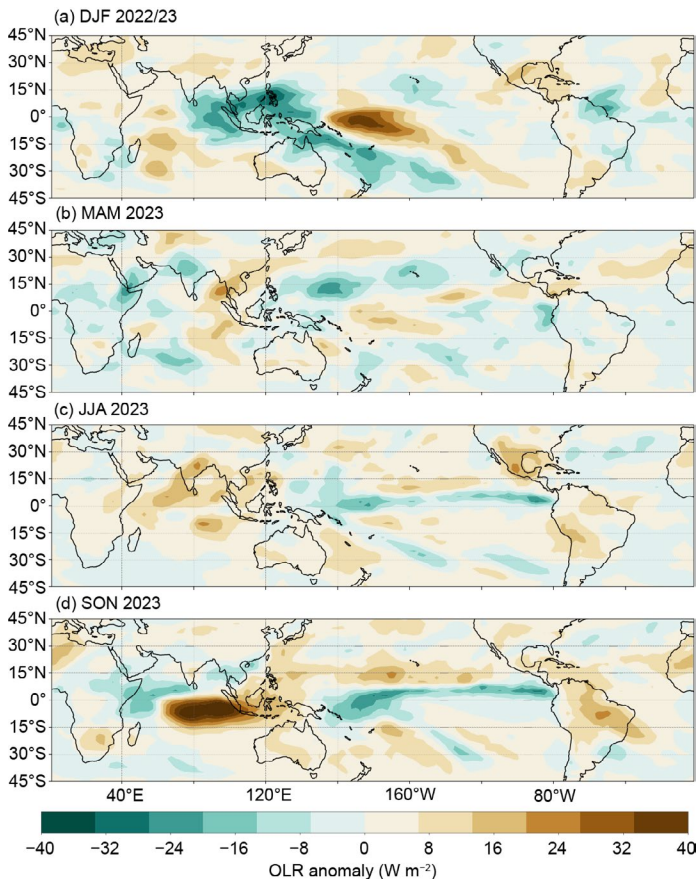
Fig. 4.4. Outgoing longwave radiation (OLR) anomalies (W m⁻²) during (a) Dec–Feb (DJF) 2022/23, (b) Mar–May (MAM) 2023, (c) Jun–Aug (JJA) 2023, and (d) Sep–Nov (SON) 2023. Anomalies are departures from the 1991–2020 period monthly means. Data are from Liebmann and Smith (1996).

Fig. 4.5. Anomalous 850-hPa wind vectors (m s⁻¹, arrows) and zonal wind speed (m s⁻¹, shading) during (a) Dec–Feb (DJF) 2022/23, (b) Mar–May (MAM) 2023, (c) Jun–Aug (JJA) 2023, and (d) Sep–Nov (SON) 2023. The reference wind vector is located on the bottom left. Anomalies are departures from the 1991–2020 period monthly means. Data are from the National Centers for Environmental Prediction (NCEP) National Center for Atmospheric Research (NCAR) reanalysis (Kalnay et al. 1996).

averaged westerly anomalies along the equatorial Pacific (Fig. 4.5d).

Reflecting La Niña, upper-level (200-hPa) westerly wind anomalies also prevailed over most of the equatorial Pacific Ocean during DJF 2022/23 (Fig. 4.6a). Upper-level westerly anomalies persisted over much of the central and eastern Pacific through MAM (Fig. 4.6b), but diminished by JJA when weak easterly anomalies developed over the central Pacific (Fig. 4.6c). Easterly upper-level wind anomalies, expected during El Niño and its associated weaker Walker circulation, were more widespread and noticeable in SON 2023 (Fig. 4.6d).

Collectively, these oceanic and atmospheric anomalies reflected the well-known, basin-wide atmospheric and oceanic coupling of ENSO (Bjerknes 1969). Overall, the atmospheric circulation reflected the transition from La Niña early in the year to a strong El Niño by the end of 2023.

3. GLOBAL PRECIPITATION

ENSO-driven teleconnections can affect precipitation anomalies globally (Bjerknes 1969; Ropelewski and Halpert 1989). While a rigorous attribution is beyond the scope of this chapter, some precipitation anomalies during JJA and SON 2023 that resemble the expected ENSO teleconnection impacts can be identified. In JJA, drier-than-average conditions were evident across eastern Australia (with some stations recording less than 25% of their average precipitation) and through

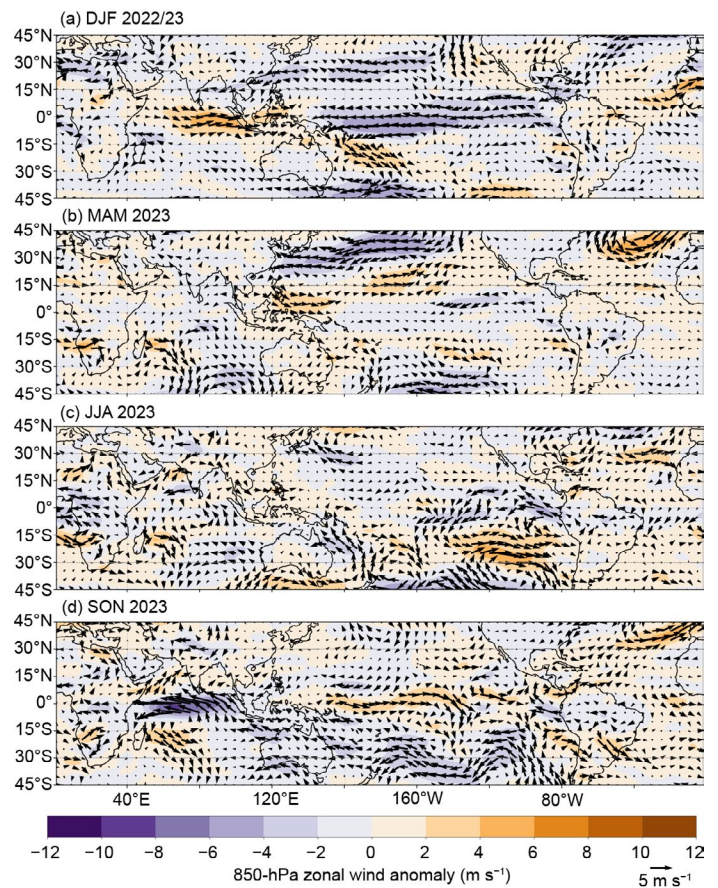**Fig. 4.6. Anomalous 200-hPa wind vectors (m s⁻¹, arrows) and zonal wind speed (m s⁻¹, shading) during (a) Dec–Feb (DJF) 2022/23, (b) Mar–May (MAM) 2023, (c) Jun–Aug (JJA) 2023, and (d) Sep–Nov (SON) 2023. The reference wind vector is located on the bottom left. Anomalies are departures from the 1991–2020 period monthly means. Data are from the National Centers for Environmental Prediction (NCEP) National Center for Atmospheric Research (NCAR) reanalysis (Kalnay et al. 1996).**

central America and northern South America (Fig. A4.1a). Many stations in India recorded below-average precipitation, although some were above average. Drier-than-average conditions continued in eastern Australia and central America in SON 2023 (Fig. A4.1b). Also in SON 2023, stations in southern Brazil and Uruguay observed positive precipitation anomalies.
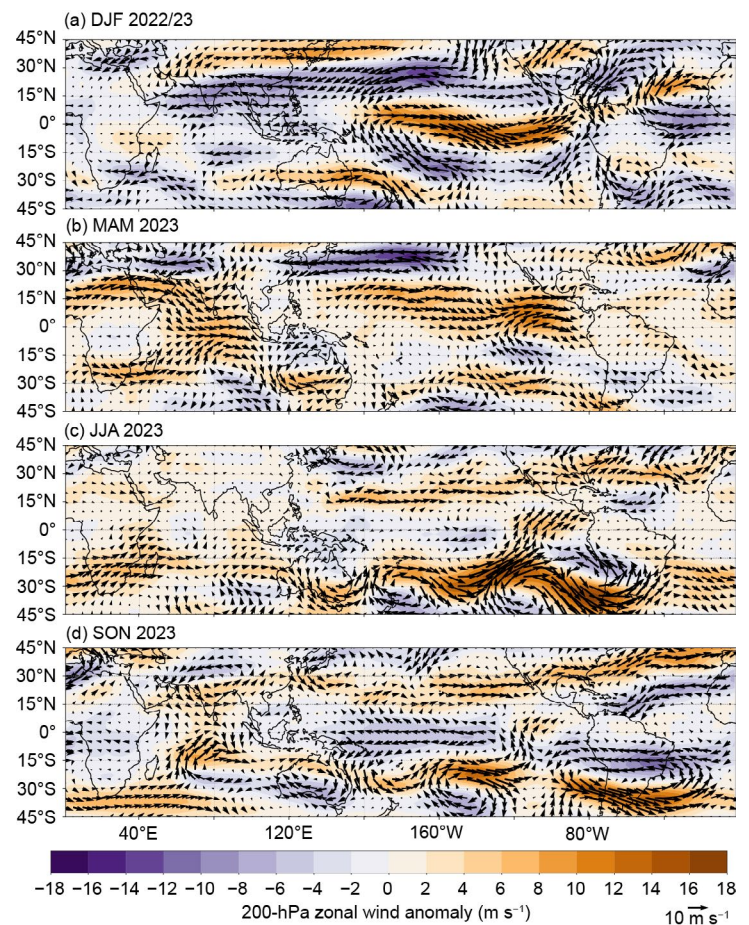
c. Tropical intraseasonal activity

—A. Allgood and C. J. Schreck

Organized tropical intraseasonal activity is modulated by several different modes of coherent atmospheric variability, most notably the Madden-Julian Oscillation (MJO; Madden and Julian 1971, 1972, 1994; Zhang 2005). The MJO is characterized by eastward-propagating envelopes of large-scale anomalous enhanced and suppressed convection that typically circumnavigate the globe in a 30-to-60-day period. MJO-related convective anomalies are similar in spatial extent to those generated by the atmospheric response to the El Niño–Southern Oscillation (ENSO), but the latter signal remains largely stationary and lasts for several months. Other impactful modes of variability include convectively-coupled atmospheric waves, such as Kelvin waves (which exhibit a faster phase speed than the MJO), and westward propagating equatorial Rossby waves (Wheeler and Kiladis 1999; Kiladis et al. 2009). These waves are typically narrower (zonally) than the MJO and may not couple as well to the broader convective regime. The MJO can be identified through time–longitude analyses of various atmospheric fields, including anomalous 200-hPa velocity potential (Fig. 4.7b), anomalous zonal winds at 200 hPa and 850 hPa (Fig. 4.8a), and anomalous outgoing longwave radiation (OLR; Fig. 4.7a). Another diagnostic tool frequently used to identify MJO activity is the Wheeler-Hendon (2004) Real-time Multivariate MJO (RMM) index. In RMM plots, robust atmospheric anomalies on a spatial scale resembling the MJO appear as a signal outside of the unit circle (Fig. 4.9). Eastward propagation is represented by counter-clockwise looping of the index about the origin.

The rapid transition from La Niña to emerging El Niño conditions that commenced during the first half of 2023 was partly facilitated by periods of strong MJO activity. The MJO was active at the beginning of 2023, with the enhanced convective phase crossing the Pacific (Figs. 4.7, 4.9a). While destructive interference between this intraseasonal signal and the ongoing La Niña
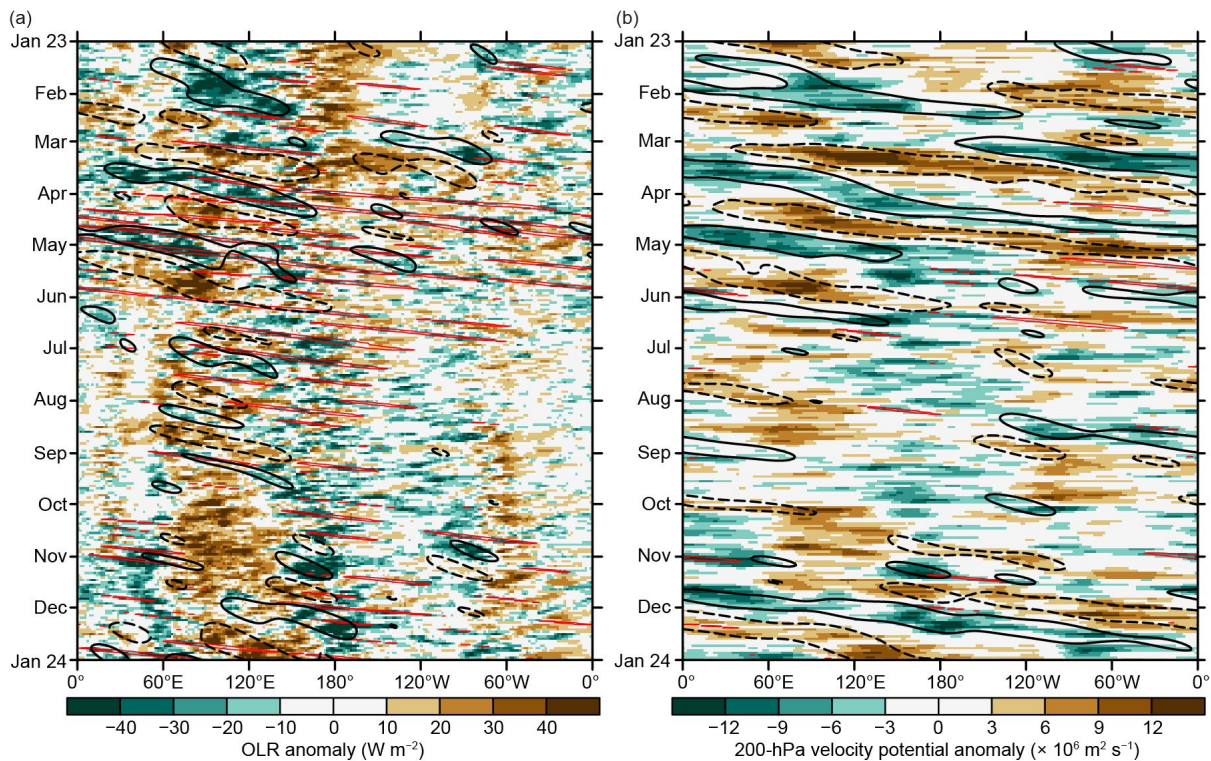
Fig. 4.7. Time–longitude section with (a) outgoing longwave radiation (OLR) anomalies (W m^{-2}; Schreck et al. 2018) and (b) 200-hPa velocity potential anomalies (× 10^6 m^2 s^{-1}) from the Climate Forecast System Reanalysis (Saha et al. 2014). Both variables are averaged over 10°S–10°N. Time increases downward on this graph, beginning with Jan 2023 at the top and ending with Jan 2024 at the bottom. Negative anomalies indicate enhanced convection, and positive anomalies indicate suppressed convection. Contours identify anomalies filtered for the Madden-Julian Oscillation (black) and atmospheric Kelvin waves (red). Contours are drawn at ±12 W m^{-2} and ±4 × 10^6 m^2 s^{-1} with the enhanced (suppressed) convective phase of these phenomena indicated by solid (dashed) contours. Anomalies are departures from the 1991–2020 base period daily means.

prevented the development of widespread equatorially focused convection, a low-level westerly wind burst was observed (Fig. 4.8a). This westerly wind burst helped generate a downwelling oceanic Kelvin wave that reduced the extent of below-average upper-oceanic heat content across the central and eastern Pacific (Fig. 4.8b). MJO activity persisted during February, with the signal generally constructively interfering with the cold ENSO base state as the enhanced convective phase crossed the Maritime Continent and the suppressed phase crossed the Pacific and Western Hemisphere. During late February and March, the MJO achieved a major disruption of the La Niña base state as it re-entered the Pacific, evidenced by an almost off-the-chart amplitude of the RMM-based MJO index in phases 7 and 8 (Fig. 4.9a). A strong, equatorially centered westerly wind burst generated a much stronger downwelling oceanic Kelvin wave in March than was generated during the January event. This rapid transport of warm ocean water from the anomalously warm West Pacific Warm Pool to the eastern Pacific brought an end to La Niña conditions. An active MJO signal persisted from April through early June (Fig. 4.9b), helping to reinforce the rapid transition away from La Niña conditions across the equatorial Pacific and setting the stage for the emerging El Niño.

El Niño conditions emerged during June, and MJO activity weakened during the boreal summer and autumn months as the low-frequency base state became the dominant driver of global tropical convective anomalies (Figs. 4.7a, 4.9c). Intraseasonal activity during this period was primarily associated with other modes, including Kelvin waves and Rossby waves. By boreal spring, a strong positive Indian Ocean dipole (IOD) event emerged, providing a secondary stationary signal that largely disrupted coherent MJO activity. The IOD activity was apparent in the MJO diagnostic figures primarily as strong low-level easterlies across the eastern Indian Ocean (Fig. 4.8a) and the RMM-based MJO index showing persistence in phases 8 and 1 during October (Fig. 4.9d).
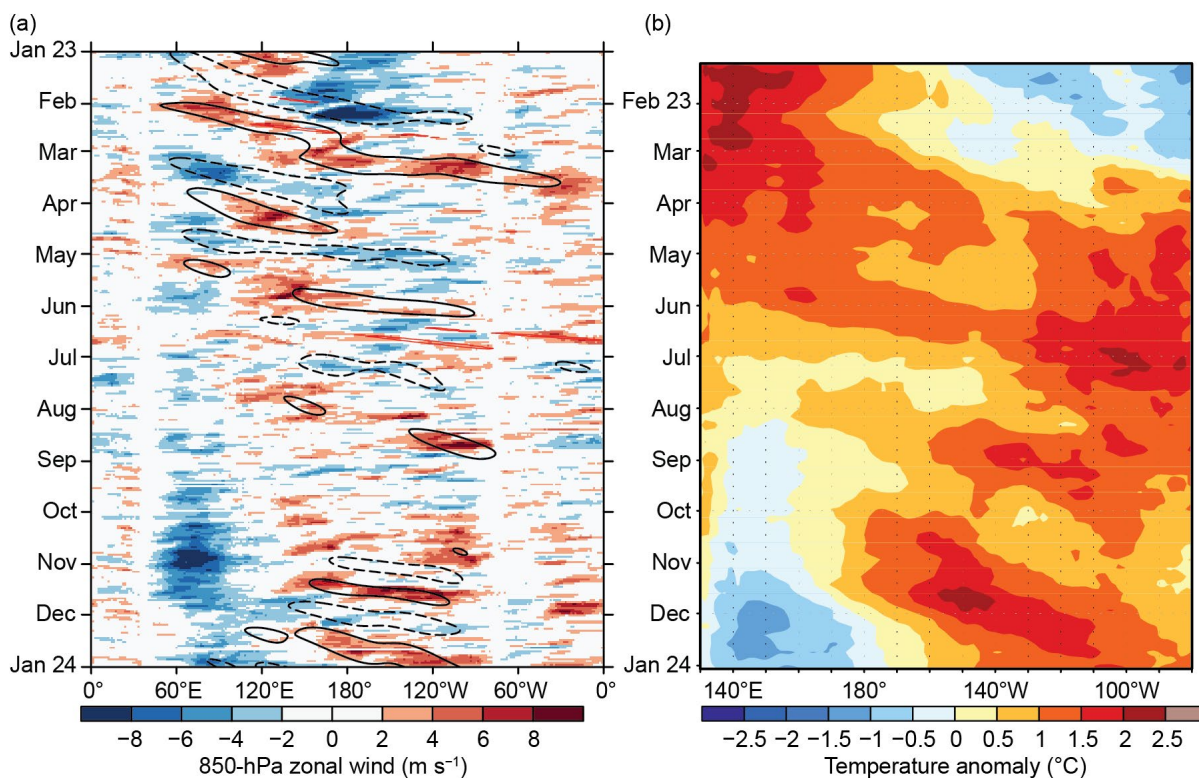
Fig. 4.8. (a) Time–longitude section for 2023 of anomalous 850-hPa zonal wind (m s⁻¹) averaged over 10°S–10°N. Contours identify anomalies filtered for the Madden-Julian Oscillation (black). (b) Time–longitude section for 2023 of the anomalous equatorial Pacific Ocean heat content, calculated as the mean temperature anomaly (°C) between 0-m and 300-m depth. Yellow/red (blue) shading indicates above- (below-) average heat content. Anomalies are departures from the 1991–2020 base period pentad means. Data in (b) are derived from an analysis system that assimilates oceanic observations into an oceanic general circulation model (Behringer et al. 1998).

Despite the increasing maturity of the El Niño event and the ongoing strong IOD in November and December, both of which typically degrade MJO propagation, robust MJO activity initiated in November, triggering an unusually strong low-level westerly wind burst over the equatorial West Pacific. The signal strengthened over the Western Hemisphere, circumnavigating the globe in approximately 40 days and triggering additional strong westerly wind bursts across the Pacific during the latter half of December. While El Niño-related SST anomalies were strongest across the central and eastern Pacific, positive SST anomalies remained in place across the West Pacific Warm Pool region despite the repeated downwelling oceanic Kelvin wave events. This unusual structure may have aided in continued MJO propagation, allowing strong convection to develop over the far western Pacific region.
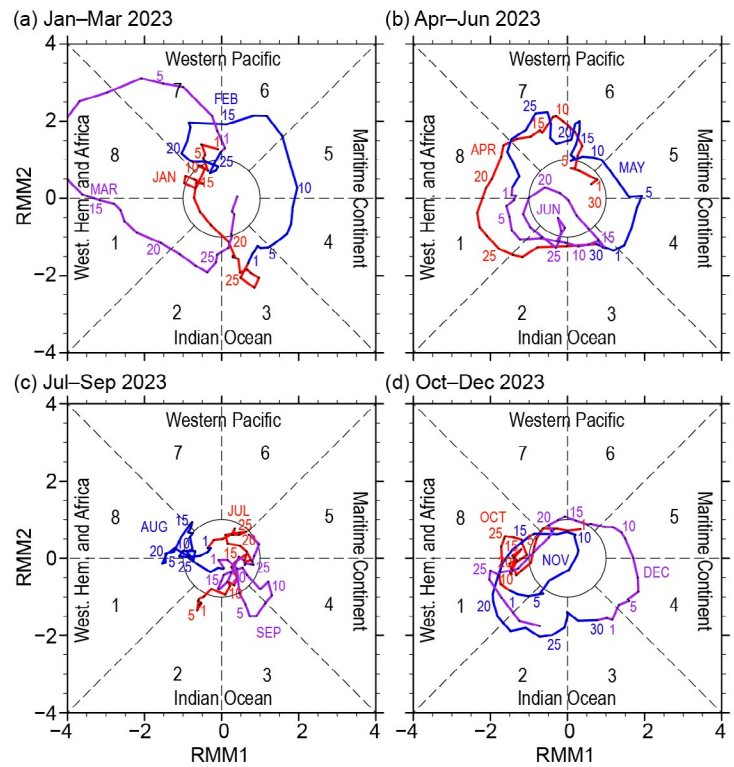
Fig. 4.9. Wheeler and Hendon (2004) Real-time Multivariate (RMM) index for (a) Jan–Mar, (b) Apr–Jun, (c) Jul–Sep, and (d) Oct–Dec 2023. Each point represents the Madden-Julian Oscillation (MJO) amplitude and location on a given day, and the connecting lines illustrate its propagation. The MJO amplitude as diagnosed by the RMM was so strong that it went off the plot in March. Amplitude is indicated by distance from the origin, with points inside the unit circle representing weak or no MJO. The eight phases around the origin identify the region experiencing enhanced convection, and counter-clockwise movement is consistent with eastward propagation.

d. Intertropical convergence zones
1. PACIFIC
N. Fauchereau

Tropical Pacific rainfall patterns are dominated by two convergence zones: the Intertropical Convergence Zone (ITCZ; Schneider et al. 2014) north of the equator and the South Pacific Convergence Zone (SPCZ; Vincent 1994) in the southwest Pacific. The position and intensity of these convergence zones throughout the year are highly sensitive to sea-surface temperature anomalies (SSTAs) and, therefore, the state of the El Niño–Southern Oscillation (ENSO; Trenberth 1984). During the course of 2023, the Pacific region underwent a transition from weak La Niña conditions to a strong El Niño. These dramatic changes in SSTAs were reflected in rainfall patterns, driven by significant changes in the position and intensity of the ITCZ and SPCZ.

Figure 4.10 summarizes the behavior for both convergence zones during 2023 using rainfall from the Multi-Source Weighted-Ensemble Precipitation (MSWEP) 2.8.0 dataset (Beck et al. 2019). Rainfall transects over 30°S to 20°N are presented for each quarter of the year, averaged across successive 30-degree longitude bands, starting in the western Pacific at 150°E–180°E. The 2023 seasonal variations are compared against the longer-term 1991–2020 climatology.
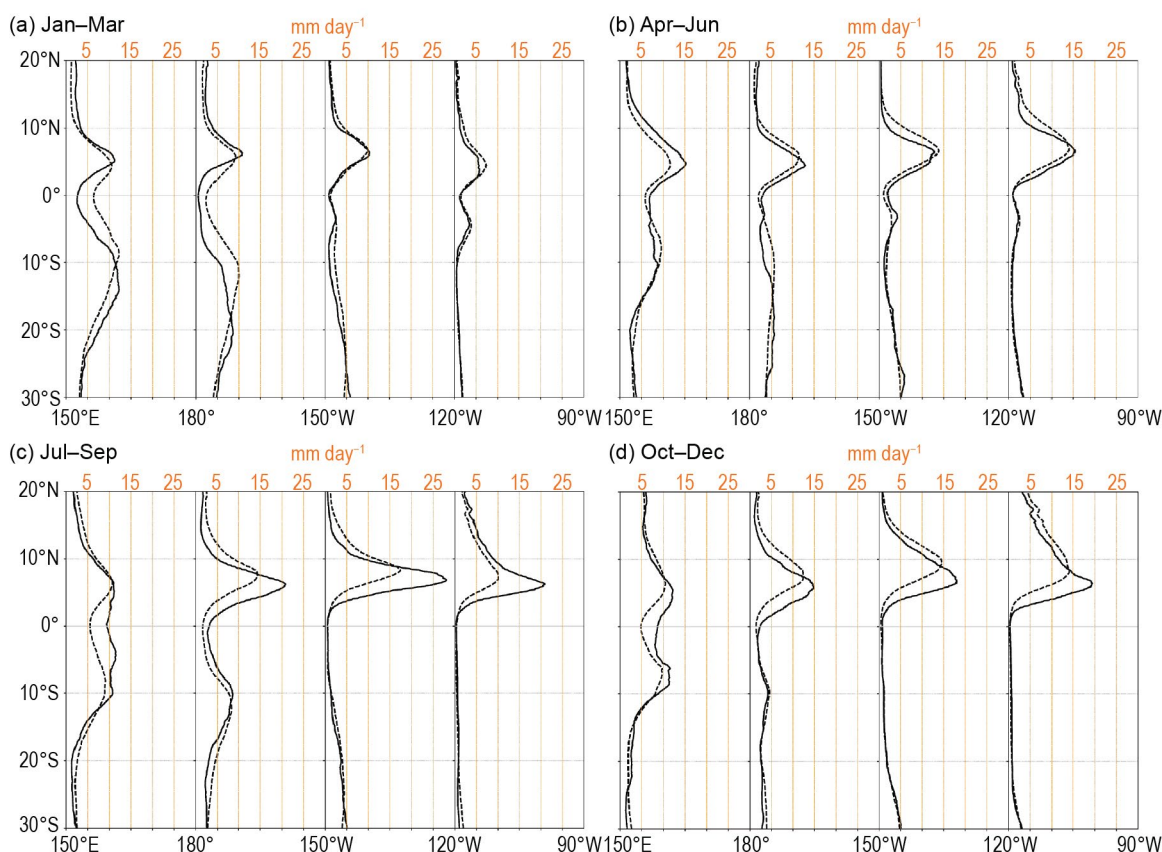
Fig. 4.10. Rainfall rate (mm day⁻¹) for (a) Jan–Mar, (b) Apr–Jun, (c) Jul–Sep, and (d) Oct–Dec 2023. The separate panels for each quarter show the 2023 rainfall latitudinal cross-section between 30°S and 20°N (solid line) and the 1991–2020 climatology (dotted line), separately for four 30° sectors from 150°E–180 to 120°W–90°W. (Source: MSWEP v2.8.0.)

The transects for January–March (Fig. 4.10a) for the western and central Pacific (150°E–150°W, especially from 150°E to the dateline) show that at the beginning of 2023, the SPCZ was shifted south and west of its climatological position. Rainfall rates within the ITCZ were reduced compared to climatology, a signature consistent with typical anomalies recorded in the Southern Hemisphere summer during La Niña. By contrast, in October–December, when the SSTAs were fully consistent with strong El Niño conditions, this pattern was broadly reversed: Fig. 4.10d shows that the ITCZ, especially in the central Pacific (180°–150°W and 150°W–120°W sectors)

was positioned south of its climatological position, with strong positive anomalies (enhanced rainfall rates compared to climatology) south of ~8°N and negative anomalies (decreased rainfall rates compared to climatology) to the north. Accordingly, the SPCZ appeared to be shifted north and east of its climatological position, although the amplitude of the anomalies was smaller than those observed during the opposite situation (i.e., the La Niña-like pattern) observed at the beginning of the year.

The shift in precipitation anomaly patterns in the tropical Pacific is exemplified in Fig. 4.11, which presents the rainfall anomalies for January–March 2023 (Fig. 4.11a) and October–December 2023 (Fig. 4.11b), respectively, compared to the 1991–2020 climatological period. During the first quarter of 2023 in the tropics zone, the defining pattern was a band of strong negative rainfall anomalies (decreased rainfall compared to normal) stretching along and just north of the equator, from the Maritime Continent to the central and eastern Pacific, capped by positive anomalies to the north. This anomaly pattern corresponded to a northward-shifted ITCZ, a typical La Niña response. In the western part of the Pacific, south of the equator, the main signal was enhanced rainfall south of a line extending approximately diagonally from Papua New Guinea in the western Pacific to the islands of French Polynesia in the eastern Pacific and suppressed rainfall to the north. This can be interpreted as an SPCZ shifted southwest of its climatological position, which is another typical La Niña signal. In contrast, the pattern of rainfall anomalies in October–December was broadly reversed. Of note during the last quarter of 2023 was the large amplitude of the anomalies recorded, especially along the equator eastward from about the dateline to about 120°W, with positive anomalies exceeding 10 mm day^{-1} just north of the equator.

The exceptional nature of the rainfall anomalies observed during the last quarter of 2023, when El Niño conditions were fully established, are well illustrated in Fig. 4.12, which shows a more detailed comparison of the central Pacific (180°–150°W) rainfall transect during October–December, relative to all other years in this dataset. During this three-month period, the recorded rainfall north of ~5°N, averaged over all longitudes
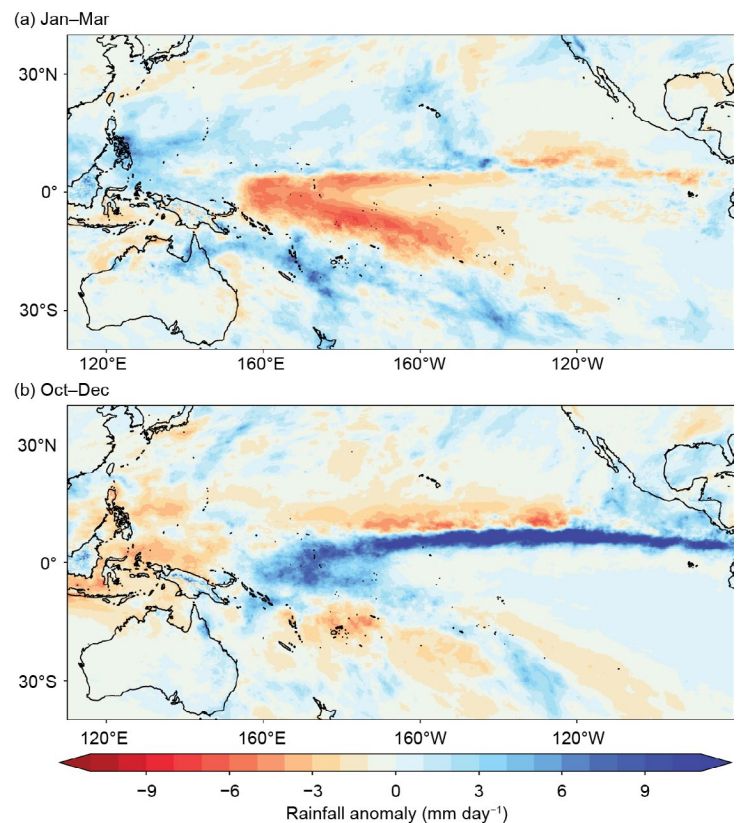
Fig. 4.11. Rainfall anomalies (mm day^{-1}) from for (a) Jan–Mar 2023 and (b) Oct–Dec 2023. The anomalies are calculated with respect to the 1991–2020 climatology. (Source: MSWEP v2.8.0.)
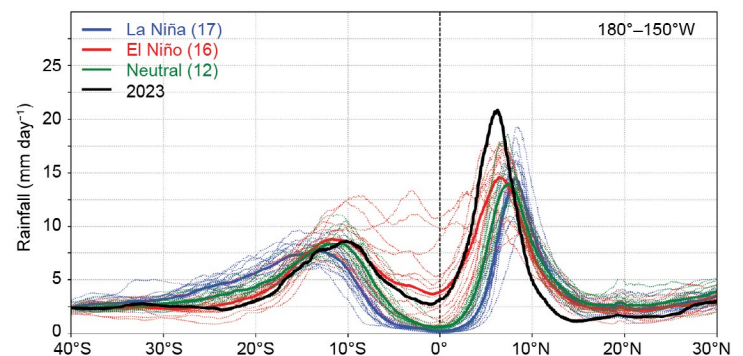
Fig. 4.12. Rainfall rate (mm day^{-1}) for Oct–Dec for each year from 1979 to 2023, averaged over the longitude sector 180°–150°W. The cross-sections are color-coded according to NOAA's Oceanic Niño Index (with a threshold of ±0.5°C), except 2023, which is shown in black. Dotted lines are individual years, and solid lines are the average overall years in each El Niño–Southern Oscillation phase. The inset legend indicates how many years went into each composite sample. (Source: MSWEP v2.8.0.)

(black line), exceeded by a large margin the rainfall rates recorded on average for all El Niño years (thick red line in Fig. 4.12).

In summary, precipitation anomaly patterns throughout 2023 underwent a dramatic shift from La Niña to El Niño-like and reached exceptional amplitude, especially just north of the equator in the eastern Pacific, corresponding to rainfall rates greatly enhanced within an ITCZ shifted south of its climatological position and, according to the MSWEP 2.8.0, the strongest anomalies on record going back to 1979.

2. ATLANTIC
A. B. Pezza and C. A. S. Coelho

The Atlantic ITCZ is a well-organized convective band that oscillates between approximately 5°N–12°N during July–November and 5°S–5°N during January–May (Waliser and Gautier 1993; Nobre and Shukla 1996). Equatorial atmospheric Kelvin waves can modulate ITCZ intraseasonal variability (Guo et al. 2014). ENSO and the Southern Annular Mode (SAM) can also influence the ITCZ on interannual time scales (Münnich and Neelin 2005). The SAM, also known as the Antarctic Oscillation, describes the north–south movement of the westerly wind belt that circles Antarctica. A positive SAM event reflects a contraction of the westerly wind belt away from the equator, with stronger subtropical ridges and less precipitation in the midlatitudes (Ding et al. 2012; Liu et al. 2021; Moreno et al. 2018).

The South Atlantic responded to the demise of the last three years of La Niña from January to May with a slightly stronger-than-normal subtropical anticyclone accompanied by anomalously warm water north of the equator and increased pressure gradients towards Antarctica, where anomalous cyclonic activity prevailed. As a result, well-below-average precipitation was widespread over much of the area in and around northern Brazil (Figs. 4.13a,b). The precipitation deficit was much stronger than observed in 2022 when La Niña was at its peak. This pattern was accompanied by a largely positive SAM, as seen by the negative pressure anomalies over the Antarctic Peninsula (Fig. 4.13a). The movement of the ITCZ was markedly north of climatology during its lifecycle (Fig. 4.14a). The Atlantic Index (see Fig. 4.14b for definition) was strongly negative, as expected for a northerly-displaced ITCZ. This pattern was associated with low-level wind convergence well north of the equator toward the areas of anomalously warm waters, with subsidence and drought conditions resulting for much of the area in and around tropical Brazil.
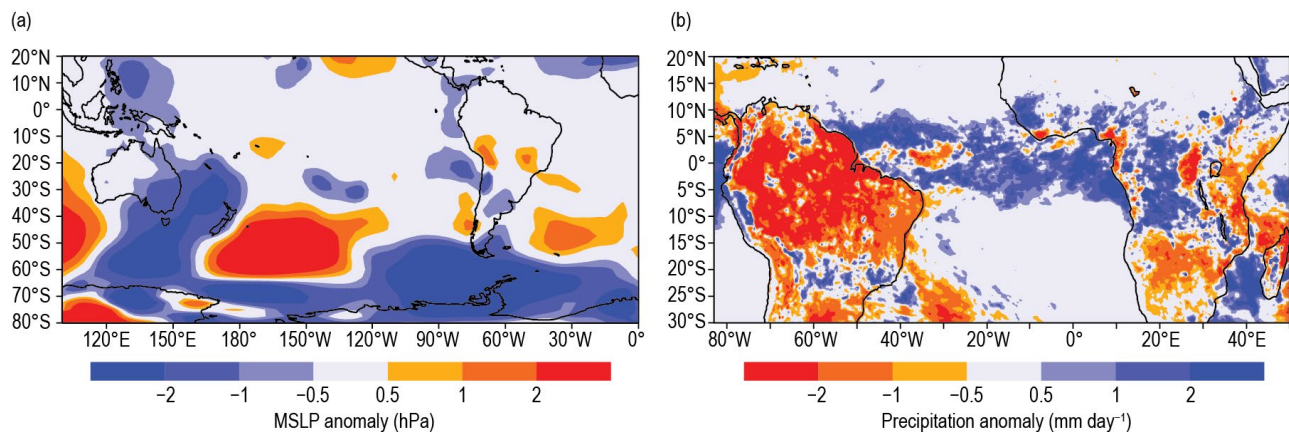
Fig. 4.13. Jan–May 2023 (a) tropical and Southern-Hemisphere mean sea-level pressure (MSLP; hPa) anomalies and (b) precipitation anomalies (mm day⁻¹) over the Atlantic sector. MSLP anomalies are calculated with respect to the 1991–2020 climatology and are derived from National Centers for Environmental Prediction (NCEP) National Center for Atmospheric Research (NCAR) reanalysis (Kalnay et al. 1996). Precipitation anomalies are calculated with respect to the 1998–2022 climatology and are derived from Climate Prediction Center Morphing technique (CMORPH; Joyce et al. 2004).
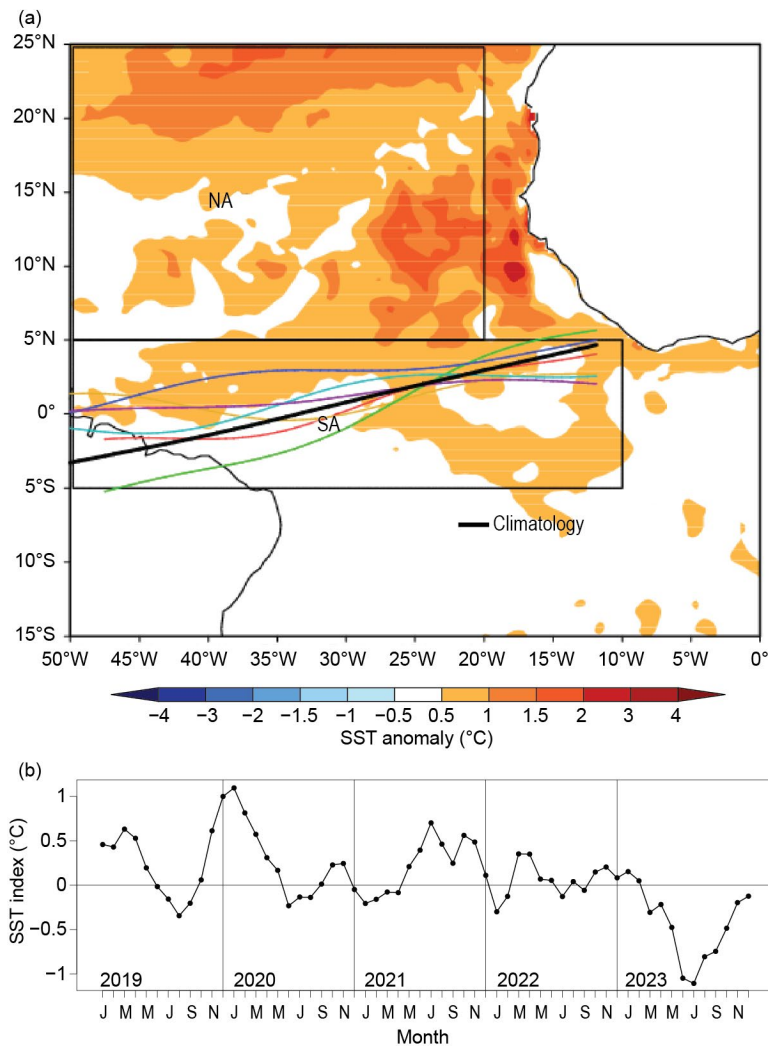
Fig. 4.14. (a) Atlantic Intertropical Convergence Zone (ITCZ) position inferred from outgoing longwave radiation (Liebmann and Smith 1996) during Mar 2023. The colored thin lines indicate the approximate position for the six pentads of the month. The thick black line indicates the Atlantic ITCZ climatological position for Mar. The sea-surface temperature (SST) anomalies (°C) for Mar 2023 calculated with respect to the 1982–2020 climatology are shaded. The two boxes indicate the areas used for the calculation of the Atlantic index in panel (b), which shows the monthly OISST (Reynolds et al. 2002) anomaly time series averaged over the South Atlantic (SA) sector (SA region: 5°S–5°N, 10°W–50°W) minus the SST anomaly time series averaged over the North Atlantic (NA) sector (NA region: 5°N–25°N, 20°W–50°W) for the period of 2019–23, forming the Atlantic index. A positive phase of the index indicates favorable conditions for enhanced Atlantic ITCZ activity south of the equator.

e. Global monsoon summary

—B. Wang and Q. He

The global monsoon is the dominant mode of annual precipitation and circulation variability and is one of the defining features of Earth's climate system (Wang and Ding 2008). Figure 4.15 depicts the monsoon domain (red lines) defined by rainfall characteristics (rainy summer versus dry winter; Wang 1994) rather than the traditional definition by winds (Ramage 1971). The Northern Hemisphere (NH) monsoon includes five regional monsoons: northern Africa, India, East Asia, the western North Pacific, and North America. The Southern Hemisphere (SH) monsoon consists of three monsoons: southern Africa, Australia, and South America. Here, we summarize both global and regional monsoon anomalies in the 2023 "monsoon year", focusing on the SH summer (November 2022–April 2023) and NH summer (May–October 2023) monsoons.

1. NH AND SH LAND MONSOON PRECIPITATION

Since monsoon rainfall over land has more important socioeconomic impacts than oceanic-monsoon rainfall, we first examine land-monsoon rainfall (LMR) in the NH (May–October) and the SH (November–April) summer monsoon. The NH and SH LMR are measured by the mean precipitation rate averaged over the land areas only in the NH and SH monsoon domains, respectively.

Historically, the year-to-year variations of the NH and SH LMR are dominated by the El Niño–Southern Oscillation (ENSO; Wang et al. 2012). Figure 4.16 highlights
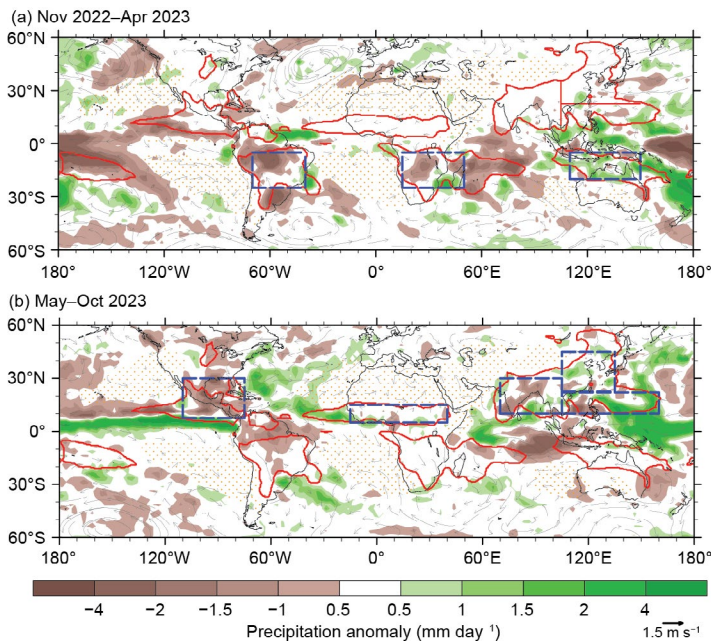
Fig. 4.15. Mean precipitation anomalies (mm day⁻¹) and 850-hPa wind anomalies (m s⁻¹) for (a) the Southern Hemisphere summer monsoon season: Nov 2022–Apr 2023 and (b) the Northern Hemisphere summer monsoon season: May–Oct 2023. The anomalies are departures from the 1991–2020 climatology. Red lines outline the global monsoon precipitation domain. Two criteria define the monsoon domain: 1) the annual precipitation range (summer-minus-winter mean) exceeds 300 mm, and 2) the summer precipitation is greater than 55% of the total annual precipitation amount, where summer here means Nov–Mar for the Southern Hemisphere and May–Oct for the Northern Hemisphere (Wang and Ding 2008). The blue rectangular boxes denote the regions where the regional monsoon precipitation indices are measured. The dotted area represents the dry region with a local summer precipitation rate below 1 mm day⁻¹. (Source: GPCP; Huffman et al. 2009.)
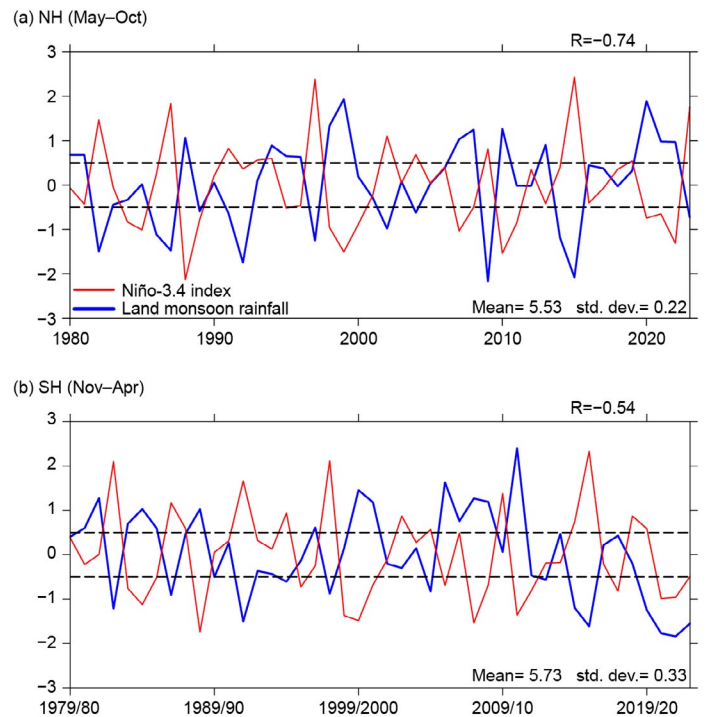
Fig. 4.16. Correlation between the El Niño–Southern Oscillation and the Northern Hemisphere (NH) and Southern Hemisphere (SH) land monsoon rainfall. (a) NH summer (May–Oct) land monsoon precipitation anomaly (blue) normalized by its standard deviation. The climatological mean NH summer land monsoon precipitation (mean) and std. dev. are shown in the lower right panel (mm day⁻¹). Numbers in the top right of each panel denote the correlation coefficient (R) between the seasonal mean precipitation anomaly and the simultaneous Niño-3.4 index (red). Dashed lines indicate ±0.5. (b) As in (a) except for the SH summer (Nov–Apr). The land monsoon precipitation excludes the monsoon rainfall over the oceanic monsoon domain. (Source: GPCP for precipitation; HadISST and ERSSTv5 for SST.)

this relationship. Both the NH and SH summer LMR are significantly anti-correlated with the corresponding Niño-3.4 index. The NH LMR has a correlation of −0.74 from 1980 to 2023 (Fig. 4.16a). The SH LMR was also negatively correlated with the Niño-3.4 index (r = −0.75) during 1979/80–2019/20. However, in the past three years the SH LMR and Niño-3.4 indices have both been negative (Fig. 4.16) such that the correlation coefficient for 1979/80–2022/23 is only −0.54 (Fig. 4.16b).

During November 2022–April 2023, the tropical Pacific experienced La Niña conditions (the third year of the 2020–22 triple La Niña). The SH LMR was well below average (−1.5 std. dev.) as noted in Fig. 4.16b. This positive relationship between ENSO and SH LMR is at odds with the historical negative correlation. As noted in the previous paragraph, this is the third consecutive year during which the SH LMR is positively related to the Niño-3.4 index. The breakdown of the negative correlation between the ENSO and SH LMR deserves further exploration.

El Niño conditions developed during May–October 2023, which were likely the predominant driver of the reduced NH LMR (−0.7 std. dev., i.e., about 0.15 mm day^{-1} or 23 mm per six months in the NH land monsoon regions; Fig. 4.16a). The decreased NH LMR in response to the 2023 El Niño is consistent with the historically observed negative El Niño–NH LMR relationship.

2. REGIONAL MONSOON PRECIPITATION AND CIRCULATION

We use regional monsoon precipitation and circulation indices to measure the integrated regional monsoon intensity. The regional summer monsoon precipitation indices signify the anomalous precipitation rate averaged over each of the blue rectangular box regions shown in Fig. 4.15. The precipitation averaged in each blue box can represent well the precipitation averaged over the corresponding, actual regional monsoon domain (Yim et al. 2014). The definitions of the circulation indices for each monsoon region are provided in Table 4.1. The circulation indices are generally defined by the meridional shear of the zonal winds at 850 hPa, which measures the intensity (shear relative vorticity) of the monsoon troughs, except for the northern African and East Asian monsoons. The northern African monsoon circulation index is defined by the westerly monsoon strength, reflecting the south–north thermal contrast between the South and North Atlantic. The East Asian summer monsoon circulation index is determined by

Table 4.1. Definition of the regional summer monsoon circulation indices and their correlation coefficients with the corresponding regional summer monsoon precipitation indices for 1979/80–2022/23. The precipitation indices are defined by the areal mean precipitation anomalies over the blue box regions shown in Fig. 4.15. R (r) represents the correlation coefficient between the total (land) monsoon precipitation and the corresponding circulation index. The correlation coefficients were computed using monthly time series (176 summer months; Jun–Sep in the Northern Hemisphere [1980–2023] and Dec–Mar in the Southern Hemisphere [1979/80–2022/23]). Bolded numbers represent significance at the 99% confidence level.

Regional monsoon	Definition of the circulation index	R (r)
Indian (ISM)	U850 (5°N–15°N, 40°E–80°E) minus U850 (25°N–30°N, 60°E–90°E)	**0.71 (0.58)**
Western North Pacific (WNPSM)	U850 (5°N–15°N, 100°E–130°E) minus U850 (20°N–35°N, 110°E–140°E)	**0.87 (0.71)**
East Asian (EASM)	V850 (20°N–35°N, 120°E–140°E) plus V850 (10°N–25°N, 105°E–115°E)	**0.72 (0.72)**
North American (NASM)	U850 (5°N–15°N, 130°W–100°W) minus U850 (20°N–30°N, 110°W–80°W)	**0.86 (0.79)**
Northern African (NAFSM)	U850 (0°–10°N, 40°W–10°E)	**0.71 (0.71)**
South American (SASM)	U850 (20°S–5°S, 70°W–40°W) minus U850 (35°S–20°S, 70°W–40°W)	**0.80 (0.80)**
Southern African (SAFSM)	U850 (12°S–2°S, 10°W–30°E) minus U850 (30°S–10°S, 40°E–60°E)	**0.58 (0.45)**
Australian (AUSSM)	U850 (15°S–0°, 90°E–130°E) minus U850 (30°S–20°S, 100°E–140°E)	**0.88 (0.79)**

the meridional wind strength, reflecting the east–west thermal contrast between the Asian continent and the western North Pacific. The precipitation and circulation indices are well correlated for most regional monsoons, with monthly mean correlation coefficients ranging from 0.71 to 0.88, except for the southern African monsoon (Table 4.1). Thus, the regional precipitation and circulation indices generally provide consistent measurements of the strength of each regional monsoon system. Notably, in the Indian and southern African monsoon regions, the circulation indices represent land monsoon rainfall less faithfully due to the fact that the leading modes of the precipitation anomalies in these two regions show a dipolar pattern (Yim et al. 2014).

During SH summer from November 2022 to April 2023, the La Niña-enhanced Walker Circulation contributed to suppressed rainfall over the central-eastern Pacific and increased rainfall over the Maritime Continent and northern Australia (Fig. 4.15a). However, precipitation was significantly reduced over the South American and southern African monsoon regions, which is abnormal for La Niña. Figure 4.17 shows areal-averaged monsoon precipitation and circulation intensities for each regional monsoon. Both the Australian summer monsoon precip-
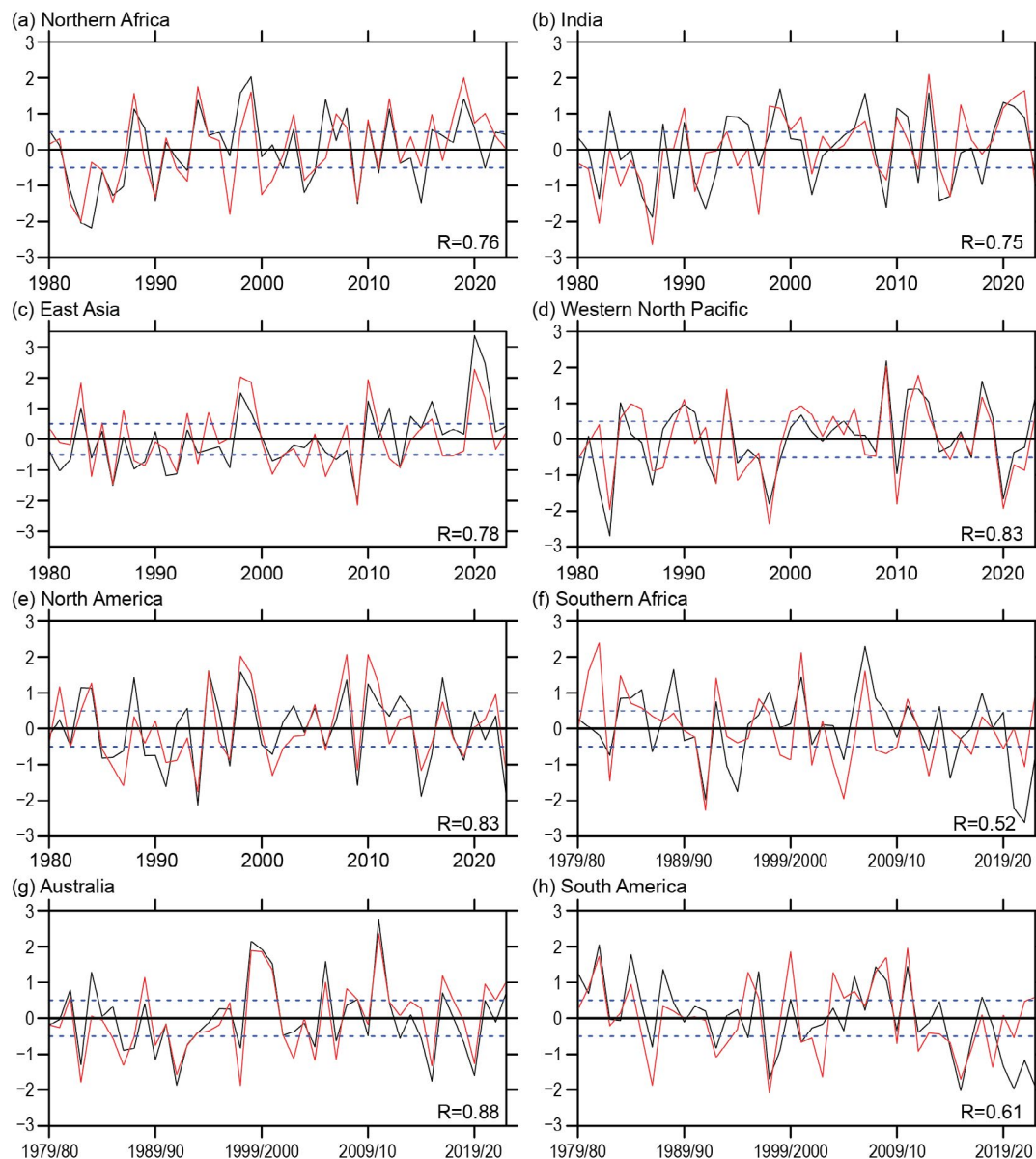
Fig. 4.17. (a)–(h). Temporal variations of summer monsoon precipitation (black lines) and low-level circulation (red lines) indices for eight regional monsoons. The precipitation indices represent the anomalous precipitation rate averaged over the blue rectangular box regions shown in Fig. 4.15. The corresponding circulation indices are defined in Table 4.1. All indices were normalized by their corresponding standard deviations (ordinate) derived for the period 1979/80–2022/23. Numbers in the bottom right of each panel denote the correlation coefficient (R) between the seasonal mean precipitation and circulation indices (sample size: 44). Dashed lines indicate ±0.5 std. dev. The summer monsoon seasons are May–Oct for the Northern Hemisphere and Nov–Apr for the Southern Hemisphere. (Data source: GPCP for precipitation; ERA5 [Hersbach et al. 2020] for circulation).

itation and circulation index showed above-normal intensity (Fig. 4.17g). The South American monsoon precipitation was 2 std. dev. below average, but the related circulation strength was 0.5 std. dev. above average (Fig. 4.17h). The southern African summer monsoon precipitation was 1 std. dev. below average, while the circulation intensity was 0.7 std. dev. above average (Fig. 4.17f). Over the South American and southern African regions, the precipitation and circulation anomalies showed opposite tendencies, which is abnormal. Overall, the circulation indices of the three SH regional monsoon systems indicate enhanced monsoons, consistent with the historically observed negative correlations between the SH regional monsoons and ENSO. However, inconsistencies in the precipitation with the expected La Niña response remain to be explored.

During the 2023 NH summer monsoon season, an El Niño developed, which severely suppressed the North American monsoon by drawing convection southward (Fig. 4.15b). The Pacific warming pattern increased precipitation in the far western Pacific (north of New Guinea) and the Philippine Sea and reduced precipitation over the western Maritime Continent and the southeast tropical Indian Ocean (Fig. 4.15b). Compared to the canonical response for eastern Pacific El Niño development, the dry anomalies over the Maritime Continent were shifted westward, possibly due to the relatively warm central Pacific. The suppressed rainfall anomaly over the western Maritime Continent and the eastern Indian Ocean could excite atmospheric descending Rossby waves residing on both sides of the equator. This pattern then reduces Indian summer monsoon rainfall and triggers the development of a positive phase of the Indian Ocean (IO) dipole sea-surface temperature anomalies (e.g., anomalous east IO cooling and west IO warming). Regionally, the Indian and North American monsoon precipitation and circulation indices all showed significant negative anomalies (Figs. 4.17b,e), which contributed to the decreased NH LMR (Fig. 4.16a). Over the northern African and East Asian summer monsoon regions, both the precipitation and circulation patterns were near normal (Figs. 4.17a,c). The western North Pacific monsoon circulation and rainfall were both positive. In summary, regardless of the westward shift of the convective anomalies over the Maritime Continent during the development of the 2023 El Niño, the NH regional monsoon responses basically followed the typical El Niño–monsoon relationships.

f. Indian Ocean dipole
—L. Chen and J.-J. Luo

The Indian Ocean dipole (IOD) is the dominant interannual mode in the tropical Indian Ocean (IO), characterized by a zonal dipole of sea-surface temperature (SST) anomalies in the equatorial IO (Saji et al. 1999; Luo et al. 2010, 2012). The dipole originates from local air–sea interaction processes in the tropical IO and/or ENSO forcing (Luo et al. 2007, 2010). The IOD typically develops in boreal spring and summer, matures in autumn, and rapidly terminates in early winter. A positive IOD (pIOD) event usually features negative SST anomalies in the eastern IO and positive SST anomalies in the west during boreal summer and autumn, and vice versa for a negative IOD (nIOD). The IOD phenomenon has a strong nonlinear feature, that is, the pIOD is usually stronger than the nIOD due to the asymmetric strength of the air–sea feedback between the two phases of the IOD (Luo et al. 2007; Hong et al. 2008).

In 2023, the tropical IO witnessed a strong pIOD event with significant negative SST anomalies in the eastern IO and positive SST anomalies in the western IO (Fig. 4.18a). The IOD index reached ~1.2°C in boreal autumn 2023 based on the OISST dataset (Fig. 4.18b). There have been 12 pIOD events from 1982 to the present (1982, 1991, 1994, 1997, 2006, 2007, 2011, 2012, 2015, 2018, 2019, 2023), and they tend to be associated with El Niño events as in 2023. The pIOD event in 2023 was the fourth-strongest pIOD event in the past 42 years (the three stronger events occurred in 2019, 1997, and 1994).

Following a negative IOD event in 2022, the tropical IO was characterized by a weak Indian Ocean basin (IOB) mode from late boreal winter to early spring 2023 (Figs. 4.18a–c). The IOB mode is believed to favor the decay of El Niño via modulating the zonal wind anomalies in the western equatorial Pacific as noted by Wu et al. (2024). Easterly wind anomalies then developed over the central IO during boreal spring and summer 2023 (Figs. 4.18b, 4.19). As a result, a pIOD event began to develop in boreal spring and summer 2023 and strengthened in boreal autumn 2023 (Fig. 4.18b). From the perspective of the tropical Indo-Pacific Ocean, these easterly wind anomalies over the central IO region are closely associated with the rapidly developing El Niño conditions in the tropical Pacific (Fig. 4.18c). In response to El Niño, an anomalous Walker Circulation occurs over the equatorial sector of the Indo-Pacific Ocean. As indicated by the anomalous precipitation and surface winds (Fig. 4.19) and the anomalous 200-hPa velocity potential field (contours in Fig. 4.20), anomalous ascending motion and increased rainfall occur over the central equatorial Pacific, while anomalous descending motion and below-normal rainfall occurred over the western equatorial Pacific, the Maritime Continent, and the eastern equatorial IO region. Consequently, anomalous easterly winds over the equatorial IO began to develop in the boreal spring of 2023.
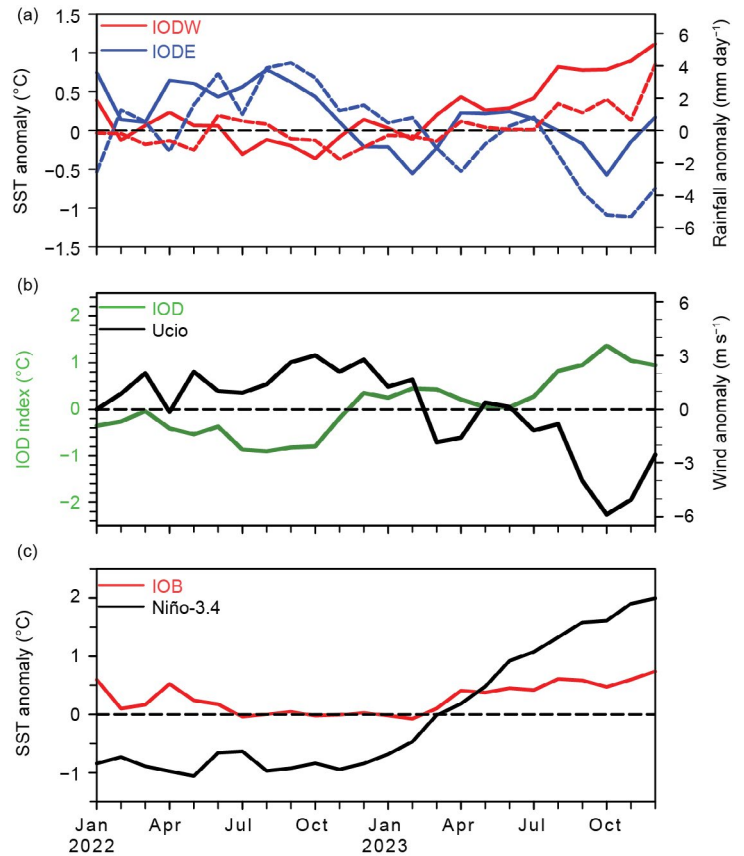
Fig. 4.18. (a) Monthly anomalies of sea-surface temperature (SST; °C; solid lines) and precipitation (mm day⁻¹; dashed lines) of the Indian Ocean dipole (IOD) in the eastern pole (IODE; 10°S–0°, 90°E–110°E; blue lines) and the western pole (IODW; 10°S–10°N, 50E°–70°E; red lines) of the IOD. (b) As in (a), but for the IOD index (measured by the SST difference between IODW and IODE, green line) and surface zonal wind anomaly (m s⁻¹) in the central equatorial IO (Ucio; 5°S–5°N, 70°E–90°E; black line). (c) As in (a), but for the SST anomalies in the Niño-3.4 region (5°S–5°N, 170°W–120°W; black line) and the tropical IO (IOB; 20°S–10°N, 40°E–120°E; red line). Anomalies are relative to the 1982–2023 base period. (Sources: NOAA OISST [Reynolds et al. 2002]; monthly CMAP precipitation analysis] available at http://ftpprd.ncep.noaa.gov/pub/precip/cmap/]; and JRA-55 atmospheric reanalysis [Ebita et al. 2011].)

Due to the positive feedback between the easterly wind anomalies and the dipole of SST anomalies over the equatorial sector of the IO, the pIOD event rapidly grew from late spring to boreal summer 2023, as shown in Figs. 4.18b, 4.19b,c, 4.20b,c. As a result of the positive air–sea feedback processes among the anomalous SST, low-level winds, and precipitation fields, an obvious dipole structure of SST and precipitation anomalies occurred in the tropical IO during boreal autumn 2023, with anomalous cool and dry conditions in the eastern IO and warm and wet conditions in the western IO (Figs. 4.19, 4.20).

In summary, a strong pIOD event occurred in 2023, with the IOD index reaching 1.2°C during boreal autumn. The development of this pIOD event appears to have been driven by El Niño conditions, following two consecutive negative IOD events in 2021 and 2022 that coincided with La Niña conditions in the Pacific (Chen and Luo 2022). In response to the development of El Niño in 2023, an anomalous Walker circulation occurred over the tropical Indo-Pacific sector, with a stronger descending branch over the western equatorial Pacific, the Maritime Continent, and the eastern equatorial IO. Consequently, anomalous easterly winds developed in boreal summer 2023, causing a dipole of SST anomalies to develop. There was a clear zonal dipole of SST and precipitation anomalies in the equatorial IO during boreal autumn 2023. In early winter (November–December) 2023, the pIOD started to decay due to IOD dynamics.
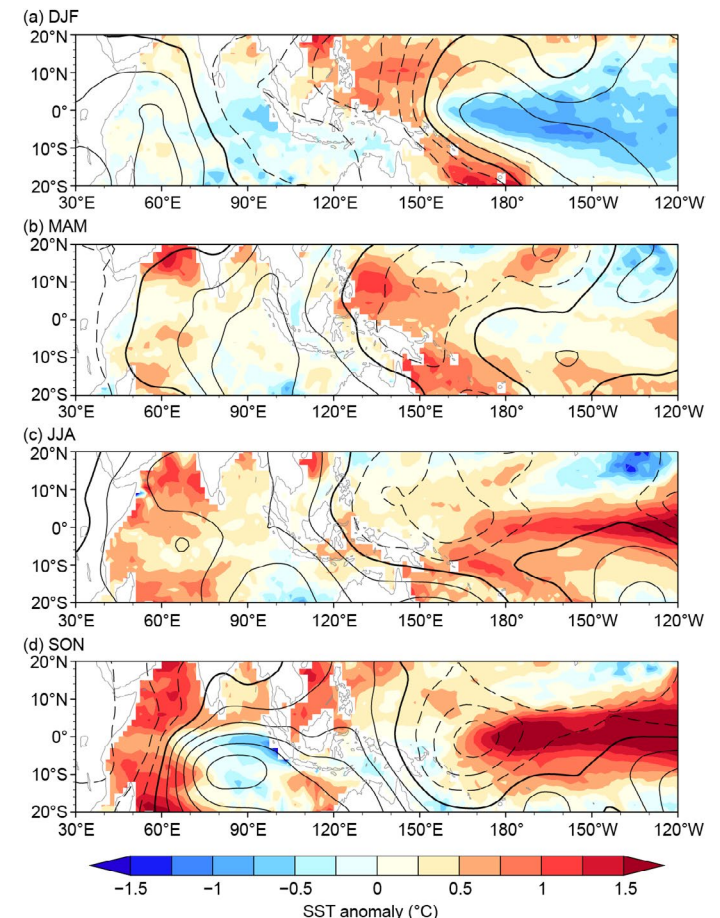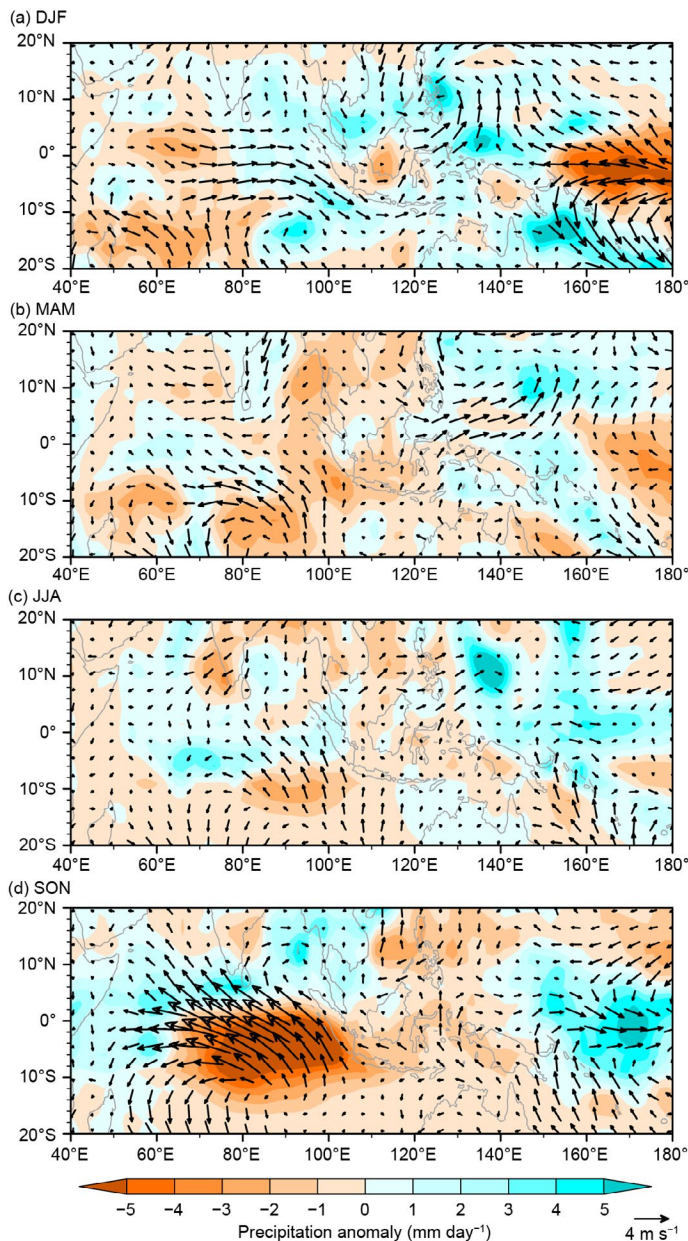
Fig. 4.19. Precipitation (mm day⁻¹) and surface wind (m s⁻¹) anomalies during (a) Dec 2022–Feb 2023, (b) Mar–May 2023, (c) Jun–Aug 2023, and (d) Sep–Nov 2023. (Sources: monthly CMAP precipitation analysis [available at ftp://ftp.cpc.ncep.noaa.gov/precip/cmap] and JRA-55 atmospheric reanalysis [Ebita et al. 2011].)

Fig. 4.20. Sea-surface temperature anomalies (°C, colored scale) superimposed by 200-hPa velocity potential (× 10⁶ m² s⁻¹, contours with an interval of 1, and solid/ dashed/bold curves denote positive/negative/zero values) during (a) Dec 2022–Feb 2023, (b) Mar–May 2023, (c) Jun–Aug 2023 and (d) Sep–Nov 2023. Anomalies were calculated relative to the climatology over the period 1982–2023. (Sources: NOAA OISST [Reynolds et al. 2002] and JRA-55 atmospheric reanalysis [Ebita et al. 2011].)

g. Tropical cyclones

1. OVERVIEW

H. J. Diamond and C. J. Schreck

The International Best Track Archive for Climate Stewardship (IBTrACS) dataset comprises historical tropical cyclone (TC) best-track data from numerous sources around the globe, including all of the World Meteorological Organization (WMO) Regional Specialized Meteorological Centers (RSMCs; Knapp et al. 2010). This dataset represents the most complete compilation of global TC data. From these data, 1991–2020 climatological values of TC activity for each basin using statistics from both the WMO RSMCs and the Joint Typhoon Warning Center (JTWC) are calculated following Schreck et al. (2014). These values are referenced in each subsection. Tallying the global TC numbers is challenging and involves more than simply adding up basin totals, as some storms cross TC basin boundaries, some TC basins overlap, and multiple agencies track and categorize them. The Northern Hemisphere (NH) basins are typically measured from January to December while Southern Hemisphere (SH) basins are typically measured from July to June. Global values here are the sum of NH for 2023 and SH for 2022/23. Unless otherwise noted, the statistics are based on preliminary data from NOAA's National Hurricane Center (NHC) and the JTWC. However, differences between the JTWC and the WMO RSMCs or other local agencies will be noted as appropriate.

Based on preliminary data from the NHC and the JTWC as archived in IBTrACS (Fig. 4.21), the combined 2023 season had 82 named storms (sustained wind speeds ≥34 kt or 17 m s^{-1}), which is 15 fewer than the previous season (2022; Diamond and Schreck 2022) and also below the 1991–2020 average

Fig. 4.21. (a) Global summary of tropical cyclone (TC) tracks overlaid on associated OISST anomalies (°C; Reynolds et al. 2002) for the 2023 season relative to 1991–2020; (b) global TC counts; and (c) global accumulated cyclone energy (ACE) values (× 10^4 kt^2). Horizontal lines in (b) and (c) are the 1991–2020 normal values.

of 87. There were 45 hurricanes/typhoons/cyclones (HTCs; sustained wind speeds ≥64 kt or 33 m s^{-1}), 30 of which reached major HTC status (sustained wind speeds ≥96 kt or 49 m s^{-1}), which was nearly double the amount from 2022. The accumulated cyclone energy (ACE) for the season was 866 × 10^4 kt^2, which was 67.5% greater than that of last year (Diamond and Schreck 2022).

In sections 4g2–4g8, 2022/23 SH and 2023 NH seasonal TC activity are described and compared to the historical record for each of the seven WMO-defined TC basins. For simplicity, all counts are broken down by the U.S. Saffir-Simpson Hurricane Wind Scale (SSHWS)[2]. The overall picture of global TCs during 2023 is shown in Fig. 4.21, and counts by category and intensity are documented in Table 4.2.

---

[2]   SSHWS is based on 1-minute averaged winds, and the categories are defined at: https://www.weather.gov/mfl/saffirsimpson; the Australian category scale is based on 10-minute averaged winds, and those categories are defined at https://australiasevereweather.com/cyclones/tropical_cyclone_intensity_scale.htm.

The eastern North Pacific, North Indian Ocean, and South Indian Ocean basins each had above-normal ACE relative to 1991–2020. Table 4.2 uses this climatological period for classifying seasons for consistency amongst basins. However, NOAA uses the terciles from 1951–2020 to classify North Atlantic ACE owing to the longer record of data there. The North Atlantic ACE was above normal relative to 1951–2020 but near normal relative to 1991–2020. By NOAA's definition, 2023 was the seventh above-normal season in the last eight years. Activity in the North Indian Ocean was particularly pronounced. Depending on the metric, it was either the second- or third-most-active season since 1981.

While the western North Pacific was near normal in terms of ACE, it was the fourth consecutive year with below-normal numbers of typhoons. The count of 17 named storms in the western North Pacific was the second lowest since 1951. The South Indian Ocean was the only SH basin with above-normal ACE, which was largely due to the exceptionally long-lived Cyclone Freddy (Sidebar 4.2).

Freddy was one of seven storms globally that achieved Category 5 on the Saffir-Simpson Hurricane Wind Scale (1-minute maximum sustained winds ≥137 kt) during 2023. Sidebar 4.1 discusses another of these Category 5 storms, Hurricane Otis, which was the strongest landfalling hurricane on record for the west coast of Mexico.

Table 4.2. Global counts of tropical cyclone (TC), hurricane/typhoon/cyclone (HTC), major HTC, Saffir-Simpson Category 5 (SS Cat 5) storm activity by basin, and accumulated cyclone energy (ACE) for 2023. "+" denotes top tercile; "++" is top 10%; "−" is bottom tercile; "−−" is bottom 10% (all relative to 1991–2020). Note that some inconsistencies between Table 4.2 and the text of the various basin write-ups in section 4g exist and are unavoidable, as tallying global TC numbers is challenging and involves more than simply adding up basin totals. This is because some storms cross TC basin boundaries, some TC basins overlap, and multiple agencies are involved in tracking and categorizing TCs.

Basin	TCs	HTCs	Major HTCs	SS Cat 5	ACE
North Atlantic	20 ++	7	3	1 +	144
Eastern Pacific	17	10 +	8 +	2 +	166 +
Western Pacific	17 − −	12 −	8	2	268
North Indian	8 ++	4 ++	3 ++	1 ++	56 ++
South Indian	9 −	7 +	4 +	1 ++	134 +
Australia	9 −	5	4 +	0	67
Southwest Pacific	6	3	2	0	31
Global	82 −	45	30 +	7 +	866 +

2. ATLANTIC BASIN

M. Rosencrans, E. S. Blake, C. W. Landsea, H. Wang, S. B. Goldenberg, R. J. Pasch, D. S. Harnos, and H. Lopez

(i) 2023 Seasonal activity

The 2023 Atlantic hurricane season produced 20 named storms (plus one tropical depression), of which 7 became hurricanes and 3 of those became major hurricanes (Fig. 4.22a). The HURDAT2 1991–2020 seasonal averages (included in IBTrACS) are 14.4 named storms, 7.2 hurricanes, and 3.2 major hurricanes (Landsea and Franklin 2013). The 20 named storms during 2023 equaled 1933 for the fourth-highest total in the HURDAT2 database, with the top three seasons for most named storms being 2020 (30), 2005 (27), and 2021 (21). In contrast, the number of hurricanes and major hurricanes were at the long-term average. The 2023 hurricane season was classified by NOAA as an above-normal season, as ACE exceeded the threshold necessary

for an above-normal season (discussed in detail later in this section). This was the seventh above-normal season since 2016, with only 2022 being classified as a near-normal season and no years in that period classified as below normal.

Seven of the 20 named storms during 2023 were short-lived (≤2 days), including the subtropical storm that developed in January. There has been a large artificial increase (approximately five per year) in these "shorties" since 2000 (Landsea et al. 2010). These increased counts primarily reflect new observational capabilities such as scatterometers, Advanced Microwave Sounding Units, and the Advanced Dvorak Technique, and have no association with any known climate variability (Villarini et al. 2011).

The 2023 seasonal accumulated cyclone energy ACE value was 144% of the 1951–2020 median of 96.7×10^4 kt^2 as noted in Fig. 4.22b. This value is above NOAA's threshold for an above-normal season (126.1×10^4 kt^2, or 130% of the 1951–2020 median). Since the current Atlantic high-activity era began in 1995 (Goldenberg et al. 2001; Bell et al. 2019, 2020), there have been 20 above-normal seasons, with 10 classified as extremely (aka hyper-) active (ACE >165% of median). By comparison, the preceding 24-year low-activity era of 1971–94 had only two above-normal seasons, with none classified as extremely active.

(ii) Storm formation times, regions, and landfalls

Tropical cyclone activity was abundant during August–October (Fig. 4.23a), the core months of the season, with one early formation in January and no activity in November. Activity for the calendar year started on 16 January with the development of an unnamed subtropical storm. During the Atlantic hurricane season, at least one named storm developed in every month except November, including three named storm formations during June. Named storm formations during August and September were about twice the average for each of those months. October had near-average activity with two named storms. This was the first year on record that the tropical Atlantic (east of 60°W, south of 23.5°N) had two named storm formations—Bret and Cindy—in June. Notably, 13 named storms formed between 20 August and 28 September, the most on record and breaking the old record of 12 set in 2020.

Of the 20 named storms that occurred during 2023, 60% (12 of 20) formed in the Main Development Region (MDR; Fig. 4.23b). The MDR spans the tropical Atlantic Ocean and Caribbean Sea between 9.5°N and 21.5°N (Goldenberg and Shapiro 1996; Goldenberg et al. 2001). Since 1950, approximately 42% of named storms form in the MDR in any given year, with about 18% in the Gulf of Mexico. In 2023, only two tropical storms and no hurricanes formed in the Gulf of Mexico (Fig. 4.23c), which is a smaller-than-average fraction of the overall tropical activity,
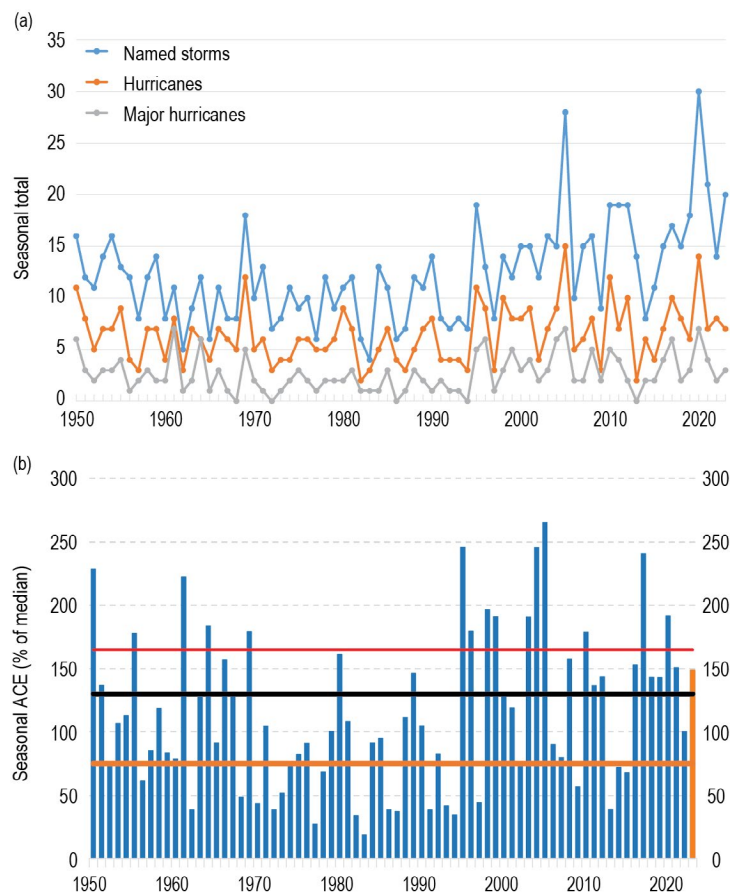
Fig. 4.22. Seasonal Atlantic hurricane activity during the period 1950–2023. (a) Numbers of named storms (blue), hurricanes (orange), and major hurricanes (gray). (b) The accumulated cyclone energy (ACE) index expressed as percent of the 1950–2020 median value. ACE is calculated by summing the squares of the six-hourly maximum sustained surface wind speed (kt) for all periods while the storm is at least of tropical storm strength. The black (orange) line represents NOAA's threshold for an above-normal (below-normal) season (https://www.cpc.ncep.noaa.gov/products/outlooks/Background.html). Note that there is a low bias in activity during the 1950s to the early 1970s due to the lack of satellite imagery and a technique (Dvorak) to interpret tropical cyclone intensity for systems over the open ocean. (c) 2023 Atlantic basin storm tracks. (Source: HURDAT2 [Landsea and Franklin 2013].)

contributing just 0.6% of the total annual ACE. The associated MDR-related ACE value was 180% of the median annual MDR ACE. The storm tracks during 2023 highlight the lack of activity in the Gulf of Mexico and the relatively higher activity originating in the MDR (Fig. 4.23c).

Even though the season had above-normal activity overall, there were only two landfalling hurricanes and several non-hurricane-strength landfalls. Despite the low overall activity in the Gulf of Mexico, it did include the season's only major hurricane landfall—Category 3 Hurricane Idalia, which came ashore in the Big Bend area of Florida. Other notable landfalling systems include Hurricane Lee, which made landfall as a post-tropical cyclone in Nova Scotia with winds of ~60 kt (30 m s⁻¹), and Hurricane Tammy, which made landfall on Barbuda with winds of 75 kt (39 m s⁻¹).
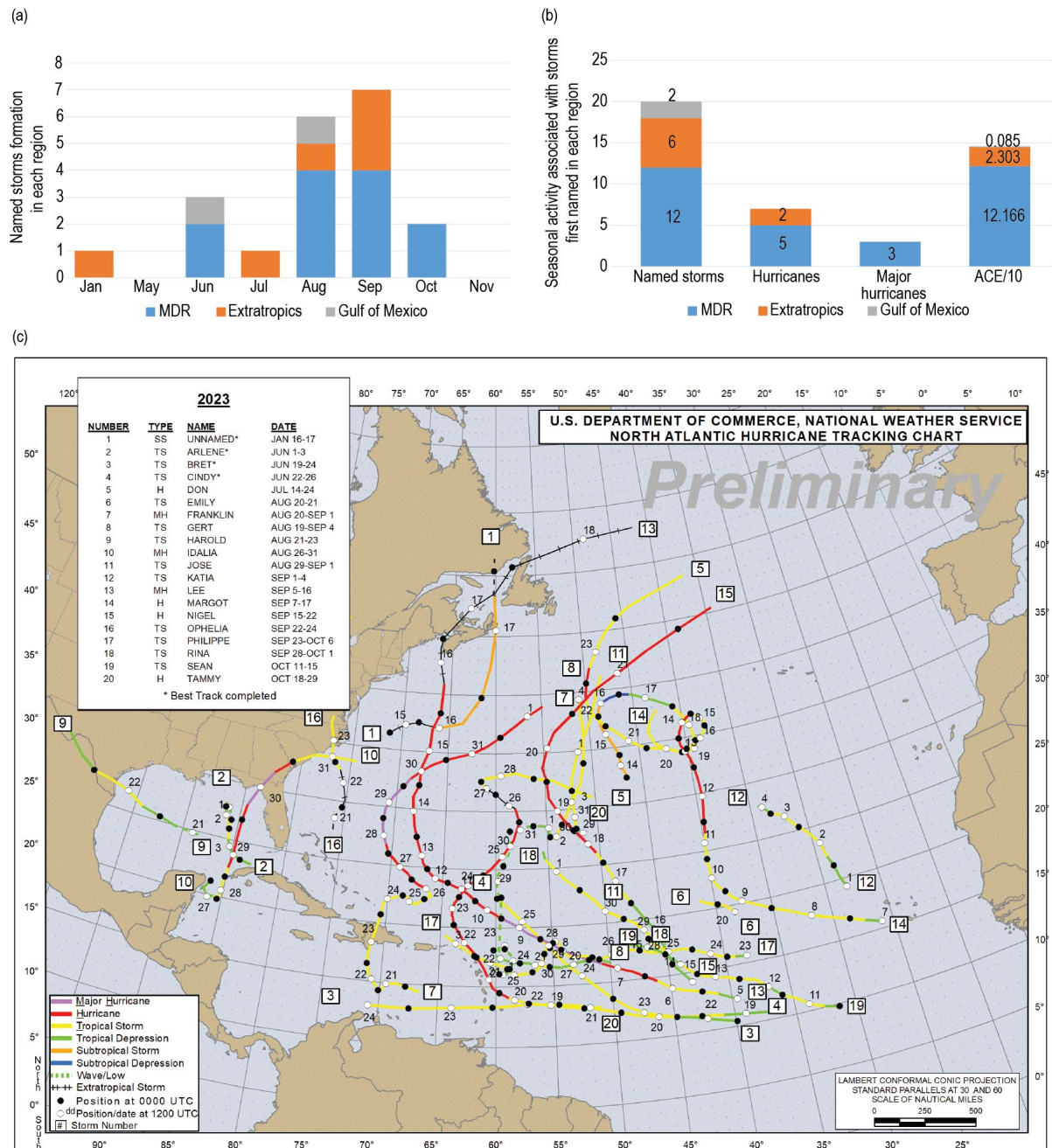
Fig. 4.23. Atlantic tropical cyclone (TC) activity in 2023. (a) Named storm counts for the month and region where the storm was first named and (b) total seasonal counts for the three storm classifications and accumulated cyclone energy (ACE) for each region where the storm was first named. ACE reflects the entire storm ACE and is attributed to the region in which the storm was first named. Regions in (a) and (b) are indicated by the color bar below panel (b). In (c), the tracks of named storms are plotted and show the relative dearth of storms in the Gulf of Mexico. The "extratropics" includes all regions except for the Main Development Region and the Gulf of Mexico. (Source: HURDAT2; Landsea and Franklin 2013].)

(iii) Sea-surface temperatures

Sea-surface temperatures (SSTs) were exceptionally warm throughout the MDR (Fig. 4.24a), with an August–October (ASO)-area-averaged SST anomaly of +1.16°C (Fig. 4.24b), setting a record since at least 1950 by more than 0.5°C. Within the MDR, SST anomalies ranged from just above +0.5°C to greater than +1.5°C. The area-averaged SST anomaly in the MDR was 0.55°C higher than that of the remainder of the global tropics (Fig. 4.24c), with the global tropics reflecting an El Niño state for the entire ASO period. This signal typifies the warm phase of the Atlantic Multidecadal Oscillation (Enfield and Mestas-Nuñez 1999; Bell and Chelliah 2006) and is a ubiquitous characteristic of Atlantic high-activity eras such as 1950–69 and 1995–present (Goldenberg et al. 2001; Vecchi and Soden 2007; Bell et al. 2018).
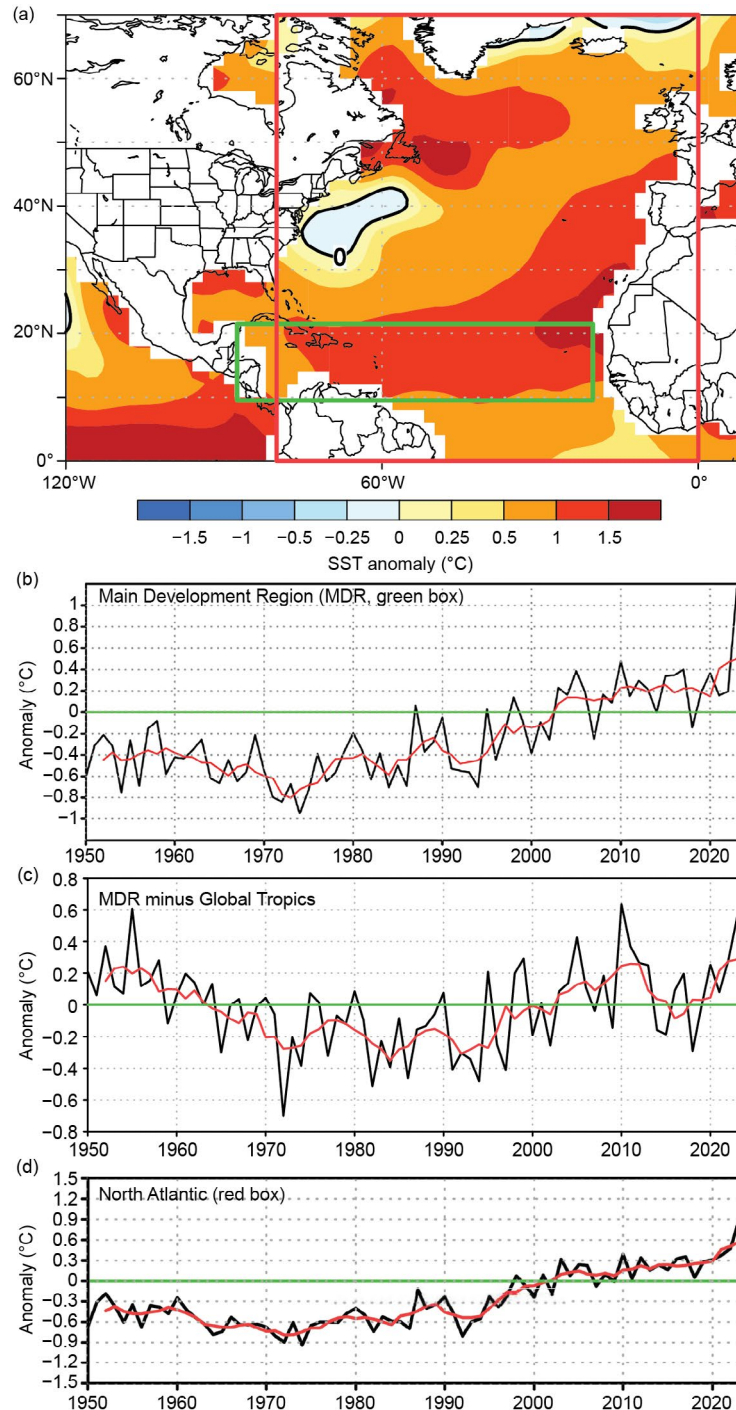
Fig. 4.24. (a) Aug–Oct 2023 sea-surface temperature (SST) anomalies (°C). (b)–(d) Time series of Aug–Oct area-averaged SST anomalies (black) and five-point running mean of the time series (red): (b) in the Main Development Region (MDR, green box in [a] spanning 20°W–87.5°W and 9.5°N–21.5°N), (c) difference between the MDR and the global tropics (20°S–20°N), and (d) in the North Atlantic (red box in [a] spanning 0°–80°W and 0°–70°N). Anomalies are departures from the 1991–2020 period means. (Source: ERSST-v5 [Huang et al. 2017].)

During ASO 2023, above-average temperatures were also reflected across most of the North Atlantic Ocean. Outside of the MDR, the largest anomalies (exceeding +1.5°C) occupied portions of the central North Atlantic (Fig. 4.24a). The area-averaged SST anomaly in the western North Atlantic (red box, Fig. 4.24a) was +0.90°C, reflecting a continuation of exceptional warmth that began in 2012 (Fig. 4.24d). Another major SST forcing during the North Atlantic hurricane season was the ongoing El Niño (see section 4b).

(iv) Atmospheric conditions

Climatologically, the ASO peak in Atlantic hurricane activity largely reflects the June–September peak in the West African monsoon. The inter-related circulation features of an enhanced monsoon act to further increase hurricane activity, while those of an anomalously weak monsoon act to suppress it (Gray 1990; Hastenrath 1990; Landsea et al. 1992; Bell and Chelliah 2006; Bell et al. 2018, 2020). The association on multi-decadal time scales between the AMO and Atlantic hurricane activity in part exists because of their common relationship to the West African monsoon (Bell and Chelliah 2006).

The West African monsoon was near-average, as indicated by a mix of negative outgoing longwave radiation (OLR) anomalies and near-average values across the African Sahel (red box, Fig. 4.25a). Total OLR values in this region averaged 241 W m^{-2} (Fig. 4.25b), while values farther south (blue box, Fig. 4.25a) averaged 228 W m^{-2}, with values less than 240 W m^{-2} indicating deep tropical convection. The OLR time series shows that an enhanced monsoon has largely prevailed throughout the current Atlantic high-activity era and warm AMO of 1995–present (Fig. 4.25b). By contrast, a much weaker monsoon with OLR values well above 240 W m^{-2} in the Sahel region was typical of the low-activity era and cool AMO period of the 1980s and early 1990s. June precipitation across the Sahel region was well above normal, July and August precipitation were below normal, and September precipitation was near normal (NOAA 2023), further indicating a varied signal from the West African monsoon.

Consistent with a near-normal monsoon, the large-scale divergent circulation at 200 hPa featured a weak signal over western Africa (Fig. 4.25c). The strongest negative velocity potential anomalies were over the Atlantic, with strong positive anomalies over the Gulf of Mexico and Central America, consistent with reduced activity in the western portion of the Atlantic basin. Analysis of the streamfunction at 200 hPa (Fig. 4.26a) shows anomalous anticyclones over the Caribbean
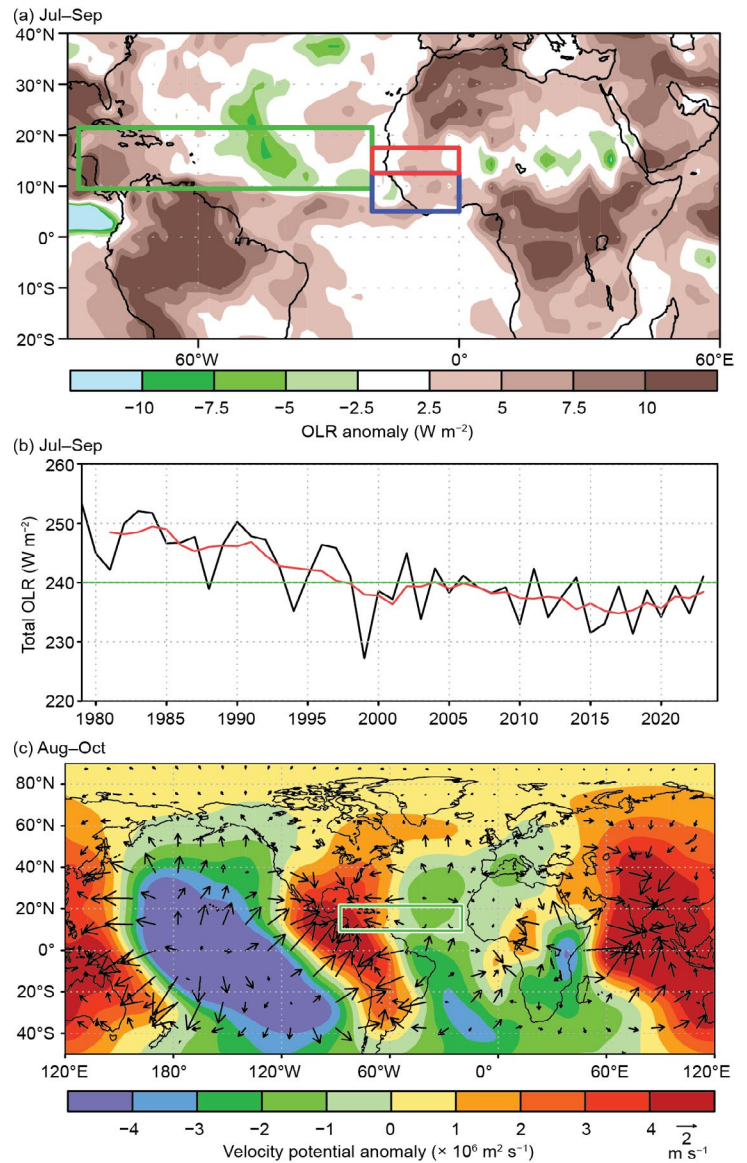
Fig. 4.25. (a) Jul–Sep 2023 anomalous outgoing longwave radiation (OLR; W m^{-2}), with negative (positive) values indicating enhanced (suppressed) convection. (b) Time series of Jul–Sep total OLR (black), five-point running mean of the time series (red) averaged over the African Sahel region (red box in (a) spanning 20°W–0° and 12.5°N–17.5°N). (c) Aug–Oct 2023 anomalous 200-hPa velocity potential (× 10^6 m^2 s^{-1}) and divergent wind vectors (m s^{-1}). In (a), the green box denotes the Atlantic Main Development Region. In (b), the green line represents the threshold for deep convection (240 W m^{-2}). Anomalies are departures from the 1991–2020 means. (Source: [Kalnay et al. 1996] for velocity potential and wind; [Liebmann and Smith 1996] for OLR.)

and much of the MDR, though anomalous cyclonic flow is evident over the eastern Atlantic and western Africa. In 2023, there were no indications of significant midlatitude wave-train breaking into the tropical Atlantic. In contrast, significant wave breaking into the Atlantic was evident during 2022, as was a lack of moisture in the upper levels during August. During 2023, mid-level and upper-level moisture were abundant across the tropical Atlantic during ASO (Fig. 4.26b). The 1000-hPa anomalous height and wind field (Fig. 4.26c) shows that heights were below normal across the MDR, a signal typically associated with busy Atlantic hurricane seasons (Knaff 1997). Indications are that the West African monsoon was a minor contributor to the heightened named-storm total.

August–October 2023 200-hPa-to-850-hPa vertical wind shear was below average for much of the MDR and slightly higher than average for the Gulf of Mexico (Fig. 4.27a). The area-averaged magnitude of the vertical wind shear for the entire MDR was 6.5 m s⁻¹ (Fig. 4.27b) and for the Gulf of Mexico was 10.3 m s⁻¹ (Fig. 4.27c). The 200-hPa-to-850-hPa vertical wind shear over the MDR was in the lowest decile since 1950, while over the Gulf of Mexico, the value was above the upper threshold of 10 m s⁻¹ considered conducive to hurricane formation on monthly time scales (Bell et al. 2017). Note that the MDR shows a strong multidecadal variability of vertical wind shear, which is correlated with multidecadal fluctuations in TC activity, whereas there is no such variability in the Gulf of Mexico (Figs. 4.27b,c; Goldenberg et al. 2001). The low wind shear over the MDR is particularly notable since strong El Niño events typically enhance the shear over much of the Caribbean and MDR. During 2023, the MDR SSTAs minus global tropical SSTAs were still positive (Fig. 4.24c), dampening potential El Niño teleconnections. The record-warm SSTs in the Atlantic and low surface pressure reduced the trade winds (Fig. 4.26c), combined with some persistent anticyclonic flow and northeasterly anomalies at 200 hPa over the MDR (Fig. 4.6) contributed to a reduction of the vertical wind shear over the MDR.
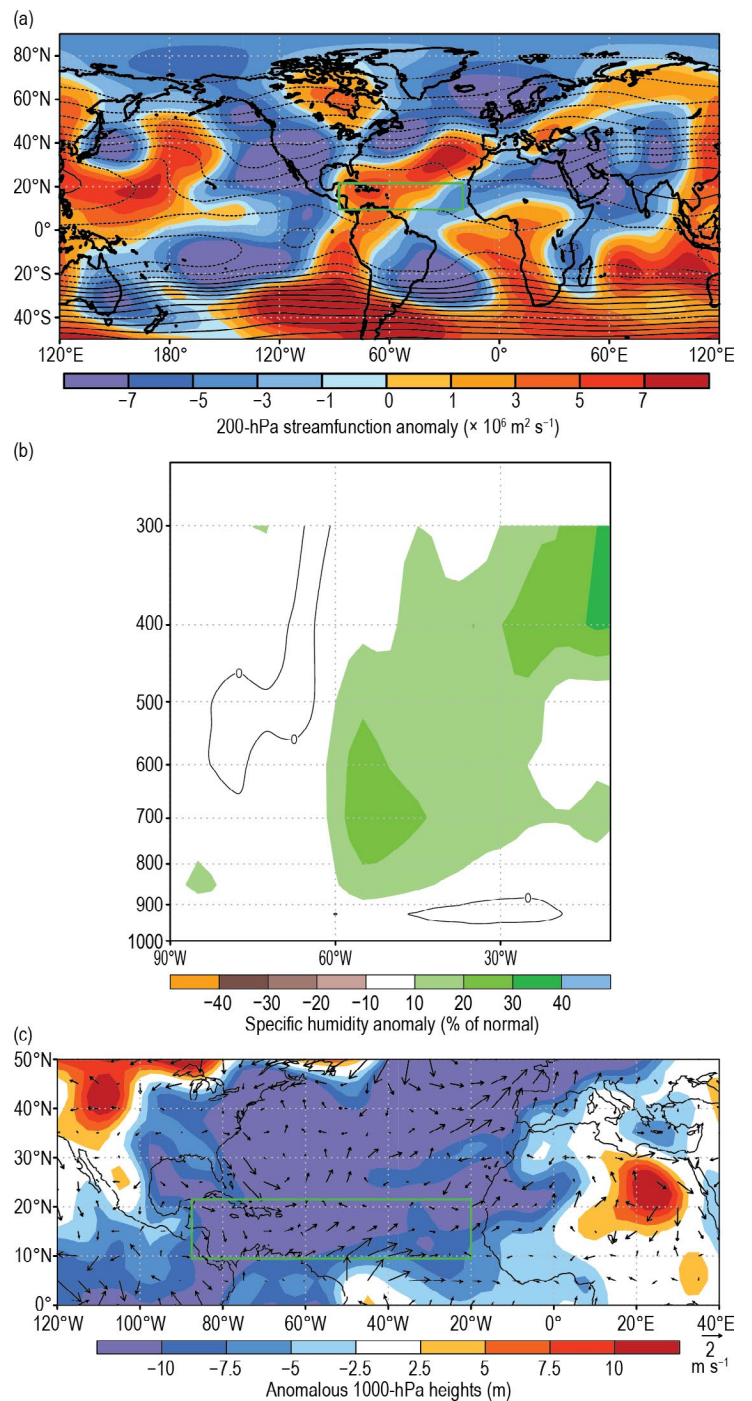
Fig. 4.26. (a) Aug–Oct 200-hPa streamfunction (contours, interval is 5 × 10⁶ m² s⁻¹) and anomalies (shaded); (b) Aug–Oct 2023 Main Development Region (MDR)-specific humidity deviations from normal (%). Brown (green) shading represents below- (above-) normal values, with the thin black line representing no deviation; (c) Aug–Oct anomalous 1000-hPa heights (shaded, m) and vector winds (m s⁻¹). The green box denotes the Atlantic MDR. Anomalies are departures from the 1991–2020 means. (Source: National Centers for Environmental Prediction [NCEP]/National Center for Atmospheric Research [NCAR] reanalysis [Kalnay et al. 1996].)

(v) Unique aspects of the 2023 Atlantic hurricane season

The below-normal TC activity over the Gulf of Mexico and subtropical Atlantic were probably related to high vertical wind shear, since the shear over the Gulf of Mexico was at its highest value since 2017 and is likely related to El Niño (Goldenberg and Shapiro 1996). El Niño conditions are typically related to lower levels of tropical cyclone activity in the Atlantic (Gray 1984), though the ACE in 2023 was above normal and the total count for named storms was well above normal. The count of named storms was the highest on record during a year with a strong El Niño. The El Niño-linked impacts in 2023 are less coherent in the initial analyses than in other El Niño years. Vertical wind shear was below normal (Fig. 4.27a) in the MDR, and mid-level moisture was above normal for most of the MDR (Fig. 4.26b), but anomalous subsidence was evident over the western portions. Additionally, although the named storm activity was relatively high, the fraction of named storms that developed into hurricanes was low (35%) compared to the average (53%). The fraction of hurricanes that became major hurricanes (43%) was close to the average (40%). The proximal cause of the lower relative fraction could be due to El Niño-related subsidence impacting intensification. The supportive influence of record-high SSTs and above-normal mid-level moisture (not present during 2022) could have been enough to promote more tropical cyclone formations, while the detrimental impacts from El Niño (higher vertical wind shear over the Gulf of Mexico and anomalous subsidence over the western MDR) might have limited intensification for several of these tropical cyclones, keeping the number of major hurricanes to near-average and the ACE to just slightly above average.

Fig. 4.27. Aug–Oct (ASO) magnitude of the 200-hPa–850-hPa vertical wind shear (m s⁻¹): (a) 2023 anomalous magnitude and vector, and (b),(c) time series of ASO vertical shear magnitude (black) and five-point running mean of the time series (red) averaged over (b) the Main Development Region (MDR; spanning 85°W–20°W and 10°N–21.5°N) and (c) the western Gulf of Mexico (spanning 80°W–97.5°W and 21.5°N–30°N). Anomalies are departures from the 1991–2020 means. (Source: National Centers for Environmental Prediction [NCEP] National Center for Atmospheric Research [NCAR] reanalysis [Kalnay et al. 1996].)

The unnamed subtropical storm that developed in January was the first system to develop before May since Tropical Storm Arlene in April 2017 and the first January Atlantic storm formation since Hurricane Alex in 2016.

3. EASTERN NORTH PACIFIC AND CENTRAL NORTH PACIFIC BASINS
K. M. Wood and C. J. Schreck

(i) Seasonal activity

Tropical cyclone activity in this section is combined from the two agencies responsible for issuing advisories and warnings in the eastern North Pacific (ENP) basin: NOAA's National Hurricane Center in Miami, Florida (for the region from the Pacific Coast of North America to 140°W), and NOAA's Central Pacific Hurricane Center in Honolulu, Hawaii (for the region between 140°W and the dateline, known as the Central North Pacific [CNP]).

A total of 17 named storms formed within the combined ENP/CNP basin in 2023, 10 of which became hurricanes and 8 became major hurricanes (Fig. 4.28a). This activity was near normal for named storms and above normal for hurricanes and major hurricanes compared with the
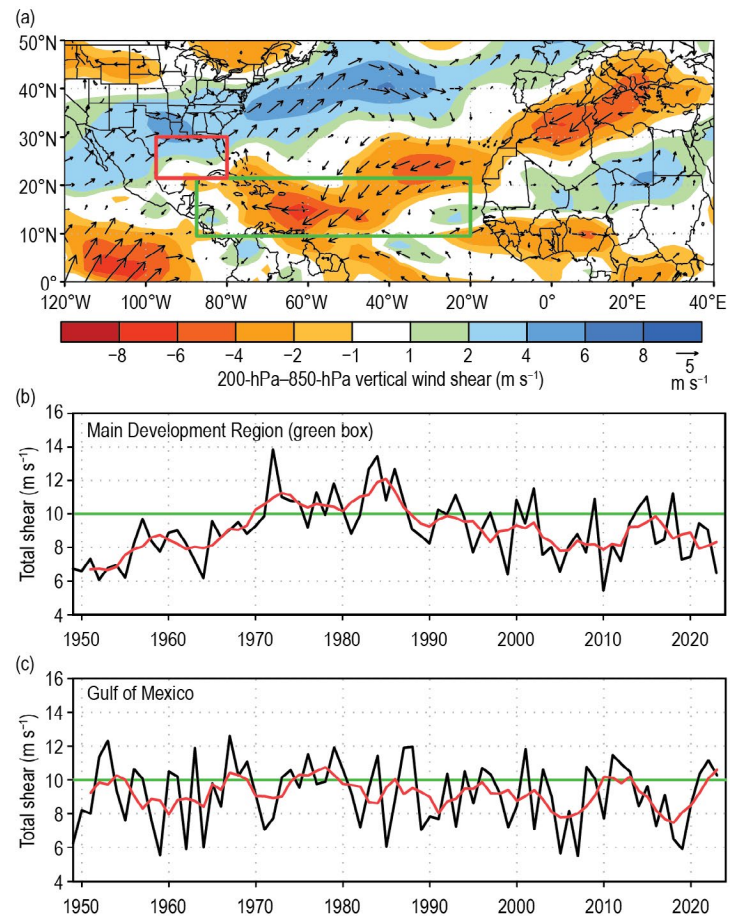
1991–2020 averages of 16.9 named storms, 8.8 hurricanes, and 4.6 major hurricanes. All storms in 2023 occurred between the official ENP hurricane season start date of 15 May and end date of 30 November. The first named storm of the season, Hurricane Adrian, marked the second-latest first formation on record (27 June) after Tropical Storm Agatha in 2016 (2 July). The final named storm, Tropical Storm Ramon, weakened to a tropical depression on 26 November. No named storms formed within the CNP, but three ENP TCs crossed 140°W (Calvin, Dora, and Greg), which is near the 1991–2020 average of 3.4 named storms for the CNP.

The 2023 seasonal ACE index was 165×10^4 kt^2, which was 124% of the 1991–2020 mean of 133×10^4 kt^2 (Fig. 4.28b; Bell et al. 2000), breaking a four-year streak of below-normal activity (Wood and Schreck 2020, 2021, 2022, 2023). Almost half of the season's activity occurred during August (49%) from three tropical storms (Eugene, Greg, and Irwin) and three major hurricanes (Dora, Fernanda, and Hilary). In contrast, July contributed 10% of the season's ACE compared with an average of 22%, and September ACE was 11% compared with an average of 24%. October 2023 marked an increase in TC activity, producing 22% of the season's ACE (October average ACE is 13%). The eight 2023 ENP TCs that reached major hurricane intensity (≥96 kt; 49 m s^{-1}) on the Saffir-Simpson Hurricane Wind Scale contributed about 84% of the season's total ACE: Calvin, Dora, Fernanda, Hilary, Jova, Lidia, Norma, and Otis.
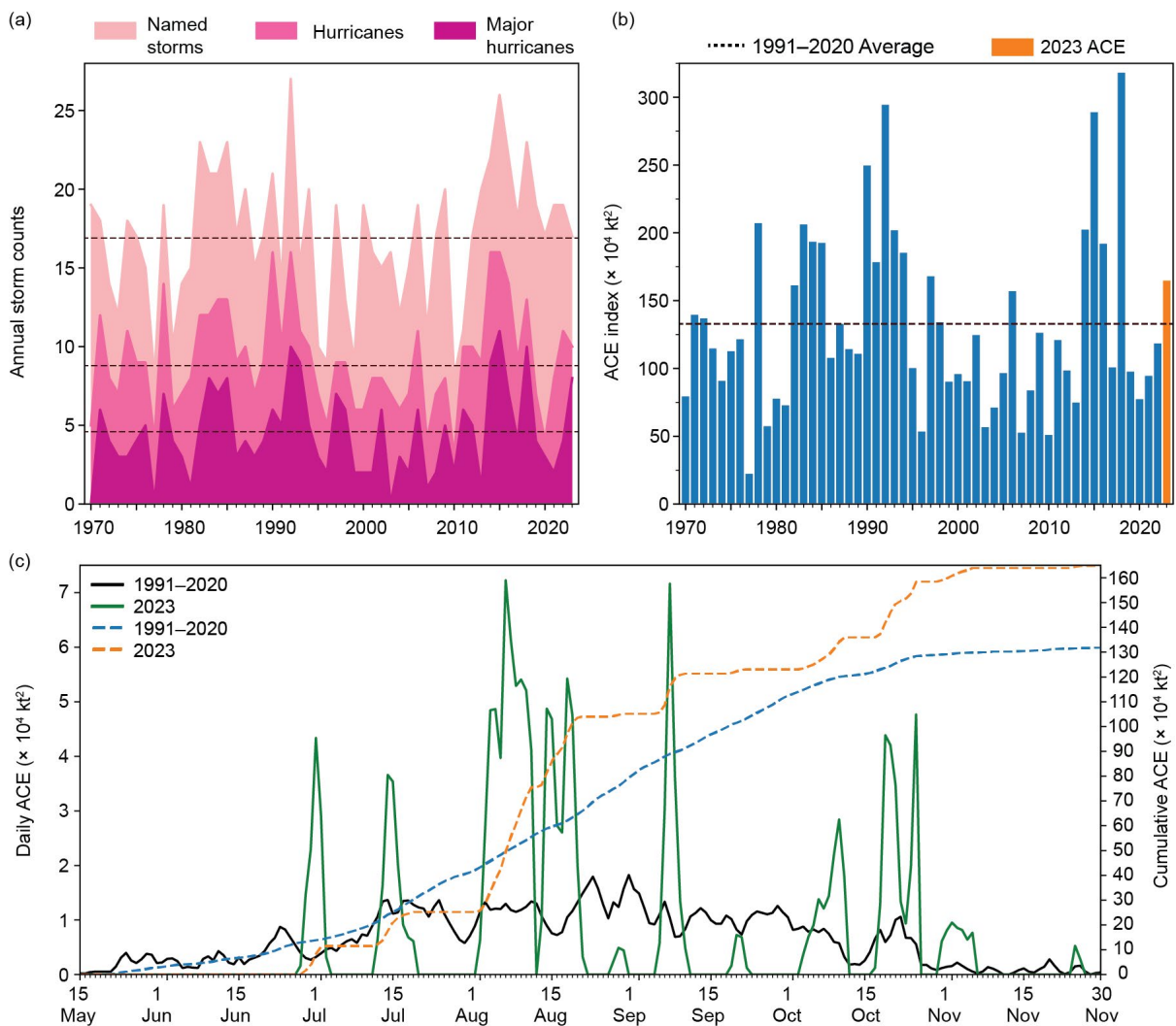
Fig. 4.28. (a) Annual eastern North Pacific and central North Pacific storm counts by category during the period 1970–2023, with the 1991–2020 average by category denoted by dashed lines. **(b)** Annual accumulated cyclone energy (ACE) during 1970–2023, with 2023 highlighted in orange, and the 1991–2020 average denoted by the dashed line. **(c)** Daily ACE for the 1991–2020 average (solid black line) and during 2023 (solid green line); accumulated daily ACE for the 1991–2020 average (dashed blue line) and during 2023 (dashed orange line).

(ii) Environmental influences on the 2023 season

Positive SST anomalies related to a strengthening El Niño event characterized the equatorial eastern Pacific during the 2023 ENP hurricane season. Accompanying these positive SST anomalies were 850-hPa westerly wind anomalies, which predominated over the region east of 140°W (Fig. 4.29). Though TCs generally formed north of the largest SST anomalies, they largely occurred in regions of relatively warm water, below-normal vertical wind shear, and below- or near-normal OLR anomalies. Most TCs tracked within the region of below-normal wind shear and above-normal SSTs, generally dissipating once they reached both anomalously and climatologically cooler SSTs, along with positive wind shear anomalies west of 120°W. The below-normal SSTs in the subtropical central Pacific were unusual for a strong El Niño and may have limited the TC activity there. Only Calvin approached Hawaii as a weakening tropical storm, and Dora's longevity was likely supported by its relatively low-latitude track maintaining proximity to warmer water and away from higher wind shear.

The formation and life cycle of ENP TCs can be influenced by the Madden-Julian Oscillation (MJO) as well as convectively coupled equatorial Kelvin waves (e.g., Maloney and Hartmann 2001; Aiyyer and Molinari 2008; Schreck and Molinari 2011; Ventrice et al. 2012a,b; Schreck 2015, 2016). A strong MJO crossed the Pacific in late July and early August, which likely contributed to unusually high August activity, including the formations of Fernanda, Greg, and Hilary. The subsequent suppressed MJO phase probably played a role in the relatively quiet conditions in September. Another active MJO may have contributed to the October formation of Lidia, Max, Norma, Otis, and Pilar, with passing equatorial Kelvin waves also enhancing these October TC formations (Fig. 4.30). A Kelvin wave may have also favored Adrian's development since cyclogenesis is generally favored within three days
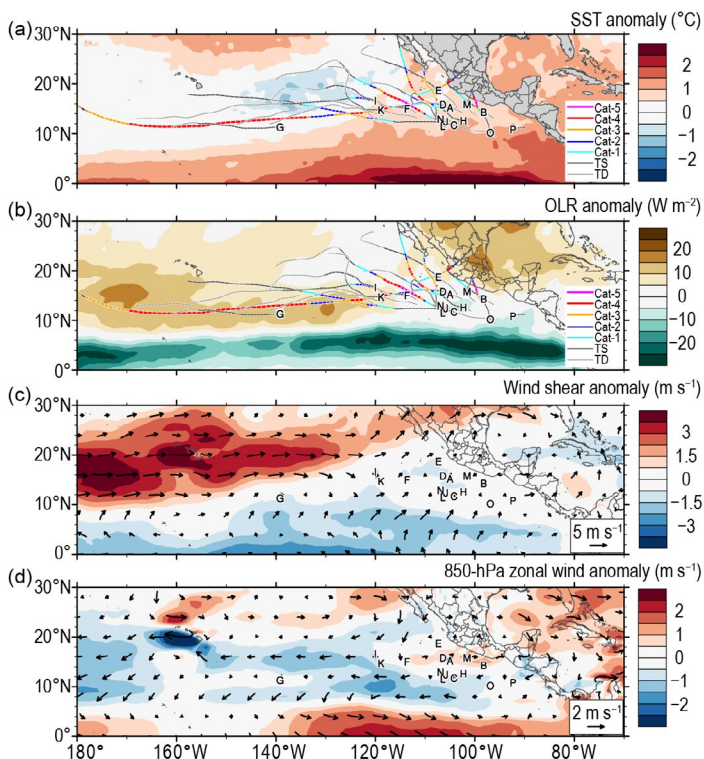
Fig. 4.29. 15 Jun–30 Nov 2023 anomaly maps of (a) sea-surface temperature (SST; °C, Banzon and Reynolds 2013), (b) outgoing longwave radiation (OLR; W m⁻²; Schreck et al. 2018), (c) 200-hPa–850-hPa vertical wind shear (m s⁻¹) vector (arrows) and scalar (shading) anomalies, and (d) 850-hPa wind (m s⁻¹, arrows) and zonal wind (shading) anomalies. Anomalies are relative to the annual cycle from 1991–2020. Letters denote where each tropical cyclone attained tropical storm intensity. Wind data are obtained from CFSR (Saha et al. 2014).
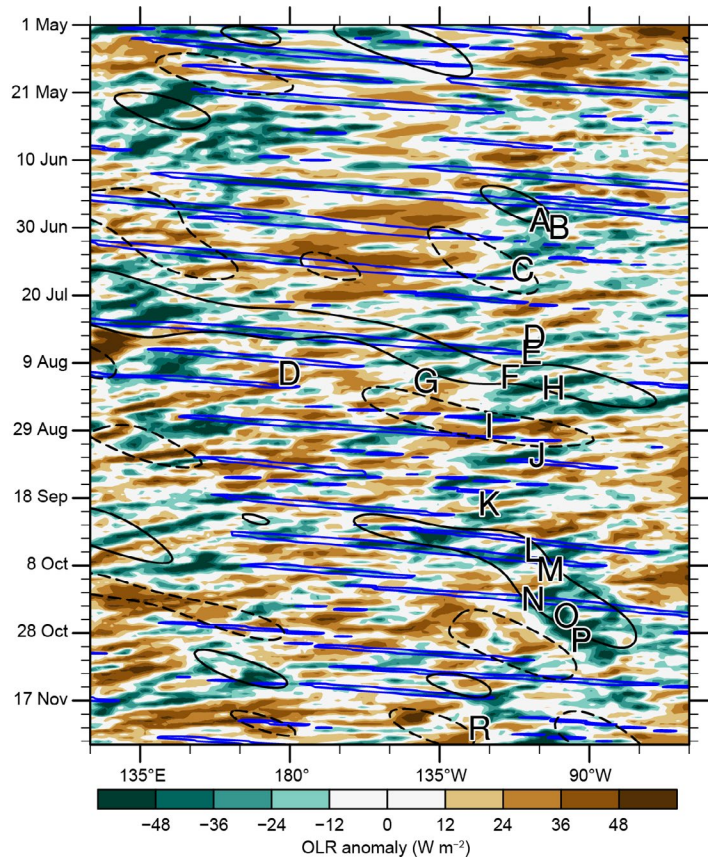
Fig. 4.30. Longitude–time Hovmöller diagram of 5°N–15°N average outgoing longwave radiation (W m⁻²; Schreck et al. 2018). Unfiltered anomalies from a daily climatology are shaded. Negative anomalies (green) indicate enhanced convection. Anomalies filtered for Kelvin waves are contoured in blue at –10 W m⁻² and Madden-Julian Oscillation-filtered anomalies are contoured in black at ±10 W m⁻² (dashed for positive, solid for negative). Letters denote the longitude and time when each tropical cyclone attained tropical storm intensity.

after a Kelvin wave passage. In addition, easterly wave activity as denoted by westward-moving (negative) OLR anomalies in Fig. 4.30 likely contributed to the genesis of many ENP TCs, including Calvin, Dora, Hilary, Jova, and Lidia.

(iii) Notable ENP tropical cyclones and impacts in 2023

Eight TCs exceeded the major hurricane threshold in 2023, nearly double the 1991–2020 average of 4.6. Two hurricanes achieved Category 5 intensity: Jova and Otis.

Of the eight major hurricanes, four made landfall: Norma and Hilary made landfall after weakening, and Lidia and Otis made landfall near peak intensity. Three additional TCs made landfall or directly impacted land: Hurricane Beatriz and Tropical Storms Max and Pilar. Of these seven storms, all but Pilar hit Mexico, making 2023 the third consecutive season during which landfalling ENP TC activity well exceeded the average for Mexico (1.8; Raga et al. 2013; Wood and Schreck 2022, 2023). Likely related in part to below-average wind shear and above-average SSTs, all eight major hurricanes exhibited periods of rapid intensification (≥30 kt; 15.4 m s^{-1} in 24 hours). In fact, the two hurricanes that did not reach major hurricane strength, Adrian and Beatriz, also reached this intensification threshold. Of the 10 TCs that peaked as either hurricanes or major hurricanes, 7 underwent at least one rapid weakening period while over the open ocean (≤−30 kt or −15.4 m s^{-1} in 24 hours; Wood and Ritchie 2015): Adrian, Calvin, Dora, Fernanda, Hilary, Jova, and Norma.

The 2023 ENP hurricane season exemplified the range of intensities at which TCs affecting land can produce significant impacts. Heavy rain from Beatriz caused isolated flooding in Mexico while the system was making landfall as a tropical storm (Blake 2024). Hurricane Dora spent an estimated 132 hours at Category 4 intensity and may have affected strong winds in Hawaii that impacted devastating wildfires in August, though Dora's exact role has yet to be quantified. Hurricane Hilary peaked as a Category 4 storm and weakened prior to landfall in Baja California but prompted the first-ever tropical storm warning for the U.S. state of California, with damage largely due to heavy rain estimated at $675 million (U.S. dollars; Aon 2024). Hurricane Lidia made landfall with estimated winds of 120 kt (62 m s^{-1}), tying Hurricane Kenna from 2002 as the fourth-strongest storm to make landfall in Mexico. Damage was estimated in the tens of millions of U.S. dollars (Aon 2024). Two deaths were attributed to Tropical Storm Max, and rain from this TC affected communities in Guerrero, Mexico, that were impacted by Hurricane Otis two weeks later (Berg 2024). Though Hurricane Norma rapidly weakened prior to landfall, the storm caused estimated economic losses of $50 million (U.S. dollars; Aon 2024), largely attributed to flooding and mudslides due to heavy rainfall. Hurricane Otis caused $12–$16 billion (U.S. dollars) in economic losses (Reinhart and Reinhart 2024) when it devastated Acapulco as a Category 5 hurricane (see Fig. SB4.1). Its estimated landfall intensity of 140 kt (70 m s^{-1}) broke the record for the strongest ENP TC landfall previously held by Hurricane Patricia (2015). Finally, Tropical Storm Pilar dumped heavy rain in Central America when it stalled offshore of El Salvador, with damage estimated at $40 million (U.S. dollars; Aon 2024).

4. WESTERN NORTH PACIFIC BASIN
S. J. Camargo

(i) Overview

This was the fourth consecutive season with below-normal activity in the western North Pacific (WNP) for most measures of tropical cyclone (TC: tropical storms and typhoons) activity. Figure 4.31 compares the activity for 2023 as identified by both the JTWC and the Japan Meteorological Agency (JMA) with their climatologies for 1991–2020. Only 17 storms reached tropical-storm intensity in 2023 (bottom quartile <23; Fig. 4.31a) based on the JTWC (best-track dataset for 1945–2022, preliminary operational data for 2023), matching the number in 1951 and close to the historical lows of 2010 (14) and 1946 (15), the only two years with fewer storms in the historical record. From these, 12 reached typhoon intensity (bottom quartile <13), with 3 reaching super-typhoon status (≥130 kt, bottom quartile <3), matching exactly the number of typhoons and super typhoons in 2022. This corresponds to 71% of the tropical storms intensifying into typhoons (top quartile >69%), with 25% of the typhoons reaching super-typhoon intensity (median: 29%). These statistics include Typhoon Dora, which formed in the eastern North

Pacific, where it was named Hurricane Dora. Dora then tracked across the dateline into the WNP. There were also two tropical depressions (bottom quartile <2) in 2023. The JMA also recorded 17 TCs (bottom quartile <23; Fig. 4.31b), including 5 tropical storms (bottom quartile <5), 2 severe tropical storms (bottom quartile <4), and 10 typhoons (bottom quartile <11). 58.8% of the storms reached typhoon intensity (top quartile >59%). Similar to other years, there were some differ-
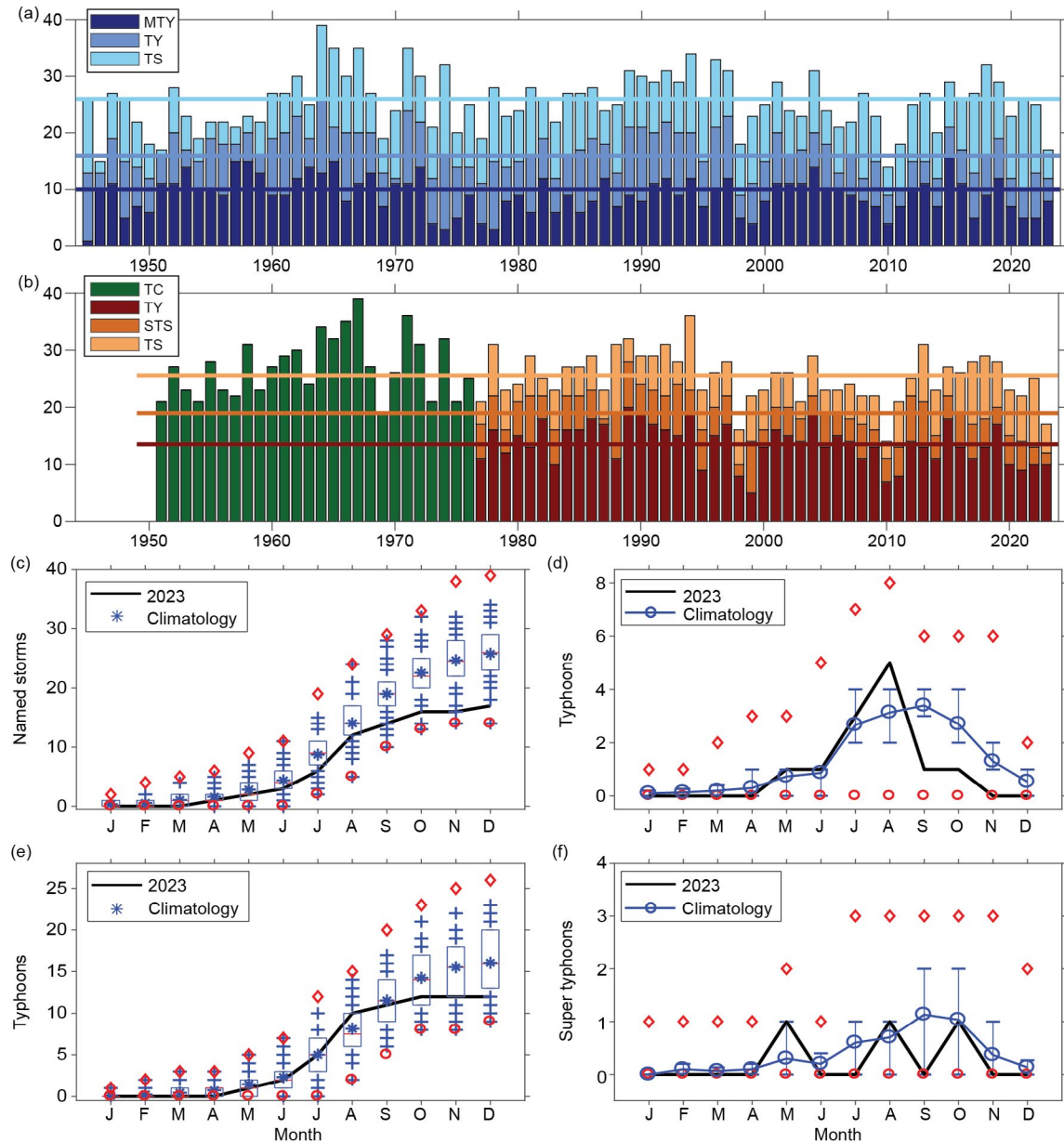
Fig. 4.31. (a) Number of tropical storms (TS), typhoons (TY), and major typhoons (MTY ≥96 kt) per year in the western North Pacific (WNP) for the period 1945–2023 based on the Joint Typhoon Warning Center. (b) Number of tropical cyclones (TCs, all storms that reach TS intensity or higher) from 1951 to 1976; number of TS, severe tropical storms (STS) and TY from 1977 to 2023 based on the Japan Meteorological Agency (JMA). (c) Cumulative number of tropical cyclones with TS intensity or higher (named storms) per month in the WNP in 2023 (black line), and climatology (1991–2020) as box plots (interquartile range: box, median: red line, mean: blue asterisk, values in the top or bottom quartile: blue crosses, high [low] records in the 1945–2022 period: red diamonds [circles]). (e) As in (c) but for the number of typhoons. (d),(f) Number of typhoons and super typhoons (≥130kt), respectively, per month in 2023 (black line) and the climatological mean (blue line). The red diamonds and circles denote the maximum and minimum monthly historical records, and the blue error bars show the climatological interquartile range for each month (in the case of no error bars, the upper and/or lower percentiles coincide with the median). (Sources: 1945–2022 Joint Typhoon Warning Center [JTWC] best-track dataset, 2023 JTWC preliminary operational track data for panels [a], [c], [d], [e], and [f]. 1951–2023 Regional Specialized Meteorological Centre-Tokyo, JMA best-track dataset for panel [b].)

ences between the JTWC and JMA storm counts, intensities, and categories[3]. Talim and Damrey were considered typhoons by the JTWC and severe tropical storms by JMA. Seventeen TCs correspond to the third-lowest value in the JMA record. The only years with less TC activity were 2010 (14) and 1998 (16). The Philippine Atmospheric, Geophysical and Astronomical Services Administration (PAGASA) named 10 TCs that entered its area of responsibility, including Tropical Depression Amang (10–13 April), which was not numbered or named by either the JMA or the JTWC.

(ii) Seasonal activity

The 2023 typhoon season had a late start, with the first storm (Tropical Storm Sanvu) forming on 19 April. The next formation, Super Typhoon Mawar, was in late May, followed by Typhoon Guchol in June. The early season (January–June) had a total of 3 TCs (bottom quartile <3), with 2 typhoons (median: 2) and 1 super typhoon (top quartile >1). The cumulative monthly number of TCs and typhoons for 2023 are depicted in Figs. 4.31c,e, respectively, with the number of typhoons and super typhoons per month displayed in Figs. 4.31d,f. In Figs. 4.31c–f, the 2023 values are compared against the climatological values, as well as the historical maxima and minima.

Three typhoons were present in the WNP basin in July (median: 3): Typhoons Talim, Doksuri, and Khanun. August was the most active month of the season, with a total of 6 TCs (top quartile >6), including Tropical Storm Kirogi (30 August–4 September) and Hurricane/Typhoon Dora (31 July–22 August). Hurricane Dora formed in the eastern North Pacific and crossed the central Pacific basin before reaching the dateline and being renamed Typhoon Dora, remaining at hurricane/typhoon intensity across the three basins. Dora was the second storm in the historical record to achieve this feat, following Hurricane John in 1994. Besides Typhoon Dora, 4 other typhoons were active in August, for a total of 5 (top quartile >4). Only 2 TCs formed in September (bottom quartile <3), including just one typhoon. The formation of a single typhoon in September (bottom quartile <3) has occurred only six times previously (1950, 1983, 1984, 2002, 2004, and 2020); no typhoons occurred in September 1960. Tropical Depression #13 was also active in September. October also had only 2 TCs (bottom quartile <2) and 1 typhoon (bottom quartile <2). In total, the peak season (July–October) had 13 TCs (bottom quartile <16), including 10 typhoons (bottom quartile <9) and 2 super typhoons (bottom quartile <2).

The season ended quietly as well. Tropical Depression #17 was the only storm active in November, and Tropical Storm Jelawat was the only storm in December. The late typhoon season (November and December) had therefore 1 tropical storm (bottom quartile <2) and no typhoons (bottom quartile <1).

In contrast with the diagnostics for TC counts, the total ACE in 2023 (Fig. 4.32a) was
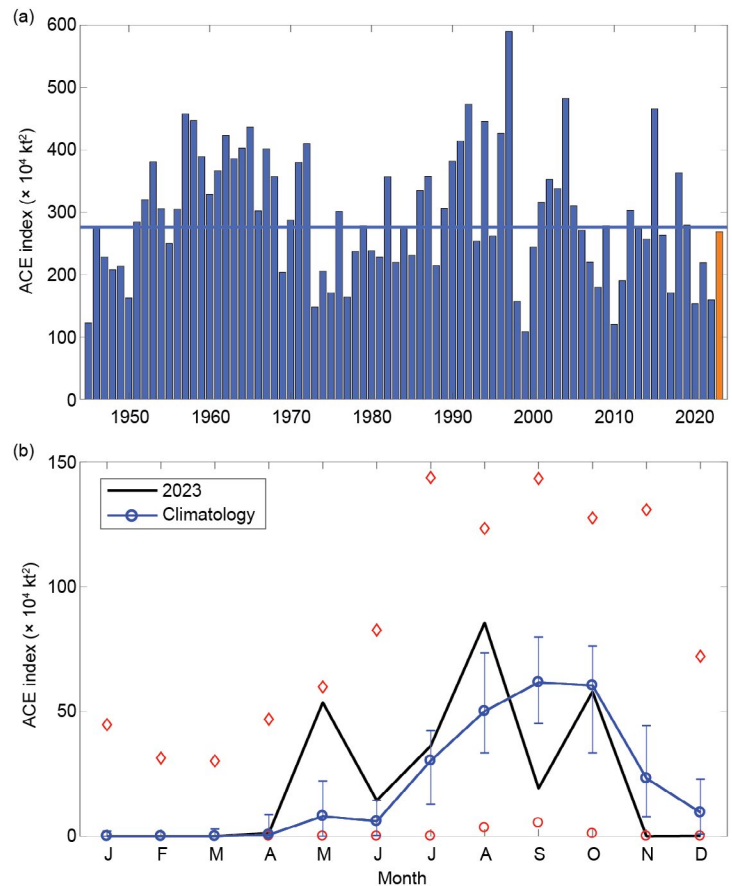
Fig. 4.32. (a) Accumulated cyclone energy (ACE; × 10⁴ kt²) per year in the western North Pacific for the period 1945–2023. The solid blue line indicates the median for the climatology (1991–2020). (b) ACE per month in 2023 (black line) and the median during 1991–2020 (blue line), the blue error bars indicate the climatological interquartile range. In the case of no error bars, the upper and/or lower percentiles coincide with the median. The red diamonds and circles denote the maximum and minimum values per month during the 1945–2022 period. (Source: 1945–2022 Joint Typhoon Warning Center [JTWC] best-track dataset; 2023 JTWC preliminary operational track data.)

---

[3] It is well known that there are systematic differences between the JMA and JTWC datasets, which have been extensively documented in the literature (e.g. Knapp et al. 2013; Schreck et al. 2014).

close to the median of the climatological distribution due to the occurrence of eight typhoons that reached Category 3 (major) intensity on the Saffir–Simpson Hurricane Wind Scale, with three of these reaching super-typhoon status (maximum intensity >130 kt). As noted earlier, of the 17 TCs that formed in 2023, 12 reached typhoon intensity. Therefore, since ACE is dominated by the storms' intensity (e.g., the square of the maximum wind speed), this led to a near-normal value of ACE, despite the low number of TCs. ACE was zero in January, February, March, and November and in the bottom quartile in September and December. October ACE was close to the climatological median, while ACE was above the climatological median in April and July. In May, June, and August, ACE was in the top quartile. A super typhoon was active during each of these months: Mawar in May, Saola in August, and Bolaven in October. ACE was in the top quartile in the early season, below the median in the peak season, and in the bottom quartile in the late season. The ACE value in the late season was the second lowest in the historical record, above only 2010, which had zero ACE in that period. Typically, high seasonal ACE values are typical of El Niño events in the WNP basin (Camargo and Sobel 2005), in contrast to 2023. Strong and long-lived typhoons are typical of El Niño events, leading to high ACE values. While there were several strong typhoons in 2023, the low number of total storms contributed to a near-normal ACE value.

Seven typhoons in 2023 had ACE values in the top quartile of the ACE for individual storms' climatological distribution: Mawar, Doksuri, Khanun, Lan, Saola, Koinu, and Bolaven. The ACE values of Super Typhoons Saola and Mawar were in the 95th and the 99th percentile of the climatological distribution, respectively. The ACE value of Super Typhoon Mawar was the 13th highest in the historical record (since 1945). These two super typhoons combined to produce 37.3% of the total ACE of the 2023 season.

Typically, during El Niño events, the typhoon genesis location is shifted to the southeast part of the WNP basin (Chia and Ropelewski 2002; Camargo and Sobel 2005; Camargo et al. 2007a). This shift in genesis location contributes to long tracks, strong storms, and high ACE values. The mean genesis position in 2023 was 14.2°N and 136.8°E, northwest of the climatological mean of 13.3°N and 140.5°E, with standard deviations of 1.9 and 7.7, respectively. These values exclude storms that formed in the eastern and central North Pacific, such as Dora in 2023. Therefore, the mean genesis position in 2023 (see July–October [JASO] 2023 storms' genesis and track locations in Figs. 4.33a,b) did not display the typical mean southeast shift of other El Niño events in the 1950–2022 period (mean genesis position of 12.6°N and 144.0°E). Similarly, the mean track position in 2023 (18.3°N, 129.0°E) was northwest of the mean climatological track position (17.8°N, 135.9°E, with standard deviations of 1.6 and 5.2, respectively).

In 2023 there were 83 days with active TCs (bottom quartile <86 days). Of these, 52 days had active typhoons (median: 52.4 days) and 27.75 days had active major typhoons (SSHWS categories 3–5; median: 23 days). The percentage of active days with typhoons and major typhoons was 53.1% (top quartile >41.3%) and 28.3% (top quartile >18.5%), respectively. In other words, while the total number of days with TCs in 2023 was low, a high percentage of these had active typhoons or major typhoons. The median TC lifetime in 2023 was 7 days (bottom quartile <7 days) and that of typhoons was 8.9 days, matching the climatological median. Hurricane/Typhoon Dora had the longest lifespan in 2023 (18.5 days), but only 4 of those days were in the western North Pacific basin. Of the storms that spent their whole lifetime in the basin, Super Typhoon Mawar had the longest lifetime (14.5 days), followed by Typhoon Khanun (14 days). Super Typhoon Saola (11 days) and Typhoon Koinu (10.75 days) also reached the top quartile of the lifetime climatological distribution (>10 days). From 30 August to 2 September, there were three storms active simultaneously in the basin: Super Typhoon Saola, Typhoon Haikui, and Tropical Storm Kirogi. The historical record for most active TCs in the WNP simultaneously is six, set in August 1996.

(iii) Environmental conditions

Figure 4.33 shows the environmental conditions and tracks during the peak typhoon season (JASO). In early 2023, a third successive year of La Niña conditions was still present, which then

transitioned to El Niño in April–June. The event was classified as a strong El Niño by August–October (section 4b). Therefore, during the peak typhoon season, there were El Niño conditions influencing the overall characteristics of the TC season. The SST anomalies (Fig. 4.33a) show a typical El Niño pattern, with above-normal SST anomalies in the equatorial region, east of 152°E, surrounded by cooler, albeit still above-normal, SST. There was also a region of high SST anomalies north of 30°N with a maximum around 40°N near the coast of Asia and north of Japan. The typhoon tracks in JASO 2023 (Fig. 4.33a) are located in the western part of the basin north of 10°N, except Hurricane/Typhoon Dora, which originated in the ENP basin.
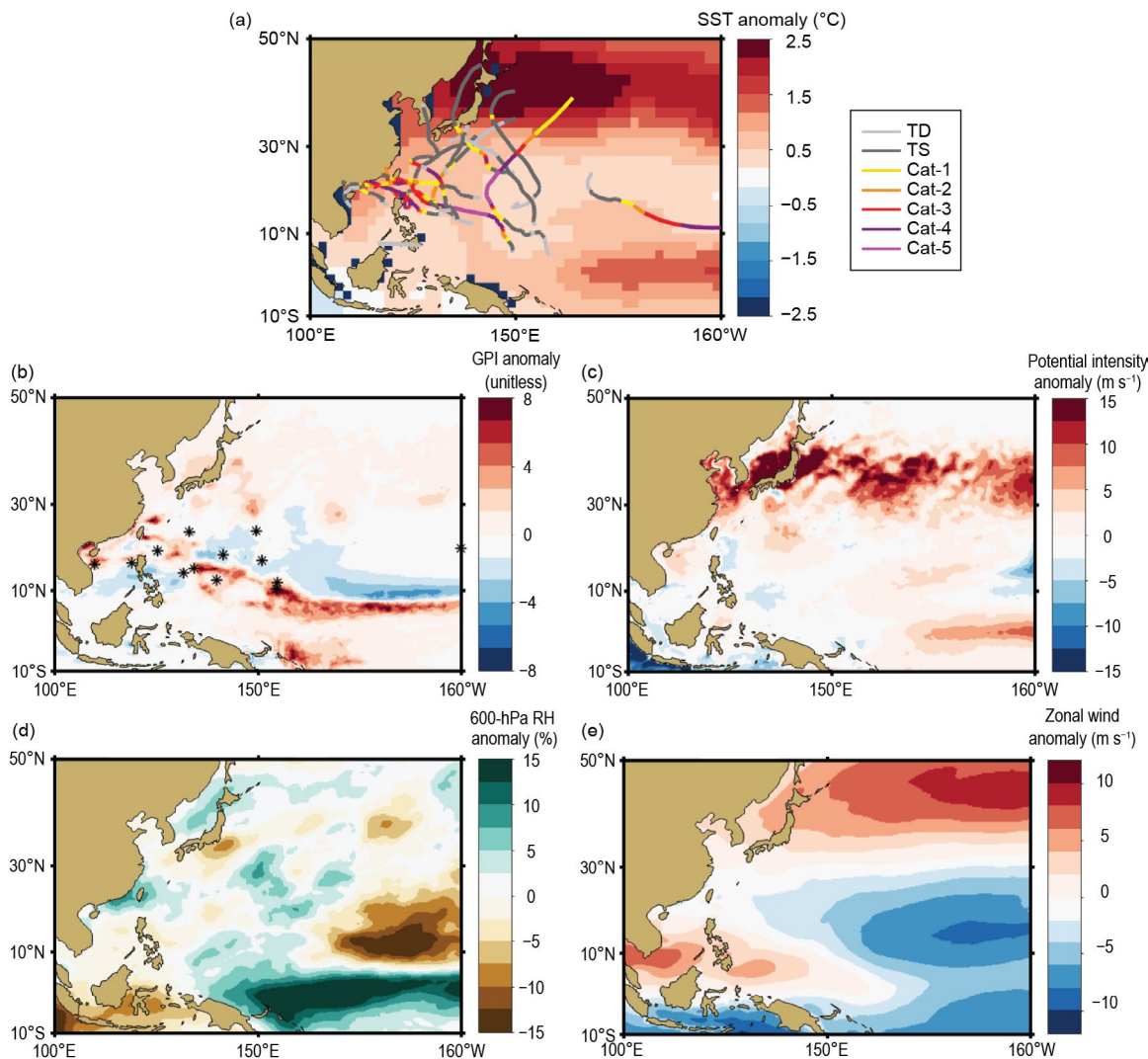
Fig. 4.33. Jul–Oct (JASO) 2023: (a) Sea-surface temperature (SST) anomalies (°C) and the tracks of all 2023 storms (including tropical depressions [TDs], tropical storms [TSs], and typhoon-strength storms [Cat]), with colors denoting their intensity, (b) genesis potential index anomalies and first position of JASO 2023 storms marked with an asterisk, (c) potential intensity anomalies (m s⁻¹), (d) 600-hPa relative humidity anomalies (%), and (e) zonal winds at 850-hPa (m s⁻¹). (Data sources: SST: ERSSTv5 [Huang et al. 2017]; other environmental fields: ERA5 reanalysis [Hersbach et al. 2020]; tracks and first position: Joint Typhoon Warning Center preliminary operational track data.)

The genesis potential index (Fig. 4.33b; Emanuel and Nolan 2004; Camargo et al. 2007b) expresses the enhanced or reduced probability of TC formation through a nonlinear empirical combination of environmental factors known to affect TC genesis. The genesis potential index anomalies have a bimodal pattern, with a narrow zonal region of positive anomalies south of 10°N and negative anomalies north of that. The region of positive genesis anomalies shifted northward in the western part of the basin, where the TCs formed in those months. The potential

intensity anomalies (Fig. 4.33c; Emanuel 1988) reflect the SST pattern, with positive anomalies in the equatorial region in the eastern part of the basin and a large zonal region of positive anomalies centered on 40°N.

Similar to the genesis potential index, the relative humidity anomalies present a zonal dipole pattern (Fig. 4.33d) in the eastern portion of the basin, with dry anomalies north of 10°N and wet anomalies to the south and east of the Maritime Continent. The monsoon trough, which is defined by the 850-hPa zonal winds anomalies, tends to expand eastward in El Niño events. In 2023, the positive zonal wind anomalies (Fig. 4.33e) encompassed the region from the South China Sea to east of the Philippines. Tropical cyclones tend to form in the edge of the monsoon trough. This was again the case in 2023, with some TCs forming on the northern edge of the monsoon trough.

These environmental conditions help explain the low levels of activity in 2023, as only a small area in the WNP basin had environmental conditions conducive to genesis formation (i.e., high SST, potential intensity, and mid-level relative humidity) during the peak typhoon season. Furthermore, a strong subtropical high and suppressed MJO activity contributed to the low level of typhoon activity in 2023, and the tropical cyclone heat potential values discussed in section 4h may shed some light on this low number of TCs. Several recent papers have related the decrease in TC activity in the WNP in the last few years to decadal variability (e.g., Zhao et al. 2018, 2020; Chan and Liu 2022).

(iv) Impacts

In 2023, 11 storms (including TCs) made landfall in the WNP basin (bottom quartile <15, climatology 1961–90). From these, 2 made landfall as tropical depressions (median: 5), 3 made landfall as tropical storms (bottom quartile <8), 4 made landfall as Saffir-Simpson Category 1–2 typhoons (Talim, Doksuri, Lan, and Saola; median: 4), and 2 made landfall as major typhoons (Haiku and Koinu; median: 2). Here, landfalls are defined as instances when the center of a storm that is over the ocean moves over land. The observed TC tracks were interpolated into 15-minute intervals, and we then used a high-resolution land mask in order to determine the occurrence of landfall. In our analysis, we only considered the highest-intensity landfall event for each storm in cases of multiple landfalls.

The largest impacts from the 2023 typhoon season were caused by Typhoon Doksuri (named Egay in the Philippines), which affected the northern Philippines and China, leading to $18.4 billion (U.S. dollars) in economic losses (Gallagher Re 2024). The remnants of Typhoon Doksuri led to high rainfall rates, causing floods and landslides in northern China, in particular in the Beijing area. The total rainfall from the storm in Beijing was 744.8 mm in a 40-hour period, which was the heaviest in the 140-year record, according to the China Meteorological Administration. The resulting floods caused 137 deaths and displaced 92,000 people in China and 313,000 in the Philippines, in addition to causing numerous power outages and a lack of running water across the region, according to Relief Web.

5. NORTH INDIAN OCEAN BASIN
J. Uehling and C. J. Schreck
(i) Seasonal activity

The North Indian Ocean (NIO) TC season typically occurs between April and December, with two peaks of activity: May–June and October–December, due to the presence of the monsoon trough over tropical waters of the NIO during these periods. Tropical cyclone genesis typically occurs in the Arabian Sea and the Bay of Bengal between 8°N and 15°N. The Bay of Bengal, on average, experiences four times more TCs than the Arabian Sea (Dube et al. 1997).

The 2023 NIO TC season had 8 named storms according to the JTWC, which was above the IBTrACS JTWC 1991–2020 climatology of 5.5. Two of those reached tropical storm strength according to the JTWC but were considered depressions by the India Meteorological Department. Four storms reached cyclone strength, and three of those reached major cyclone strength. These values were above the climatological average of 2.2 cyclones and well above the average of

1.1 major cyclones (Fig. 4.34). The 2022 seasonal ACE index (January–December) of 57.5×10^4 kt^2 was more than double the 1991–2020 mean of 24.7×10^4 kt^2.

Conditions were particularly favorable during the pre-monsoon period (May–June) when two of the major cyclones occurred. Sea-surface temperatures were unusually warm across the basin, with large anomalies in the Arabian Sea (Fig. 4.35a). Convection was also enhanced in the Arabian Sea, where Very Severe Cyclone Biparjoy formed (Fig. 4.35b). The Indian monsoon was delayed; thus, convection was generally suppressed over India and the Bay of Bengal where Super Cyclone Mocha formed. The delayed monsoon was associated with below-normal vertical wind shear southward from around 16°N–18°N to the equator (Fig. 4.35c). Low-level easterlies dominated the basin throughout the season (Fig. 4.35d). The conditions for tropical cyclones overall were favorable with low shear and high SSTs, which helped to explain the enhanced activity this year. These favorable factors were enough to overcome the drier and less convec-tively favorable conditions in the Bay of Bengal. During the post-monsoon period, the Indian Ocean dipole became strongly positive. The associated high SSTs in the Arabian Sea provided conditions conducive to the development of Very Severe Cyclone Tej's intensity.

Fig. 4.34. (a) North Indian Ocean (NIO) tropical cyclone tracks in 2023. (b),(c) Annual tropical cyclone statistics for the NIO basin for the period 1990–2023: (b) number of named storms, cyclones, and major cyclones, and (c) accumulated cyclone energy (ACE; × 10^4 kt^2). Horizontal lines, representing the 1991–2020 climatology, are included in both (b) and (c).
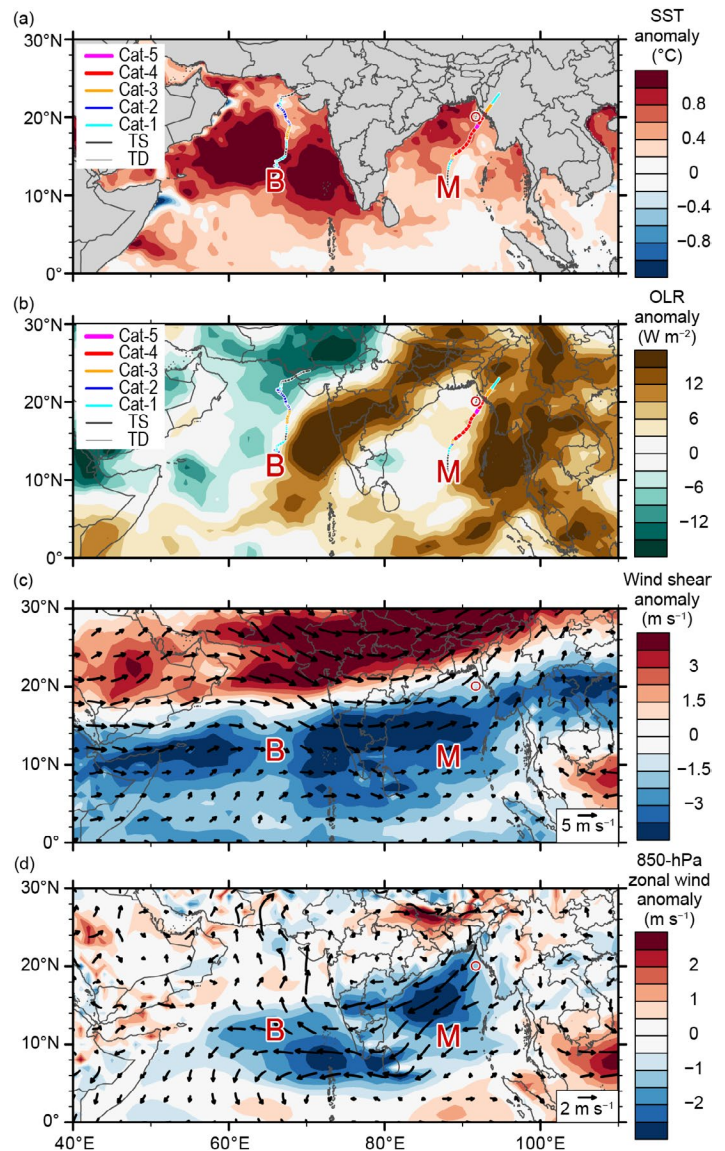
Fig. 4.35. May–Jun 2023 North Indian Ocean (NIO) anomaly maps of: (a) sea-surface temperature (SST; °C; Banzon and Reynolds 2013), (b) outgoing longwave radiation (OLR; W m^{-2}; Schreck et al. 2018); (c) 200-hPa–850-hPa vertical wind shear (m s^{-1}) vector (arrows) and scalar anomalies (shading), and (d) 850-hPa winds (m s^{-1}, arrows) and zonal wind anomalies (shading). Anomalies are relative to the annual cycle for 1991–2020. Letter symbols denote where each NIO tropical cyclone attained its initial tropical storm intensity, and the red circle represents an unnamed tropical storm. (Source: wind data from CFSR [Saha et al. 2014].)

(ii) Individual tropical cyclones and impacts

The North Indian Ocean cyclone season began on 11 May with the formation of Super Cyclonic Storm Mocha. This was also the strongest storm of the year in the basin, with winds peaking at 140 kt (72 m s^{-1}) and a minimum central pressure of 918 hPa, equivalent to a Category 5 hurricane on the SSHWS. Super Cyclone Mocha made a catastrophic landfall in Myanmar, causing over $1 billion (U.S. dollars) in damage and hundreds of fatalities between Myanmar and Bangladesh (Aon 2024). In June, the second major cyclone of the year, Very Severe Cyclone Biparjoy formed in the Arabian Sea and peaked with sustained winds of 105 kt (54 m s^{-1}). The storm made landfall in India after weakening to a tropical storm and comparatively minor impacts were felt. Very Severe Cyclone Tej, the final major cyclone of the year, occurred from 20 to 23 October. The storm peaked as a Category 3 equivalent over the Arabian Sea with maximum sustained winds of 110 kt (57 m s^{-1}) and a minimum pressure of 956 hPa. The cyclone brought flooding rains as it passed near the island of Socotra and caused minor impacts after landfall as a weakening tropical storm in Yemen.

The final cyclone-strength storm of the year was Severe Cyclone Hamoon, which peaked with winds of 80 kt (41 m s^{-1}) and a central pressure of 978 hPa. Hamoon occurred during late October over the Bay of Bengal and made landfall as a cyclone in Bangladesh. Hamoon brought heavy rainfall, strong winds, and storm surge to the country, resulting in numerous fatalities and extensive damage (Aon 2024). Late in the year, Cyclone Midhili and Cyclone Michaung caused flooding and damages after landfalls in Bangladesh and India, respectively.

6. SOUTH INDIAN OCEAN BASIN
A. D. Magee and C. J. Schreck

(i) Seasonal activity

The South Indian Ocean (SIO) TC basin extends south of the equator from the east African coastline to 90°E. While tropical cyclone activity can occur year-round, the peak season is typically between November and April when the Intertropical Convergence Zone is situated in the Southern Hemisphere. The 2022/23 season includes TCs that occurred from July 2022 to June 2023. Landfalling TCs typically impact Madagascar, Mozambique, and the Mascarene Islands, including Mauritius and La Réunion; however, impacts can be felt in other locations within the region.

A below-average storm count during the 2022/23 season was observed in the SIO basin, with 9 named storms according to the JTWC, compared to the IBTrACS-JTWC 1991–2020 mean of 10.4 (Fig. 4.36). There were 7 cyclones, of which 4 became major cyclones, above-normal compared to a 1991–2020 mean of 6.0 and 3.5, respectively. The season had an earlier-than-normal start, with Tropical Storms Ashley and Balita developing in September and October, respectively.
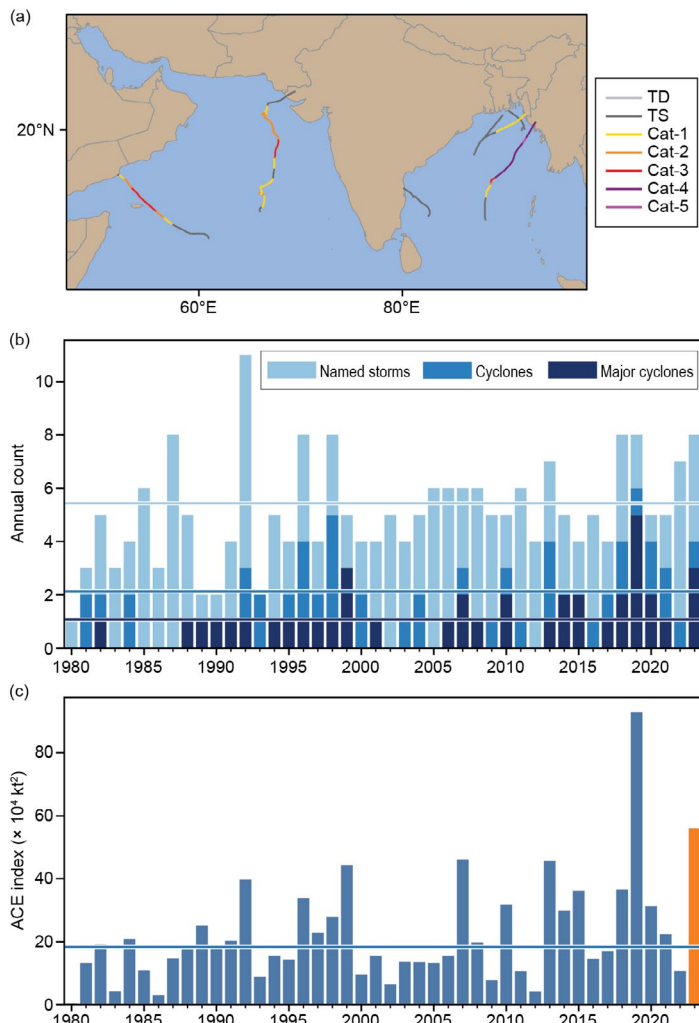

Fig. 4.36. (a) South Indian Ocean (SIO) tropical cyclone tracks in 2023. (b),(c) Annual tropical cyclone statistics for the SIO basin for the period 1980–2023: (b) number of named storms, cyclones, and major cyclones, and (c) accumulated cyclone energy (ACE; × 10^4 kt^2). Horizontal lines, representing the 1991–2020 climatology, are included in both (b) and (c).
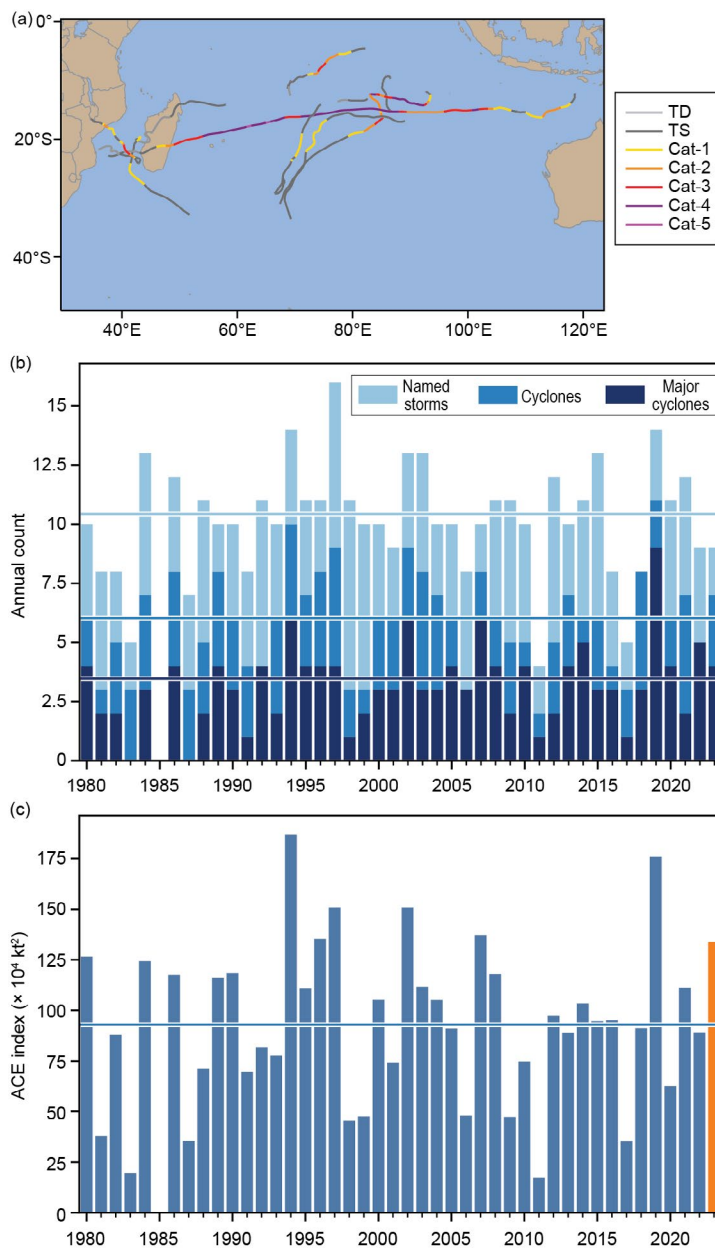
The 2022/23 seasonal ACE index was 133.7 × 10⁴ kt², which is 142% of the 1991–2020 climatology of 94.3 × 10⁴ kt². Cyclone-favorable conditions, including anomalously high SSTs, were present to the northeast of Madagascar and south of 20°S (Fig. 4.37a), and favorable wind shear anomalies persisted across much of the basin between December and March (Fig. 4.37c).

(ii) Noteworthy tropical cyclones and impacts

The first tropical cyclone of the 2022/23 SIO TC season, Severe Tropical Cyclone Darian, initially began to the north of Cocos (Keeling) Islands in the Australian western region. On 21 December, the system passed into the SIO basin as a highly compact Category 4 tropical cyclone on the SSHWS. The system tracked southwest and then west, where it temporarily weakened. Darian then began intensifying again, reaching its peak intensity on 23 December, with maximum sustained winds of 135 kt (69 m s⁻¹) and a minimum central pressure of 922 hPa, a Category 4 system on the SSHWS. Darian continued to move on a southwesterly track, and on 28 December the system was downgraded to a tropical storm.

Tropical Cyclone Cheneso, the second tropical cyclone of the 2022/23 SIO TC season, formed on 16 January to the south of Diego Garcia. The system tracked southwest as it intensified to a severe tropical storm before making landfall across northern Madagascar, where it weakened. When Cheneso emerged into the Mozambique Channel, it briefly intensified into a Category 1 tropical cyclone on the SSHWS, reaching a peak intensity with sustained winds of 80 kt (41 m s⁻¹) and a minimum central pressure of 967 hPa on 28 January. Tropical Cyclone Cheneso resulted in 33 fatalities and widespread damage to over 10,000 homes as well as several healthcare and school facilities. Damage was estimated to total around $20 million (U.S. dollars).

Fig. 4.37. 15 Dec 2022–15 Mar 2023 Southern Indian Ocean (SIO) anomaly maps of: (a) sea-surface temperature (SST; °C; Banzon and Reynolds 2013), (b) outgoing longwave radiation (OLR; W m⁻²; Schreck et al. 2018); (c) 200-hPa–850-hPa vertical wind shear (m s⁻¹) vector (arrows) and scalar anomalies (shading), and (d) 850-hPa winds (m s⁻¹, arrows) and zonal wind anomalies (shading). Anomalies are relative to the annual cycle for 1991–2020. Letter symbols denote where each SIO tropical cyclone attained its initial tropical storm intensity (Source: wind data from CFSR [Saha et al. 2014]).

Severe Tropical Cyclone Freddy was a remarkable and record-breaking tropical cyclone that traversed the southern Indian Ocean for over five weeks in February and March 2023, establishing itself as one of the longest-lasting tropical cyclones on record (see Sidebar 4.2). Freddy alone accounted for about half of the ACE in the South Indian Ocean in 2022/23.

The final TC of the season, Severe Tropical Cyclone Fabien, formed from an active pulse of the Madden-Julian Oscillation, which initiated conditions conducive for cyclone development. Emerging from a low-pressure system on 8 May, the system began to intensify, organizing into a tropical disturbance by 13 May. Fabien tracked southwest from the central Southern Indian
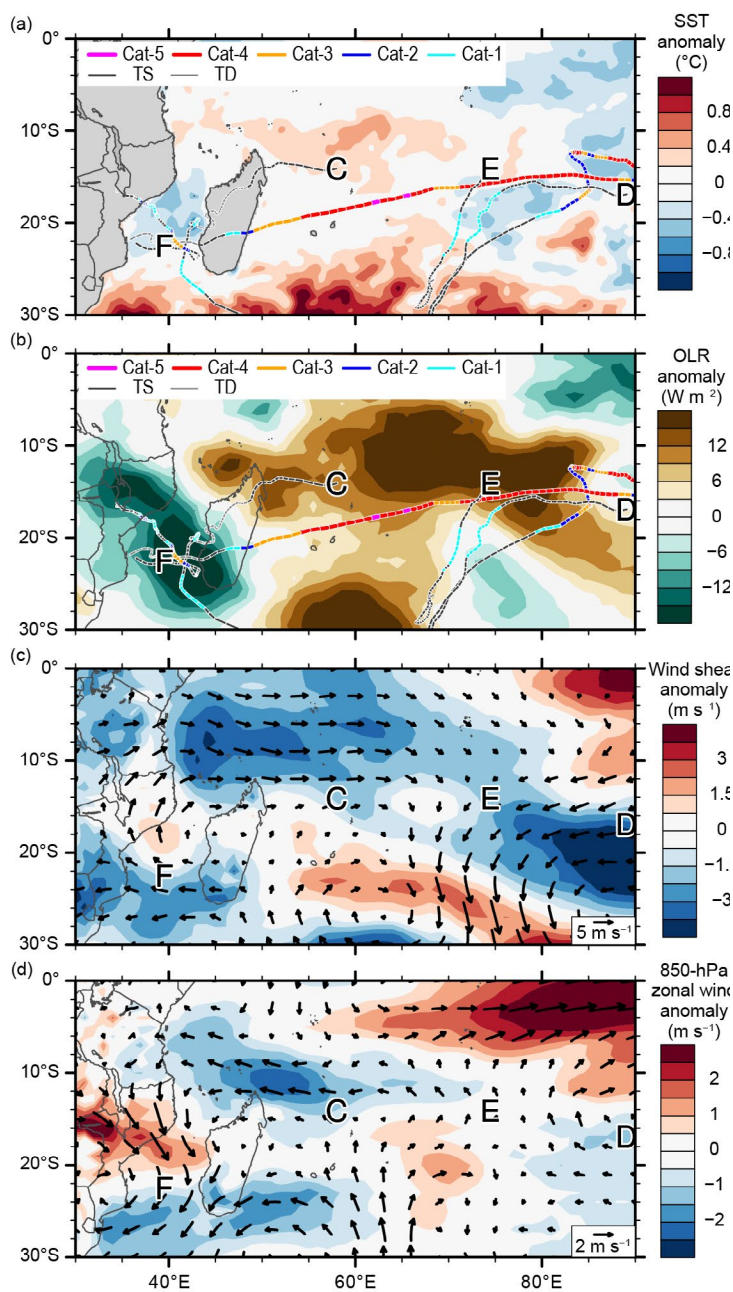
Ocean and reached its peak intensity with sustained winds of 100 kt (51 m s^{-1}) and a minimum central pressure of 962 hPa on 16 May—a Category 3 system on the SSHWS. Although the system did not make landfall, high waves caused a fishing boat to capsize, resulting in 16 fatalities.

7. AUSTRALIAN BASIN

B. C. Trewin and L. Paterson

(i) Seasonal activity

The 2022/23 TC season was below average in the broader Australian basin (areas south of the equator and between 90°E and 160°E[4], which includes Australian, Papua New Guinea, and Indonesian areas of responsibility). The season produced 7 TCs, well below the 1991–2020 average[5] of 9.5. This reduction in activity was atypical for a season with weak to moderate La Niña conditions and equaling 2011/12 as having the lowest number of cyclones in a La Niña season on record. The 1991–2020 IBTrACS seasonal averages for the basin are 10.2 named storms, 5.0 TCs, and 2.5 major TCs, which compares with the 2022/23 IBTrACS-based counts of 9, 7, and 4, respectively (Fig. 4.38). Two of those storms reached tropical storm strength according to the JTWC but were considered tropical lows by the Australia's Bureau of Meteorology.

There were five TCs in the western sector[6] of the broader Australian region, one in the northern sector, and one in the eastern sector during 2022/23. Three of the seven cyclones reached Australian Category 5 intensity within the Australian basin, and a fourth did so after leaving the basin.

(ii) Landfalling and other significant tropical cyclones

Fig. 4.38. (a) Australian tropical cyclone tracks in 2023. (b),(c) Annual tropical cyclone statistics for the Australian basin for the period 1980–2023: (b) number of named storms, cyclones, and major cyclones, and (c) accumulated cyclone energy (ACE; × 10^4 kt^2). Horizontal lines, representing the 1991–2020 climatology, are included in both (b) and (c).

There were two landfalls in mainland Australia during the season at tropical cyclone intensity: Ellie in the Northern Territory in December and Ilsa in Western Australia in April. Ellie reached tropical cyclone intensity on 22 December while off the west coast of the Northern Territory Top End and made landfall as a Category 1 system near the Daly River mouth later the same day. While Ellie only spent a short period as a tropical cyclone, the post-landfall tropical low persisted for more than two weeks, initially over areas of the Northern Territory south of the landfall point and then moving west into the Kimberley region of Western Australia, finally dissipating after returning to the central Northern Territory on 8 January.

[4] The Australian Bureau of Meteorology's warning area overlaps both the southern Indian Ocean and southwest Pacific.

[5] References to cyclone category in this section are to the Australian scale (http://www.bom.gov.au/cyclone/tropical-cyclon e-knowledge-centre/understanding/categories/), which differs from the Saffir-Simpson scale.

[6] The western sector covers areas between 90°E and 125°E. The eastern sector covers areas east of the eastern Australian coast to 160°E, as well as the eastern half of the Gulf of Carpentaria. The northern sector covers areas from 125°E east to the western half of the Gulf of Carpentaria. The western sector incorporates the Indonesian area of responsibility, while the Papua New Guinea area of responsibility is incorporated in the eastern sector.

The tropical low brought heavy rainfall along its path, with especially high accumulations in the Kimberley region due to the slow movement of the system. Totals exceeding 400 mm for the week ending 3 January were widespread, with Dimond Gorge, 70 km northeast of Fitzroy Crossing, reporting the highest total of 830.2 mm, including 355.6 mm on 2 January. Major flooding occurred over large parts of Western Australia and the Northern Territory. The Fitzroy River at Fitzroy Crossing reached a new high peak of 14.23 m, 0.27 m above the previous record. The main road bridge at Fitzroy Crossing collapsed, severing the only wet-season link through the region until a temporary crossing could be built in late March. Many other transport links were also severely disrupted. Numerous Aboriginal communities were evacuated to larger towns.

Ilsa reached named TC intensity north of Broome on 11 April and intensified steadily over the following 48 hours as it moved southwest, reaching Category 5 intensity at 0600 UTC on 13 April about 180 km north of Port Hedland. The storm then turned southeast and made landfall around 1600 UTC that day near Pardoo Station, east of Port Hedland. The landfall was near peak intensity with maximum sustained 10-minute winds estimated at 124 kt (64 m s^{-1}), the first Australian scale Category 5 landfall in Australia since Marcia in 2015 (and in Western Australia since Laurence in 2009). Bedout Island recorded 10-minute sustained winds of 119 kt (61 m s^{-1}) and a maximum gust of 156 kt (80 m s^{-1}), both of which were the highest values observed at a Bureau of Meteorology site in Australia, although higher values have been observed at non-Bureau sites (Courtney et al. 2012). Ilsa weakened rapidly as it moved inland, with the remnant low dissipating near the Northern Territory border early on 15 April. The landfall was in a sparsely populated area, with the main impact being the destruction of the Pardoo Roadhouse, along with significant damage to nearby pastoral stations. Nine fishermen were reported missing at sea after their vessel sank near Rowley Shoals and were presumed drowned.

In addition to Ilsa, two other cyclones off the Western Australian coast reached Category 5 intensity: Darian, which was within the region from 18 to 21 December with a peak 10-minute wind speed of 124 kt (64 m s^{-1}), and Herman, which peaked at 115 kt (59 m s^{-1}) during its lifetime from 29 March to 2 April. Neither system approached land areas or had any known impacts. Freddy, which formed northwest of Broome on 6 February and reached Category 4 intensity on 12 February with 10-minute winds of 115 kt (49 m s^{-1}), left the Australian region on 14 February and subsequently reached Saffir-Simpson Category 5 intensity in the South Indian Ocean basin, becoming the world's longest-lived tropical cyclones (see Sidebar 4.2). While it had no known impacts in the Australian region, Freddy had major impacts in Africa (section 4g6). Gabrielle, the season's only TC in the eastern region, peaked at Australian Category 3 intensity on 10 February before leaving the region, subsequently crossing the Australian territory of Norfolk Island (with minor damage) and having major impacts in New Zealand as a post-tropical cyclone (section 4g8).

8. SOUTHWEST PACIFIC BASIN
A. D. Magee and A. M. Lorrey

(i) Seasonal activity

The 2022/23 southwest Pacific tropical cyclone season officially began in November 2022 and ended in April 2023. The data for the season were gathered from the Fiji Meteorological Service, Australia's Bureau of Meteorology, and New Zealand MetService, Ltd. The Southwest Pacific basin, as defined by Diamond et al. (2012) as 135°E–120°W, experienced a total of four TCs, including three severe storms. One storm was considered to be a tropical storm by the JTWC, but a tropical depression by the WMO RSMC in Fiji. In comparison to the 1991–2020 seasonal average of 9.8 named tropical cyclones, including 4.3 severe storms, as reported by SPEArTC, the 2022/23 southwest Pacific TC season was considered to be below normal. Despite this, the 2022/23 southwest Pacific TC season was the costliest on record in the Southern Hemisphere, primarily due to Severe Tropical Cyclone Gabrielle.

Figure 4.39 illustrates the TC activity in the basin, which spans the area 160°E–120°W to avoid overlap with the Australian basin and double counting of storms. It is important to note that the climatological definition of the southwest Pacific basin (Diamond et al. 2012) is used for this seasonal description and does not align with WMO-designated boundaries for the

BAMS

Regional Specialized Meteorological Center's nor the Tropical Cyclone Warning Center's areas of responsibility.

(ii) Storm tracks, landfalls, and impacts

Tropical Cyclone Irene, the first tropical cyclone of the 2022/23 southwest Pacific tropical cyclone season, initially formed as a tropical low to the west of Vanuatu on 13 January. The system was named on 18 January to the north of New Caledonia as it continued to track towards the east. Cyclone Irene reached peak intensity as an Australian scale Category 2 tropical cyclone, with sustained winds of 55 kt (28 m s^{-1}) and a minimum central pressure of 980 hPa on 18 January. Irene passed over Tanna Island in Vanuatu and continued to track toward the east-southeast.

The first severe tropical cyclone of the season and the costliest on record in the Southern Hemisphere, Severe Tropical Cyclone Gabrielle, formed on 5 February as a tropical low southeast of the Solomon Islands. Initially moving westward before tracking toward the south, Gabrielle intensified swiftly, becoming an Australian-scale Category 3 severe tropical cyclone on 9 February, reaching its peak intensity with sustained winds of 89 kt (46 m s^{-1}) and a minimum central pressure of 958 hPa the following day. Norfolk Island issued a red alert as Gabrielle neared, and New Zealand extended existing states of emergency in Auckland and the Coromandel due to the cyclone's imminent threat. Although not included in the IBTrACS preliminary track (Fig. 4.39a), the storm impacted New Zealand from 11 to 17 February, prompting a national state of emergency on 14 February for only the third time in the history of the country. Gabrielle tracked in a southeasterly direction in the Bay of Plenty, east of Northland and Auckland, and then followed an east-southeasterly track (not shown). As it passed by Great Barrier Island, a pressure reading of 967 hPa was recorded. Gabrielle brought heavy rain, with 250 mm–400 mm totals recorded across much of the northern part of North Island. Gabrielle was responsible for widespread power outages, and national transport networks were disrupted. There were also mandatory evacuations in some locations due to expected storm impacts. In New Zealand, severe flooding and property damage ensued, with gale-force winds ripping roofs off buildings and causing landslides. In some locations on the eastern seaboard, there was also significant coastal inundation. Fluvial flooding was extensive, and dozens of communities were temporarily cut off due to road closures or from bridges being destroyed. Multiple dams in Hawke Bay burst due to flash flooding, and significant volumes of silt blanketed vineyards and orchards. At some locations, buildings were lifted off their foundations and moved hundreds of meters due to the force of flood-waters. Over 140,000 landslides were recorded post-cyclone. The cyclone's passage through New Zealand left over 225,000 homes without power, thousands of displaced people, and significant infrastructure damage, including to water supplies, roads,
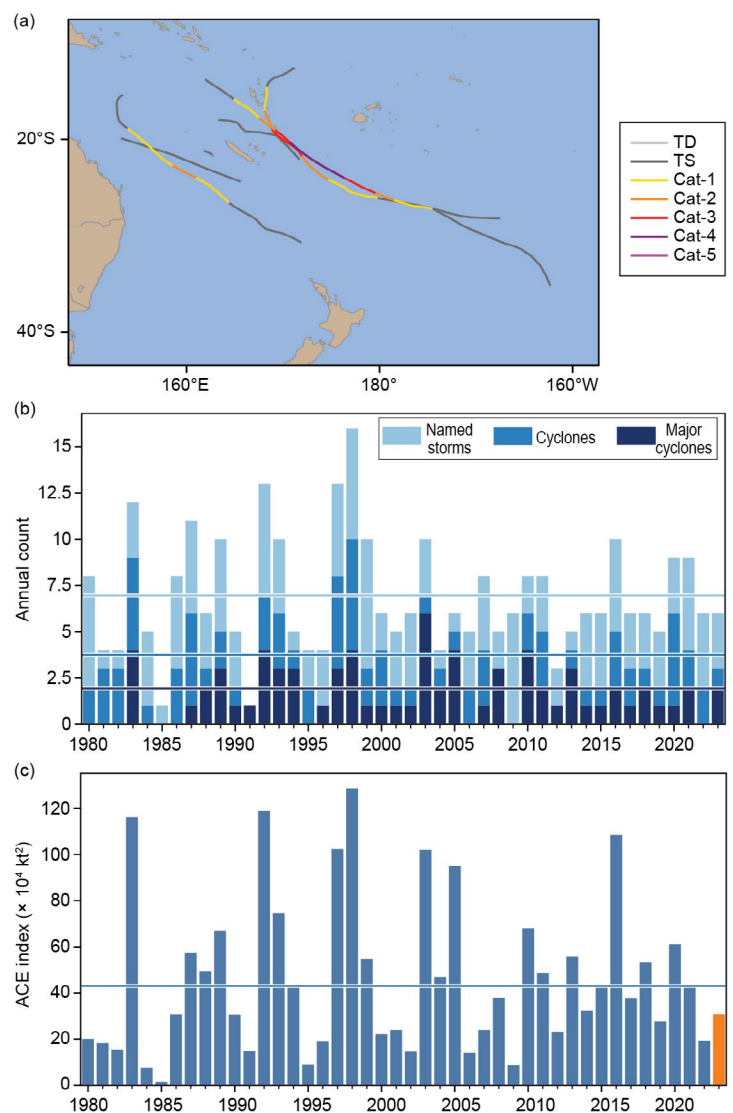

Fig. 4.39. (a) Southwest Pacific tropical cyclone tracks in 2023. (b),(c) Annual tropical cyclone statistics for the southwest Pacific basin for the period 1980–2023: (b) number of named storms, cyclones, and major cyclones, and (c) accumulated cyclone energy (ACE; × 10^4 kt^2). Horizontal lines, representing the 1991–2020 climatology, are included in both (b) and (c).

railways, and bridges. With 11 direct fatalities, Gabrielle became the deadliest New Zealand weather event since 1968 (NIWA 2023). Total damage associated with Gabrielle exceeded $13.5 billion New Zealand dollars ($9.5 billion U.S. dollars), the costliest on record in the Southern Hemisphere to date.

Severe Tropical Cyclone Judy began as a low-pressure system located south of Samoa. Favorable conditions, including moderate wind shear and high sea-surface temperatures, helped the system to organize quickly. The system developed into a tropical cyclone on 27 February near the Solomon Islands and continued to track in a southwesterly direction. As it approached central Vanuatu, Severe Tropical Cyclone Judy reached its peak intensity with sustained winds of 100 kt (51m s^{-1}) and a minimum central pressure of 940 hPa, becoming an Australian-scale Category 4 tropical cyclone on 1 March. The system passed over Shefa Province, close to Port Vila, and made landfall across Tanna Island. Residents in Port Vila were evacuated, and more than 50% of households reported damage. Strong winds brought down communication lines and damaged Vanuatu Central Hospital. The system continued to track towards the southeast, where increasing wind shear weakened the system.

Severe Tropical Cyclone Kevin formed initially within a monsoonal trough near Queensland, Australia. While Cyclone Judy was moving in a south-southeast direction away from the Vanuatu group, Kevin quickly strengthened while tracking toward Vanuatu and underwent rapid intensification promoted by favorable sea-surface temperatures and atmospheric conditions. The system passed over Erromango and Tanna Island in Vanuatu as an Australian scale Category 4 storm on 3 March before reaching its peak intensity the next day, with sustained winds of 125 kt (64 m s^{-1}) and a minimum central pressure of 913 hPa, an Australian-scale Category 5 intensity. The event coincided with a 6.5 magnitude earthquake that struck just west of Espiritu Santo, exacerbating the cyclone's impacts.

Severe Tropical Cyclones Judy and Kevin passed Vanuatu within 48 hours of each other, exacerbating impacts and complicating the humanitarian and emergency response. In total, around two-thirds of the country's population was directly affected. Over 19,000 houses were destroyed or damaged across Malampa, Shefa, and Tafea. Temporary and seasonal crops were also severely impacted, and many home gardens were destroyed. The coffee and commercial fruit and vegetable sectors were also significantly affected. No fatalities were reported; however, property damage of over $400 million New Zealand dollars ($248 million U.S. dollars) was reported, which amounts to about 25% of the gross domestic product for Vanuatu.

h. Tropical cyclone heat potential
— F. Bringas, I-I. Lin, and J. A. Knaff

Tropical cyclone heat potential (TCHP) is an indicator of the amount of heat stored in the upper ocean that can potentially promote tropical cyclone (TC) intensification and regulate ocean–atmosphere enthalpy fluxes and TC-induced sea-surface temperature (SST) cooling (e.g., Lin et al. 2013). TCHP is calculated by integrating the ocean temperature between the sea surface and the 26°C isotherm (D26), which has been reported as the minimum temperature required for TC genesis and intensification (Leipper and Volgenau 1972; Dare and McBride 2011). TCs traveling over regions of high TCHP conditions experience higher heat fluxes from the ocean into the atmosphere, favoring intensification and leading to reduced SST cooling (e.g., Lin et al. 2013). Areas in the ocean with TCHP values above 50 kJ cm^{-2} have been statistically linked with TC intensification, including rapid intensification when the maximum sustained wind speed increases by at least 30 kt in 24 hours in situations in which atmospheric conditions are favorable (e.g., Shay et al. 2000; Mainelli et al. 2008; Lin et al. 2021; Knaff et al. 2018, 2020). In addition to upper-ocean heat content, upper-ocean salinity conditions may also modulate TC intensification as storms traveling over areas of fresh water-induced barrier layers may receive increased air–sea heat fluxes caused by reduced upper-ocean mixing and cooling (e.g., Balaguru et al. 2012; Domingues et al. 2015).

We present an assessment and analysis of the upper-ocean heat content conditions during 2023, based on estimates of two parameters: 1) TCHP (e.g., Goni et al. 2009, 2017) global anomalies with respect to their long-term mean (1993–2022) and 2) TCHP in 2023 compared to conditions observed in 2022. TCHP anomalies during 2023 (Fig. 4.40) are computed for June–November in the Northern Hemisphere and November 2022–April 2023 in the Southern Hemisphere. The seven regions where TCs typically form, travel, and weaken/intensify are highlighted in Fig. 4.40. In all these regions, TCHP values exhibit large temporal and spatial variability due to mesoscale features (e.g., surface currents and associated eddies and rings) and short- to long-term modes of climate variability (e.g., North Atlantic Oscillation, El Niño–Southern Oscillation, and the Pacific Decadal Oscillation). The differences in TCHP anomalies between 2023 and 2022, as depicted in Fig. 4.41, were computed for the primary months of TC activity in each hemisphere as described above.

TCHP anomalies during 2023 exhibited above-average values in all TC regions and basins, including the eastern North Pacific and western North Pacific and the southwest Indian Ocean where, despite smaller areas of negative anomalies, average values in the regions were positive albeit closer to the long-term mean (Fig. 4.40). These positive TCHP anomalies were particularly large in most areas of the North Indian, the southwest Pacific, the North Atlantic, the Gulf of Mexico, and the equatorial regions of the eastern North Pacific where most TCs travel

Fig. 4.40. Global anomalies of tropical cyclone heat potential (TCHP; kJ cm^{-2}) during 2023 computed as described in the text. The boxes indicate the seven regions where TCs typically occur; from left to right: southwest Indian, North Indian, northwest Pacific, southeast Indian, South Pacific, northeast Pacific, and North Atlantic (shown as Gulf of Mexico and tropical Atlantic separately). The green lines indicate the trajectories of all tropical cyclones reaching at least Category 1 (1-minute average wind ≥64 kt) and above during Nov 2022–Apr 2023 in the Southern Hemisphere and Jun–Nov 2023 in the Northern Hemisphere, and purple lines indicate Category 1 TCs that occurred outside these periods. The number above each box corresponds to the number of Category 1 and above cyclones that traveled within that box. Gulf of Mexico is shown in the inset in the lower right corner.

and intensify. TCHP anomalies reached values up to 30 kJ cm^{-2}, which are indicative of favorable oceanic conditions for the development and intensification of TCs. These same regions had TCHP anomalies during 2023 that were more than 20 kJ cm^{-2} larger than in 2023. Meanwhile, the South Indian Ocean, the western North Pacific, and the Bay of Bengal had near- or below-average
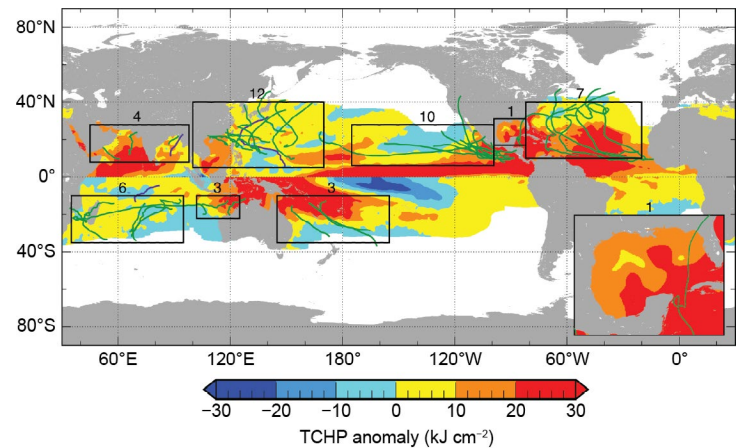
TCHP anomalies during 2023, and their TCHP was lower in 2023 compared to the previous year (Fig. 4.41).

The positive anomalies in the eastern North Pacific and central Pacific equatorial areas, with values during 2023 larger than 50 kJ cm^{-2} compared to 2022 (Fig. 4.41), were associated with the El Niño. In contrast, over the western North Pacific, negative anomalies of –10 kJ cm^{-2} to –20 kJ cm^{-2} as compared to 2022 were observed, consistent with a strong El Niño, which is known to reduce TCHP in the northwest Pacific (Zheng et al. 2015; Lin et al. 2020).

Consistent with the observed slightly above-average TCHP anomalies during 2023 in the region, the 2022/23 southwest Indian Ocean cyclone season was below average in terms of named storms but above average in terms of accumulated cyclone energy (ACE; Fig. 4.40). The most intense

Fig. 4.41. Tropical cyclone heat potential (TCHP) anomaly difference between the 2023 and 2022 tropical cyclone seasons (kJ cm^{-2}; Jun–Nov in the Northern Hemisphere and Nov–Apr in the Southern Hemisphere). The Gulf of Mexico is shown in the inset in the lower right corner.

storm of the season was Cyclone Freddy. During its westward track until making landfall in Madagascar and Mozambique, Freddy weakened and re-intensified repeatedly, completing seven independent cycles of rapid intensification while traveling over areas with SSTs greater than 28°C and a TCHP greater than 40 kJ cm^{-2} (see Sidebar 4.2 for details).

Large positive areas of high TCHP anomaly values, in excess of 30 kJ cm^{-2} from the long-term average, were observed in regions of the southwest Indian and southwest Pacific, where TCs typically form and develop. However, 2022/23 generated near-average TC activity in these regions with a total of six TCs, of which four reached Category 1 intensity or above.

In the North Indian Ocean, above-average TCHP anomalies in excess of 30 kJ cm^{-2} and 10 kJ cm^{-2} were observed during 2023 in the northern Arabian Sea and the southern Bay of Bengal, respectively (Fig. 4.40). The most intense storm was Category 5 TC Mocha, which occurred in May (Fig. 4.40, in purple). After being named in the Bay of Bengal on 9 May, Mocha experienced two cycles of rapid intensification on 12 May and then 13 May, reaching its estimated peak intensity of 1-minute sustained wind speed of 140 kt (72 m s^{-1}) and a minimum central barometric pressure of 918 hPa, according to the Joint Typhoon Warning Center (JTWC), while traveling over extremely favorable oceanic conditions characterized by SSTs greater than 30°C and a TCHP greater than 120 kJ cm^{-2}.

Upper-ocean thermal conditions are largely modulated by the state of the El Niño–Southern Oscillation (ENSO) in the North Pacific Ocean (e.g., Zheng et al. 2015; Lin et al. 2020). While La Niña was predominant in the region during 2022, a shift to El Niño started early in 2023 with the transition occurring by June. El Niño became strong by late 2023 (section 4b). Consistent with this change in the ENSO state, TCHP anomalies were positive in the equatorial region of the eastern North Pacific with values well above 30 kJ cm^{-2}, while in the western North Pacific TCHP anomalies were positive although closer to the long-term mean (Fig. 4.40). Compared to 2022, TCHP anomalies in the eastern North Pacific during 2023 were larger by more than 20 kJ cm^{-2} in the equatorial regions while they were mostly negative by a similar magnitude in the western North Pacific (Fig. 4.41).

Tropical cyclone activity in the western North Pacific in 2023 was relatively low, although seven TCs reached Category 4 or 5 status. Among them, Super Typhoon Mawar was the most intense TC of the northwest Pacific in 2023, with a maximum intensity of 160 kt (82 m s^{-1}), according to the JTWC. Mawar originated and intensified at relatively low latitudes (~15°N) in May. At this low latitude, even in May, TCHP values were still high (~140 kJ cm^{-2}) and could favor Mawar's intensification.

The favorable oceanic conditions for TC intensification noted in the eastern North Pacific likely contributed to the above-average hurricane season observed during 2023. The two most
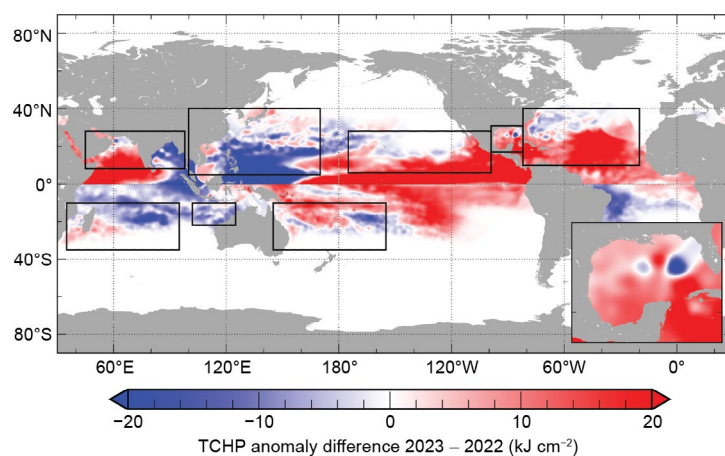
intense TCs of the season were Category 5 Hurricanes Jova and Otis, which underwent short periods of rapid intensification while traveling over regions of similar upper ocean thermal conditions characterized by SSTs greater than 29°C and a TCHP greater than 80 kJ cm^{-2}.

In the North Atlantic basin, upper-ocean thermal conditions during the 2023 hurricane season were characterized by TCHP anomalies larger than the long-term average, except in a reduced area near the northeast coast of the United States, where TCHP anomalies were slightly negative with respect to the long-term mean (Fig. 4.40). In particular, large TCHP anomalies were observed in the southeast portion of the basin west of Africa, the Caribbean Sea and the tropical North Atlantic around Cuba, and the Gulf of Mexico, where TCHP anomalies reached average values of up to 35 kJ cm^{-2} during the season. The same spatial distribution was observed for areas of TCHP anomalies that were larger in 2023 compared to the previous year throughout most of the region (Fig. 4.41), with anomalies in excess of 25 kJ cm^{-2} in the areas with the largest TCHP anomalies during 2023. It is likely that these favorable upper ocean thermal conditions contributed to 2023 being the fourth most active on record for named storm formations, with a total of 20 named storms (Fig. 4.40). The 2023 season was also the most active season on record for a year with a strong El Niño; Category 5 Hurricane Lee was the strongest storm of the season in this region. The system traveled over areas of favorable oceanic conditions with SSTs greater than 30°C and a TCHP greater than 90 kJ cm^{-2}, reaching its estimated peak intensity of 145 kt (75 m s^{-1}) and a minimum central barometric pressure of 926 hPa. Lee rapidly intensified from Category 1 to Category 5 during a 24-hour period with an increase in wind speed of 75 kt (39 m s^{-1}). Despite these favorable oceanic conditions, Lee subsequently weakened due to TC-unfavorable atmospheric conditions, including an increase in vertical wind shear.

In summary, favorable upper-ocean thermal conditions were observed in all TCHP basins during the 2023 season, except for the western North Pacific and southeast Indian Ocean, where conditions were slightly above average compared to the long-term mean. TCHP anomalies during 2023 were higher in most basins compared to the previous year, with the exception of the same two regions (western North Pacific and southeast Indian Ocean basins) where anomalies during 2023 were lower than those of the previous year. TC activity based on the number of named storms was consistent with these thermal conditions for every region. Several storms, including Intense Cyclone Freddy in the southwest Indian, Super Typhoon Mawar in the western North Pacific, Major Hurricanes Jova and Otis in the eastern North Pacific, and Major Hurricane Lee in the North Atlantic underwent rapid intensification, including several independent rapid intensification cycles in some cases, while traveling over areas with favorable oceanic conditions with high SST and TCHP values.

Sidebar 4.1: **Hurricane Otis: The strongest landfalling hurricane on record for the west coast of Mexico**

P. KLOTZBACH, C. FOGARTY, AND R. TRUCHELUT

Hurricane Otis was the strongest hurricane on record to strike the west coast of Mexico, making landfall with maximum winds of 140 kt (75 m s^{-1}) on 25 October (Reinhart and Reinhart 2024). The storm came ashore just west of Acapulco, causing devastation across the city and resulting in $12–16 billion (U.S. dollars) in property damage and at least 52 fatalities. The storm's extremely rapid intensification was poorly predicted by dynamical and statistical models. The official forecast from the National Hurricane Center (NHC) around 24 hours prior to landfall called for Otis to peak at Category 1 strength on the Saffir-Simpson Hurricane Wind Scale (64 kt–82 kt; 34 m s^{-1}–42 m s^{-1}). The explosive strengthening and lack of forecast warning led to a "nightmare scenario" for the Acapulco metropolitan area per the NHC forecast discussion[7] issued at 0300 UTC on 25 October.

This sidebar discusses the meteorological history of Otis, including some of the records that the storm achieved during its lifetime and the damage that the storm caused. Eastern North Pacific hurricane records from 1971 to 2022 are taken from the NHC's hurricane database (e.g., HURDAT2; Landsea and Franklin 2013)[8]. Otis' observed values are taken from the NHC's Tropical Cyclone Report on the storm (Reinhart and Reinhart 2024).

Otis formed from an area of low pressure off the west coast of Mexico, becoming a tropical depression at 1200 UTC on 22 October and intensifying to a tropical storm six hours later. Over the next 24 hours, the system strengthened slowly from 35 kt (18 m s^{-1}) to 45 kt (23 m s^{-1}) as it meandered northward. While Otis was tracking over ~29°C–30°C sea-surface temperatures during this time, it also was battling moderate levels of easterly vertical wind shear which left the center of the circulation somewhat exposed. Continued easterly shear checked Otis' intensification rate through 0600 UTC on 24 October, at which time sustained winds had reached 55 kt (28 m s^{-1}). In the next 24 hours, vertical wind shear relaxed, and the system responded by undergoing one of the strongest 24-hour rapid intensification episodes on record in the eastern North Pacific, intensifying from a 55-kt (28-m s^{-1}) tropical storm to a 145-kt (75-m s^{-1}) Category 5 hurricane. Otis weakened slightly before landfall, making landfall at 0645 UTC with maximum sustained winds of 140 kt (72 m s^{-1}; Fig. SB4.1). The storm dissipated quickly after landfall, weakening to a tropical storm by 1800 UTC on 25 October and degenerating into a remnant low over the mountainous terrain of western Mexico three hours later.

Hurricane Otis' 24-hour increase in intensity of 90 kt (46 m s^{-1}) tied with Hurricane Linda (1997) for the second-most intensification in a 24-hr period for an eastern North Pacific tropical cyclone on record (since 1971), lagging only Hurricane Patricia's (2015) 24-hour increase of 105 kt (54 m s^{-1}). Otis also intensified by 65 kt (31 m s^{-1}) in 12 hours, from a Category 1 hurricane (65 kt; 33 m s^{-1}) at 1200 UTC on 24 October to a Category 4 hurricane (130 kt; 67 m s^{-1}) at 0000 UTC on 25 October. This tied Hurricane Patricia for the strongest 12-hour intensification rate in the eastern North Pacific on record (65 kt; 33 m s^{-1}). Otis' maximum intensity of 145 kt (75 m s^{-1}) reached on 25 October tied with Hurricane Kenna (2002) for the strongest eastern North Pacific hurricane that late in the calendar year on record. As noted earlier, Otis was the strongest hurricane on record to make landfall on the west coast of Mexico (140 kt; 72 m s^{-1}). It was also the fifth Category 5 hurricane since 1950 to make landfall in mainland Mexico, joining Atlantic Hurricanes Janet (1955), Anita (1977), Gilbert (1988), and Dean (2007).

In Acapulco and the surrounding region of Guerrero, Otis inflicted catastrophic damage to most structures, including many hotels and high-rise buildings as well as downing and defoliating trees and causing severe rainfall-related flooding and mudslides. Windows and interior walls were blown out of most high-rise buildings and luxury hotels (e.g., Fig. SB4.2), resulting in catastrophic impacts to the city's tourism-based economy. Damage was also reported at many hospitals and medical clinics. Several electrical substations and a power plant were also heavily damaged, and thousands of utility poles were destroyed, resulting in widespread power and internet communication outages across the region. Storm
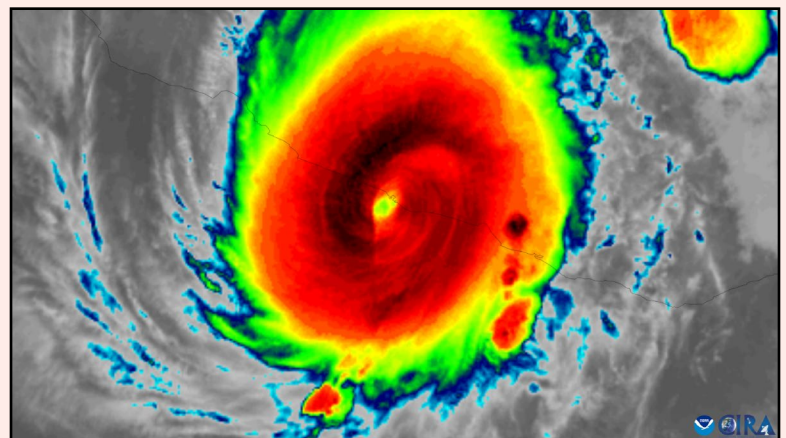

Fig. SB4.1. GOES-18 infrared satellite image of Hurricane Otis near the time of its landfall at 0610 UTC on 25 October 2023. (Image credit: NOAA/CIRA.)

[7] https://www.nhc.noaa.gov/archive/2023/ep18/ep182023.discus.012.shtml?
[8] https://www.nhc.noaa.gov/data/hurdat/hurdat2-nepac-1949-2022-050423.txt

surge and waves resulted in extensive damage to vessels and marina infrastructure exacerbated by the very short preparation time to secure property.

Mudslides on the outskirts of the city in mountainous terrain combined with severe winds caused more loss of life and the complete destruction of many private dwellings. The flooding and mudslides also blocked major highways, including the Mexico City-to-Acapulco "Highway of the Sun," preventing crews from traveling to the city to provide aid. Acapulco's commercial and military airports were also badly damaged, further hampering relief efforts. As noted earlier, Otis caused $12–16 billion (U.S. dollars) in damage. To put this damage in perspective, Mexico's Gross Domestic Product (GDP) is $1.3 trillion (U.S. dollars), and Otis' damage was approximately 1% of the Mexican GDP. For comparison, the costliest storm in U.S. history was Hurricane Katrina in (2005), which caused damage totaling $195 billion (U.S. dollars), equivalent to about 0.6% of the U.S.' GDP.

Hurricane Otis merits further study in multiple scientific and social dimensions. Operational intensity forecast errors were near recent upper bounds, with 48- and 24-hour projections underestimating Otis' 145 kt (75 m s^{-1}) peak maximum sustained winds by 95 kt (49 m s^{-1}) and 70 kt (36 m s^{-1}), respectively. This explosive intensification was coupled with an accelerated track towards a densely populated urban area, limiting the effective preparation window in Acapulco for hurricane-force winds to a day or less. Otis is also the first instance of the most intense portion of a Category 5 hurricane making landfall at near-peak intensity with a coastal area that has large-scale multistory structures, resulting in widespread, catastrophic structural damage. The wind profile power law and the observational height adjustments from Franklin et al. (2003) both suggest one-minute sustained winds atop the 100 m–125 m residential towers in eastern Acapulco likely reached at least 165 kt (85 m s^{-1}), with possible three-second gusts of 190 kt–200 kt (98 m s^{-1}–103 m s^{-1}). The extraordinary wind stresses and resulting destruction observed during Otis may hold valuable lessons for improving the resilience of coastal structures. Additionally, this earthquake-prone area of Mexico may also have unique building codes that, while well-suited to minimizing earthquake damage, might provide some challenges for those same structures in withstanding high winds from hurricanes, as documented in Crosti et al. (2011), which notes that while seismic design explicitly allows for inelastic behavior, it is in opposition to the requirements for high-wind design. This is certainly an issue for structural engineers to consider in compound-risk areas that are undoubtedly not limited to the Mexican coast.

Fig. SB4.2. (a) Before and (b) after view of high-rise buildings and surrounding vegetation highlighting the severe wind impacts from Hurricane Otis in Acapulco, Mexico. (Photo credit: Parvez 2023.)

Sidebar 4.2: Tropical Cyclone Freddy: The world's longest-lived tropical cyclone
B. TREWIN, C. EARL-SPURR, AND R. CERVENY

Tropical Cyclone Freddy in February and March 2023 was the world's longest-lived tropical cyclones (TCs) on record. It crossed the full width of the Indian Ocean, the first time since 2000 that a cyclone that formed in the Australian region made landfall on the mainland African coast. Freddy made three landfalls in total: one in Madagascar and two in Mozambique.

Freddy was first identified south of Bali (Indonesia) on 5 February. It reached TC intensity at 0600 UTC on 6 February at 12.3°S, 118.8°E, to the north of Broome in Western Australia. The storm then took a generally westward track, reaching an initial intensity peak on 11 February with maximum sustained one-minute winds of 115 kt (59 m s^{-1}), according to the Joint Typhoon Warning Center (making it a Category 4 system on the Australian scale), near 15°S, 102°E.

On 14 February, Freddy crossed the 90°E meridian into the southwest Indian Ocean basin. It intensified over the next few days, reaching its peak intensity on 19 February near 18°S, 62°E with maximum one-minute sustained winds of 140 kt (72 m s^{-1}), a Category 5 system on the Saffir-Simpson scale. It passed north of Mauritius and La Réunion on 20 February, still close to maximum intensity.

Freddy's first landfall was at about 1800 UTC on 21 February, near Mananjary on the east coast of Madagascar. The storm weakened somewhat before landfall but was still a significant cyclone at this point, with maximum one-minute sustained winds of 90 kt (46 m s^{-1}). The cyclone rapidly weakened over land while crossing Madagascar, but quickly re-intensified as it crossed the Mozambique Channel, making a second landfall near Vilankulos, Mozambique, on 24 February with maximum one-minute sustained winds of 60 kt (31 m s^{-1}).

Although it dropped below cyclone intensity, the system remained organized over land and re-emerged over the Mozambique Channel on 1 March, re-intensifying to become a cyclone again. It remained slow-moving over the Mozambique Channel, intensifying to reach maximum one-minute sustained winds of at least 95 kt (49 m s^{-1}) on two separate days, 7 and 11 March. The second of these maximum gusts occurred as it was moving northwest to make its final landfall near Quelimane, Mozambique, on 11 March. The storm weakened only slightly before landfall, which occurred with maximum one-minute sustained winds of 95 kt (49 m s^{-1}). The system then moved northwest as a remnant low, falling below cyclone intensity on 12 March and dissipating altogether by 14 March.

The major impacts of Freddy occurred as a result of flooding during and after the final landfall, both in Mozambique and Malawi, as extremely heavy rain fell (up to 672 mm in Mozambique) over the period of its landfalls. In some cases, one month's worth of rainfall fell in a single day, and six months of rain fell within six days. Malawi was especially hard hit with at least 679 deaths reported, according to the International Disaster Database EM-DAT. A further 165 deaths were reported in Mozambique, which had also experienced substantial flooding and wind damage during Freddy's first landfall. Casualties were also reported in Madagascar and Zimbabwe and at sea near Mauritius. In total, Severe Tropical Cyclone Freddy resulted in over 1400 fatalities and caused damage exceeding $655 million (U.S. dollars), making it the second-costliest tropical cyclone on record in the south Indian Ocean basin (Aon 2024).

A World Meteorological Organization expert committee recently confirmed that Freddy should be classified as the world's longest-lived tropical cyclone, and had the second longest track after Hurricane John in 1994 (Earl-Spurr et al. 2024). The system's total lifetime was clearly longer than that of the existing record holder, Hurricane John (which lasted for about 30 days in the northeast Pacific in August and September 1994), and even after periods over land when Freddy dropped below tropical cyclone intensity were discounted, it was at tropical cyclone strength for substantially longer than John's total lifetime.
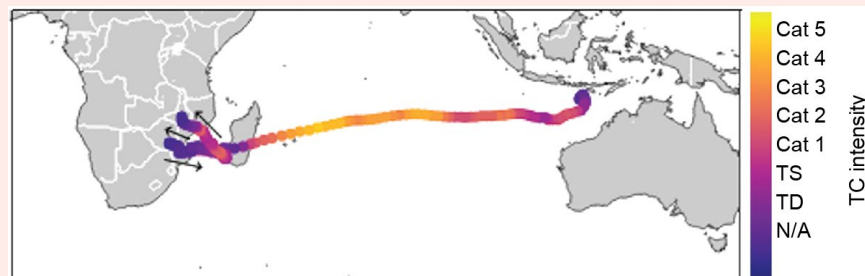

Fig. SB4.3. Cyclone Freddy storm track from 2 to 24 February 2023. Saffir-Simpson storm intensities along the track are indicated by the color scale.

Appendix 1: Acronyms

ACE accumulated cyclone energy
AMO Atlantic Multi-decadal Oscillation
ASO August–October
AUSSM Australian summer monsoon
CMORPH Climate Prediction Center Morphing technique
CNP Central North Pacific
DJF December–February
EASM East Asian summer monsoon
ENP Eastern North Pacific
ENSO El Niño–Southern Oscillation
GDP gross domestic product
HTC hurricane/typhoon/cyclone
IBTrACS International Best Track Archive for Climate Stewardship
IO Indian Ocean
IOB Indian Ocean basin
IOD Indian Ocean Dipole
IODE Eastern Indian Ocean Dipole
IODW Western Indian Ocean Dipole
ISM Indian summer monsoon
ISM Indian summer monsoon
ITCZ Intertropical Convergence Zone
JASO July–October
JJA June–August
JMA Japan Meteorological Agency
JTWC Joint Typhoon Warning Center
LMR Land Monsoon rainfall
MAM March–May
MDR Main Development Region
MJO Madden-Julian Oscillation
MSLP mean sea-level pressure
MSWEP Multi-Source Weighted-Ensemble Precipitation
NA North Atlantic
NAFSM northern African summer monsoon
NASM North American summer monsoon
NCAR National Center for Atmospheric Research
NCEP National Centers for Environmental Prediction
NH Northern Hemisphere
NHC National Hurricane Center
NIO North Indian Ocean
nIOD negative Indian Ocean Dipole
NOAA GlobalTemp NOAA Merged Land Ocean Global Surface Temperature Analysis
OISST Optimum Interpolation Sea Surface Temperature
OLR outgoing longwave radiation
ONI Oceanic Niño Index
PAGASA Philippine Atmospheric, Geophysical and Astronomical Services Administration
pIOD positive Indian Ocean Dipole
RMM Real-time Multivariate Madden-Julian Oscillation

RSMC	Regional Specialized Meteorological Center
SA	South Atlantic
SAFSM	southern African summer monsoon
SAM	Southern Annular Mode
SASM	South American summer monsoon
SH	Southern Hemisphere
SIO	South Indian Ocean
SON	September–November
SPCZ	South Pacific Convergence Zone
SSHWS	Saffir-Simpson Hurricane Wind Scale
SST	sea-surface temperature
SSTA	sea-surface temperature anomaly
TC	tropical cyclone
TCHP	tropical cyclone heat potential
WMO	World Meteorological Organization
WNP	Western North Pacific
WNPSM	western North Pacific summer monsoon

Appendix 2: Datasets and sources

Section 4b ENSO and the tropical Pacific			
Sub-section	**General Variable or Phenomenon**	**Specific dataset or variable**	**Source**
4b	Sea Surface Temperature	ERSSTv5	https://doi.org/10.7289/V5T72FNM
4b1	Sea Surface Temperature	NOAA Optimum Interpolation SST (OISST) v2.1	https://www.ncei.noaa.gov/products/optimum-interpolation-sst
4b1	Subsurface ocean temperature	Global Ocean Data Assimilation System (GODAS, Behringer 2007)	https://www.cpc.ncep.noaa.gov/products/GODAS/
4b2	Outgoing longwave radiation	NCEP CPC OLR (Liebmann and Smith, 1996)	https://www.cpc.ncep.noaa.gov/products/global_precip/html/wpage.olr.html
4b2	wind vectors/wind speed	NCEP NCAR reanalysis 1	https://psl.noaa.gov/data/gridded/data.ncep.reanalysis.html

Section 4c Tropical Intraseasonal Activity			
Sub-section	**General Variable or Phenomenon**	**Specific dataset or variable**	**Source**
4c	Outgoing longwave radiation	HIRS OLR (Schreck et al. 2018)	https://www.ncei.noaa.gov/access/metadata/landing-page/bin/iso?id=gov.noaa.ncdc:C00875
4c	wind velocity potential anomalies	Climate Forecast System Reanalysis (CFSR)	https://climatedataguide.ucar.edu/climate-data/climate-forecast-system-reanalysis-cfsr
4c	Subsurface ocean heat content	Global Ocean Data Assimilation System (GODAS, Behringer et al. 1998)	https://www.cpc.ncep.noaa.gov/products/GODAS/

Section 4d Intertropical Convergence Zone			
Sub-section	**General Variable or Phenomenon**	**Specific dataset or variable**	**Source**
4d1	Precipitation	Multisource weighted ensemble precipitation (MSWEP v2.8.0)	https://www.gloh2o.org/mswep/
4d2	Sea level pressure	NCEP NCAR reanalysis 1	https://psl.noaa.gov/data/gridded/data.ncep.reanalysis.html
4d2	Precipitation	CPC Morphing technique (CMORPH)	https://www.ncei.noaa.gov/products/climate-data-records/precipitation-cmorph
4d2	Outgoing Longwave Radiation	NCEP CPC OLR (Liebmann and Smith, 1996)	https://www.cpc.ncep.noaa.gov/products/global_precip/html/wpage.olr.html
4d2	Sea Surface Temperature	NOAA Optimum Interpolation SST (OISST) v2.1	https://www.ncei.noaa.gov/products/optimum-interpolation-sst

Section 4e Global Monsoon Summary

Sub-section	General Variable or Phenomenon	Specific dataset or variable	Source
4e	Precipitation	Global Precipitation Climatology Project (GPCP)	https://www.ncei.noaa.gov/products/climate-data-records/precipitation-gpcp-monthly
4e	Sea Surface Temperature	ERSSTv5	https://doi.org/10.7289/V5T72FNM
4e	Sea Surface Temperature	HadISST	https://www.metoffice.gov.uk/hadobs/hadisst/
4e	Wind, [Near] Surface	ERA5	https://www.ecmwf.int/en/forecasts/dataset/ecmwf-reanalysis-v5
4e	Wind, Upper Atmosphere	ERA5	https://www.ecmwf.int/en/forecasts/dataset/ecmwf-reanalysis-v5

Section 4f Indian Ocean Dipole

Sub-section	General Variable or Phenomenon	Specific dataset or variable	Source
4f	Precipitation	Climate Prediction Center (CPC) Merged Analysis of Precipitation (CMAP)	https://www.cpc.ncep.noaa.gov/products/global_precip/html/wpage.cmap.html
4f	Sea Surface Temperature	NOAA Optimum Interpolation SST (OISST) v2	https://www.ncei.noaa.gov/products/optimum-interpolation-sst
4f	Wind, [Near] Surface	JRA-55 Atmospheric Reanalysis	http://jra.kishou.go.jp/JRA-55/index_en.html

Section 4g Tropical Cyclones

Sub-section	General Variable or Phenomenon	Specific dataset or variable	Source
4g1, 4g2, 4g3, 4g5, 4g6, 4g7	Tropical Cyclone Data	International Best Track Archive for Climate Stewardship (IBTrACS)	https://www.ncei.noaa.gov/products/international-best-track-archive
4g2	Tropical Cyclone Data	Hurdat2	www.aoml.noaa.gov/hrd/hurdat/Data_Storm.html
4g2, 4g4	Sea Surface Temperature	ERSSTv5	https://doi.org/10.7289/V5T72FNM
4g2	Outgoing Longwave Radiation	NCEP CPC OLR (Liebmann and Smith, 1996)	https://www.cpc.ncep.noaa.gov/products/global_precip/html/wpage.olr.html
4g2, 4g4	Wind, [Near] Surface	ERA5	https://www.ecmwf.int/en/forecasts/dataset/ecmwf-reanalysis-v5

Sub-section	General Variable or Phenomenon	Specific dataset or variable	Source
4g3, 4g5, 4g6	Sea Surface Temperature	NOAA Optimum Interpolation SST (OISST) v2	https://www.ncei.noaa.gov/products/optimum-interpolation-sst
4g3, 4g5, 4g6	Wind, [Near] Surface	Climate Forecast System Reanalysis (CFSR)	https://climatedataguide.ucar.edu/climate-data/climate-forecast-system-reanalysis-cfsr
4g3, 4g5	Outgoing longwave radiation	HIRS OLR (Schreck et al. 2018)	https://www.ncei.noaa.gov/access/metadata/landing-page/bin/iso?id=gov.noaa.ncdc:C00875
4g4	Tropical Cyclone Data	RSMC-Tokyo, JMA best-track data	www.jma.go.jp/jma/jma-eng/jma-center/rsmc-hp-pub-eg/besttrack.html
4g4	Tropical Cyclone Data	Joint Typhoon Warning Center (JTWC) best-track database	https://www.metoc.navy.mil/jtwc/jtwc.html?best-tracks
4g6	Temperature, [Near] Surface	GHCNDEX	www.climdex.org/
4g8	Tropical Cyclone Data	Southwest Pacific Enhanced Archive of Tropical Cyclones (SPEArTC)	https://apdrc.soest.hawaii.edu/projects/speartc/

| Sidebar 4.1 Hurricane Otis: The strongest landfalling hurricane on record for the west coast of Mexico			
Sub-section	General Variable or Phenomenon	Specific dataset or variable	Source
SB4.1	Tropical Cyclone Data	Hurdat2	www.aoml.noaa.gov/hrd/hurdat/Data_Storm.html
SB4.1	Tropical Cyclone Data	National Hurricane Center (NHC) operational b-decks	https://ftp.nhc.noaa.gov/atcf/btk/

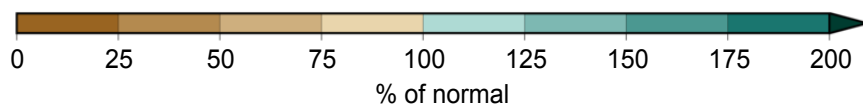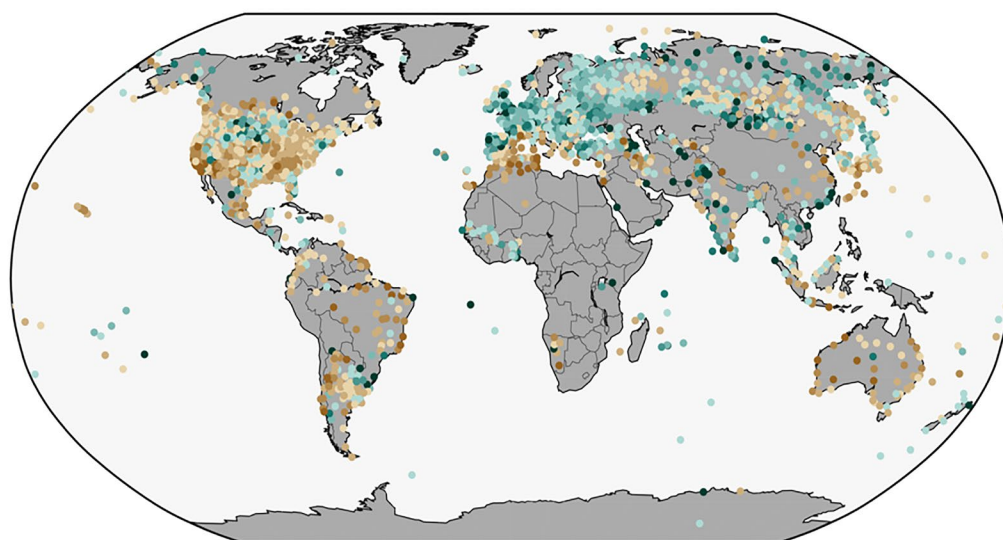| Sidebar 4.2 Tropical Cyclone Freddy—the world's longest-lived tropical cyclones			
Sub-section	General Variable or Phenomenon	Specific dataset or variable	Source
SB4.2	Tropical Cyclone Data	Joint Typhoon Warning Center (JTWC) best-track database	https://www.metoc.navy.mil/jtwc/jtwc.html?best-tracks

Appendix 3: Supplemental materials

(a) Jun–Aug 2023
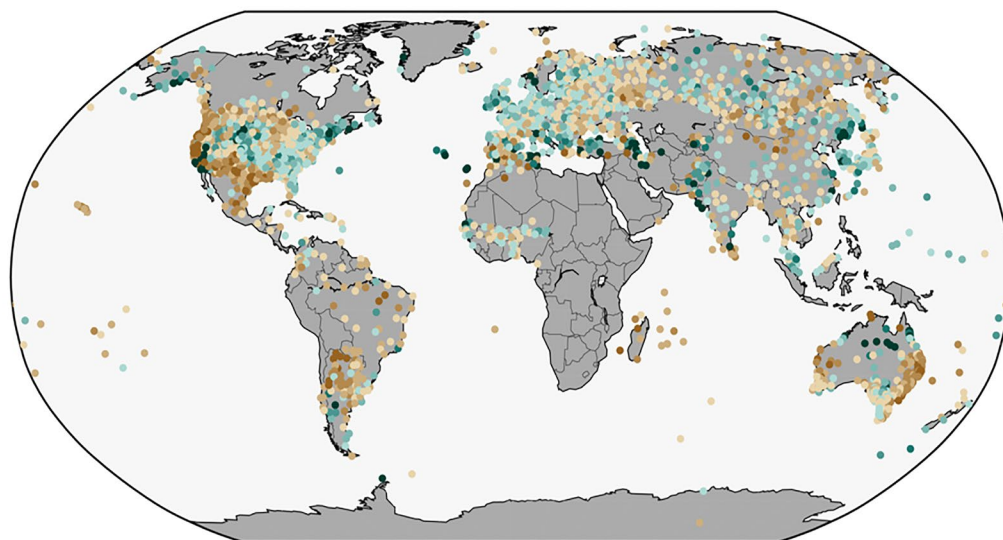
(b) Sep–Nov 2023

% of normal

Appendix Fig. A4.1. Land-only precipitation (% of normal) during (a) Jun–Aug 2023 and (b) Sep–Nov 2023 (relative to a 1961–90 base period). (Sources: figure provided by NOAA NCEI, with data from GHCN-M version 4beta [Menne et al. 2017].)

References

Aiyyer, A., and J. Molinari, 2008: MJO and tropical cyclogenesis in the Gulf of Mexico and eastern Pacific: Case study and idealized numerical modeling. *J. Atmos. Sci.*, **65**, 2691–2704, https://doi.org/10.1175/2007JAS2348.1.

Aon, 2024: Climate and catastrophe insight report. Aon, 118 pp., https://assets.aon.com/-/media/files/aon/reports/2024/climate-and-catastrophe-insights-report.pdf.

Balaguru, K., P. Chang, R. Saravanan, L. R. Leung, Z. Xu, M. Li, and J. S. Hsieh, 2012: Ocean barrier layers' effect on tropical cyclone intensification. *Proc. Natl. Acad. Sci. USA*, **109**, 14 343–14 347, https://doi.org/10.1073/pnas.1201364109.

Banzon, V. F., and R. W. Reynolds, 2013: Use of WindSat to extend a microwave-based daily optimum interpolation sea surface temperature time series. *J. Climate*, **26**, 2557–2562, https://doi.org/10.1175/JCLI-D-12-00628.1.

Beck, H. E., E. F. Wood, M. Pan, C. K. Fisher, D. G. Miralles, A. I. J. M. van Dijk, T. R. McVicar, and R. F. Adler, 2019: MSWEP V2 Global 3-hourly 0.1° precipitation: Methodology and quantitative assessment. *Bull. Amer. Meteor. Soc.*, **100**, 473–500, https://doi.org/10.1175/BAMS-D-17-0138.1.

Behringer, D. W., 2007: The Global Ocean Data Assimilation System (GODAS) at NCEP. 11th Symp. on Integrated Observing and Assimilation Systems for Atmosphere, Oceans, and Land Surface, San Antonio, TX, Amer. Meteor. Soc., 3.3, http://ams.confex.com/ams/87ANNUAL/techprogram/paper_119541.htm.

——, M. Ji, and A. Leetmaa, 1998: An improved coupled model for ENSO prediction and implications for ocean initialization. Part I: The ocean data assimilation system. *Mon. Wea. Rev.*, **126**, 1013–1021, https://doi.org/10.1175/1520-0493(1998)126<1013:AICMFE>2.0.CO;2.

Bell, G. D., and M. Chelliah, 2006: Leading tropical modes associated with interannual and multi-decadal fluctuations in North Atlantic hurricane activity. *J. Climate*, **19**, 590–612, https://doi.org/10.1175/JCLI3659.1.

——, and Coauthors, 2000: The 1999 North Atlantic Hurricane season [in "Climate Assessment for 1999"]. *Bull. Amer. Meteor. Soc.*, **81** (6), S19–S22, https://doi.org/10.1175/1520-0477(2000)81[s1:CAF]2.0.CO;2.

——, E. Blake, C. Landsea, K. Mo, R. Pasch, M. Chelliah, and S. Goldenberg, 2006: Atlantic basin [in "State of the Climate in 2005"]. *Bull. Amer. Meteor. Soc.*, **87** (6), S33–S37, https://doi.org/10.1175/1520-0477-87.6.S1.

——, ——, C. W. Landsea, C. Wang, J. Schemm, T. Kimberlain, R. J. Pasch, and S. B. Goldenberg, 2017: Atlantic basin [in "State of the Climate in 2016"]. *Bull. Amer. Meteor. Soc.*, **98** (8), S108–S112, https://doi.org/10.1175/2017BAMSStateoftheClimate.1.

——, ——, ——, S. B. Goldenberg, and R. J. Pasch, 2018: Atlantic basin [in "State of the Climate in 2017"]. *Bull. Amer. Meteor. Soc.*, **99** (8), S114–S118, https://doi.org/10.1175/2018BAMSStateoftheClimate.1.

——, ——, ——, H. Wang, S. B. Goldenberg, and R. J. Pasch 2019: Atlantic basin [in "State of the Climate in 2018"]. *Bull. Amer. Meteor. Soc.*, **100** (9), S113–S119, https://doi.org/10.1175/2019BAMSStateoftheClimate.1.

——, E. S. Blake, C. W. Landsea, M. Rosencrans, H. Wang, S. B. Goldenberg, and R. J. Pasch, 2020: Atlantic basin [in "State of the Climate in 2019"]. *Bull. Amer. Meteor. Soc.*, **101** (7), S204–S212, https://doi.org/10.1175/BAMS-D-20-0077.1.

Berg, R., 2024: Tropical cyclone report: Tropical Storm Max (EP162023). NHC NHC Tropical Cyclone Rep., 20 pp., https://www.nhc.noaa.gov/data/tcr/EP162023_Max.pdf.

Bjerknes, J., 1969: Atmospheric teleconnections from the equatorial Pacific. *Mon. Wea. Rev.*, **97**, 163–172, https://doi.org/10.1175/1520-0493(1969)097<0163:ATFTEP>2.3.CO;2.

Blake, E. S., 2024: Tropical cyclone report: Hurricane Beatriz (EP022023). NHC Tropical Cyclone Rep., 17 pp., https://www.nhc.noaa.gov/data/tcr/EP022023_Beatriz.pdf.

Camargo, S. J., and A. H. Sobel, 2005: Western North Pacific tropical cyclone intensity and ENSO. *J. Climate*, **18**, 2996–3006, https://doi.org/10.1175/JCLI3457.1.

——, A. W. Robertson, S. J. Gaffney, P. Smyth, and M. Ghil, 2007a: Cluster analysis of typhoon tracks: Part II: Large-scale circulation and ENSO. J. Climate, **20**, 3654–3676, https://doi.org/10.1175/JCLI4203.1.

——, K. A. Emanuel, and A. H. Sobel, 2007b: Use of a genesis potential index to diagnose ENSO effects on tropical cyclone genesis. *J. Climate*, **20**, 4819–4834, https://doi.org/10.1175/JCLI4282.1.

Chan, J. C. L., and K. S. Liu, 2002: Recent decrease in the difference in tropical cyclone occurrence between the Atlantic and the western North Pacific. *Adv. Atmos. Sci.*, **39**, 1387–1397.

Chen, L., and J.-J. Luo, 2021: Indian Ocean dipole and unique Indian Ocean basin warming in 2020 [in "State of the climate in 2020"]. *Bull. Amer. Meteor. Soc.*, **102** (8), S220–S222, https://doi.org/10.1175/BAMS-D-21-0080.1.

——, and ——, 2022: Indian Ocean dipole [in "State of the Climate in 2021"]. *Bull. Amer. Meteor. Soc.*, **103** (8), S213–S217, https://doi.org/10.1175/BAMS-D-22-0069.1.

Chia, H. H., and C. F. Ropelewski, 2002: The interannual variability in the genesis location of tropical cyclones in the northwest Pacific. *J. Climate*, **15**, 2934–2944, https://doi.org/10.1175/1520-0442(2002)015<2934:TIVITG>2.0.CO;2.

Courtney, J., and Coauthors, 2012: Documentation and verification of the world extreme wind gust record: 113.3 m s^{-1} on Barrow Island, Australia, during passage of tropical cyclone Olivia. *Aust. Meteor. Oceanogr. J.*, **62**, 1–9, https://doi.org/10.22499/2.6201.001.

Crosti, C., D. Duthinh, and E. Simiu, 2011: Risk consistency and synergy in multihazard design. *J. Struct. Eng.*, **137**, 844–849, https://doi.org/10.1061/(ASCE)ST.1943-541X.0000335.

Dare, R. A., and J. L. McBride, 2011: Sea surface temperature response to tropical cyclones. *Mon. Wea. Rev.*, **139**, 3798–3808, https://doi.org/10.1175/MWR-D-10-05019.1.

Diamond, H. J.,,, and C. J. Schreck III, Eds., 2022: The tropics [in "State of the Climate in 2021"]. *Bull. Amer. Meteor. Soc.*, **103** (8), S193–S256, https://doi.org/10.1175/BAMS-D-22-0069.1.

——, and ——, Eds., 2023: The tropics [in "State of the Climate in 2022"]. *Bull. Amer. Meteor. Soc.*, **104** (8), S207–S270, https://doi.org/10.1175/BAMS-D-23-0078.1.

——, A. M. Lorrey, K. R. Knapp, and D. H. Levinson, 2012: Development of an enhanced tropical cyclone tracks database for the Southwest Pacific from 1840 to 2011. *Int. J. Climatol.*, **32**, 2240–2250, https://doi.org/10.1002/joc.2412.

Ding, Q., E. J. Steig, D. S. Battisti, and J. M. Wallace, 2012: Influence of the tropics on the southern annular mode. *J. Climate*, **25**, 6330–6348, https://doi.org/10.1175/JCLI-D-11-00523.1.

Domingues, R., and Coauthors, 2015: Upper ocean response to Hurricane Gonzalo (2014): Salinity effects revealed by targeted and sustained underwater glider observations. *Geophys. Res. Lett.*, **42**, 7131–7138, https://doi.org/10.1002/2015GL065378.

Dube, S. K., D. Rao, P. C. Sinha, T. S. Murty, and N. Bahuluyan, 1997: Storm surge in the Bay of Bengal and Arabian Sea: The problem and its prediction. *Mausam*, **48**, 283–304, https://doi.org/10.54302/mausam.v48i2.4012.

Earl-Spurr, C., and Coauthors, 2024: New WMO certified tropical cyclone duration extreme: TC Freddy (04 February to 14 March 2023) lasting for 36 days. *Bull. Amer. Meteor. Soc.*, in press, https://doi.org/10.1175/BAMS-D-24-0071.1.

Ebita, A., and Coauthors, 2011: The Japanese 55-Year Reanalysis "JRA-55": An interim report. *SOLA*, **7**, 149–152, https://doi.org/10.2151/sola.2011-038.

Emanuel, K. A., 1988: The maximum intensity of hurricanes. *J. Atmos. Sci.*, **45**, 1143–1155, https://doi.org/10.1175/1520-0469(1988)045<1143:TMIOH>2.0.CO;2.

——, and D. S. Nolan, 2004: Tropical cyclone activity and the global climate system. 26th Conf. on Hurricanes and Tropical Meteorology, Miami, FL, Amer. Meteor. Soc., 10A.2, https://ams.confex.com/ams/26HURR/techprogram/paper_75463.htm.

Enfield, D. B., and A. M. Mestas-Nuñez, 1999: Multiscale variabilities in global sea surface temperatures and their relationships with tropospheric climate patterns. *J. Climate*, **12**, 2719–2733, https://doi.org/10.1175/1520-0442(1999)012<2719:MVIGSS>2.0.CO;2.

Franklin, J. L., M. L. Black, and K. Valde, 2003: GPS dropwindsonde wind profiles in hurricanes and their operational implications. *Wea. Forecasting*, **18**, 32–44, https://doi.org/10.1175/1520-0434(2003)018<0032:GDWPIH>2.0.CO;2.

Gallagher Re, 2024: Natural Catastrophe and Climate Report: 2023. 76 pp., https://www.ajg.com/gallagherre/news-and-insights/2024/january/2023-natural-catastrophe-and-climate-report/.

Goldenberg, S. B., and L. J. Shapiro, 1996: Physical mechanisms for the association of El Niño and West African rainfall with Atlantic major hurricane activity. *J. Climate*, **9**, 1169–1187, https://doi.org/10.1175/1520-0442(1996)009<1169:PMFTAO>2.0.CO;2.

——, C. W. Landsea, A. M. Mestas-Nuñez, and W. M. Gray, 2001: The recent increase in Atlantic hurricane activity: Causes and implications. *Science*, **293**, 474–479, https://doi.org/10.1126/science.1060040.

Goni, G. J., and Coauthors, 2009: Applications of satellite-derived ocean measurements to tropical cyclone intensity forecasting. *Oceanography*, **22** (3), 190–197, https://doi.org/10.5670/oceanog.2009.78.

——, and Coauthors, 2017: Autonomous and Lagrangian ocean observations for Atlantic tropical cyclone studies and forecasts. *Oceanography*, **30** (2), 92–103, https://doi.org/10.5670/oceanog.2017.227.

Gray, W. M., 1984: Atlantic seasonal hurricane frequency. Part I: El Niño and 30 mb quasi-biennial oscillation influences. *Mon. Wea. Rev.*, **112**, 1649–1668, https://doi.org/10.1175/1520-0493(1984)112<1649:ASHFPI>2.0.CO;2.

——, 1990: Strong association between West African rainfall and U.S. landfall of intense hurricanes. *Science*, **249**, 1251–1256, https://doi.org/10.1126/science.249.4974.1251.

Guo, Y., X. Jiang, and D. E. Waliser, 2014: Modulation of the convectively coupled Kelvin waves over South America and the tropical Atlantic Ocean in association with the Madden–Julian oscillation. *J. Atmos. Sci.*, **71**, 1371–1388, https://doi.org/10.1175/JAS-D-13-0215.1.

Hastenrath, S., 1990: Decadal-scale changes of the circulation in the tropical Atlantic sector associated with Sahel drought. *Int. J. Climatol.*, **10**, 459–472, https://doi.org/10.1002/joc.3370100504.

Hersbach, H., and Coauthors, 2020: The ERA5 global reanalysis. *Quart. J. Roy. Meteor. Soc.*, **146**, 1999–2049, https://doi.org/10.1002/qj.3803.

Hong, C.-C., T. Li, and J.-J. Luo, 2008: Asymmetry of the Indian Ocean dipole. Part II: Model diagnosis. *J. Climate*, **21**, 4849–4858, https://doi.org/10.1175/2008JCLI2223.1.

Huang, B., and Coauthors, 2017: Extended Reconstructed Sea Surface Temperature, version 5 (ERSSTv5): Upgrades, validations, and intercomparisons. *J. Climate*, **30**, 8179–8205, https://doi.org/10.1175/JCLI-D-16-0836.1.

——, C. Liu, V. Banzon, E. Freeman, G. Graham, B. Hankins, T. Smith, and H.-M. Zhang, 2021: Improvements of the Daily Optimum Interpolation Sea Surface Temperature (DOISST) version 2.1. *J. Climate*, **34**, 2923–2939, https://doi.org/10.1175/JCLI-D-20-0166.1.

Huffman, G., R. F. Adler, D. T. Bolvin, and G. Gu, 2009: Improving the global precipitation record: GPCP version 2.1. *Geophys. Res. Lett.*, **36**, L17808, https://doi.org/10.1029/2009GL040000.

Joyce, R. J., J. E. Janowiak, P. A. Arkin, and P. Xie, 2004: CMORPH: A method that produces global precipitation estimates from passive microwave and infrared data at high spatial and temporal resolution. *J. Hydrometeor.*, **5**, 487–503, https://doi.org/10.1175/1525-7541(2004)005<0487:CAMTPG>2.0.CO;2.

Kalnay, E., and Coauthors, 1996: The NCEP/NCAR 40-Year Reanalysis Project. *Bull. Amer. Meteor. Soc.*, **77**, 437–471, https://doi.org/10.1175/1520-0477(1996)077<0437:TNYRP>2.0.CO;2.

Kiladis, G. N., M. C. Wheeler, P. T. Haertel, K. H. Straub, and P. E. Roundy, 2009: Convectively coupled equatorial waves. *Rev. Geophys.*, **47**, RG2003, https://doi.org/10.1029/2008RG000266.

Knaff, J. A., 1997: Implications of summertime sea level pressure anomalies in the tropical Atlantic region. *J. Climate*, **10**, 789–804, https://doi.org/10.1175/1520-0442(1997)010<0789:IOSSLP>2.0.CO;2.

——, C. R. Sampson, and K. D. Musgrave, 2018: An operational rapid intensification prediction aid for the western North Pacific. *Wea. Forecasting*, **33**, 799–811, https://doi.org/10.1175/WAF-D-18-0012.1.

——, ——, and B. R. Strahl, 2020: A tropical cyclone rapid intensification prediction aid for the Joint Typhoon Warning Center's areas of responsibility. *Wea. Forecasting*, **35**, 1173–1185, https://doi.org/10.1175/WAF-D-19-0228.1.

Knapp, K. R., M. C. Kruk, D. H. Levinson, H. J. Diamond, and C. J. Neumann, 2010: The International Best Track Archive for Climate Stewardship (IBTrACS): Unifying tropical cyclone data. *Bull. Amer. Meteor. Soc.*, **91**, 363–376, https://doi.org/10.1175/2009BAMS2755.1.

——, J. A. Knaff, C. R. Sampson, G. M. Riggio, and A. D. Schnapp, 2013: A pressure-based analysis of the historical western North Pacific tropical cyclone intensity record. *Mon. Wea. Rev.*, **141**, 2611–2631, https://doi.org/10.1175/MWR-D-12-00323.1.

Kumar, A., and Z.-Z. Hu, 2014: Interannual and interdecadal variability of ocean temperature along the equatorial Pacific in conjunction with ENSO. *Climate Dyn.*, **42**, 1243–1258, https://doi.org/10.1007/s00382-013-1721-0.

Landsea, C. W., and J. L. Franklin, 2013: Atlantic hurricane database uncertainty and presentation of a new database format. *Mon. Wea. Rev.*, **141**, 3576–3592, https://doi.org/10.1175/MWR-D-12-00254.1.

——, W. M. Gray, P. W. Mielke, and K. J. Berry, 1992: Long-term variations of western Sahelian monsoon rainfall and intense U.S. landfalling hurricanes. *J. Climate*, **5**, 1528–1534, https://doi.org/10.1175/1520-0442(1992)005<1528:LTVOWS>2.0.CO;2.

——, G. A. Vecchi, L. Bengtsson, and T. R. Knutson, 2010: Impact of duration thresholds on Atlantic tropical cyclone counts. *J. Climate*, **23**, 2508–2519, https://doi.org/10.1175/2009JCLI3034.1.

Leipper, D. F., and D. Volgenau, 1972: Hurricane heat potential of the Gulf of Mexico. *J. Phys. Oceanogr.*, **2**, 218–224, https://doi.org/10.1175/1520-0485(1972)002<0218:HHPOTG>2.0.CO;2.

Liebmann, B., and C. A. Smith, 1996: Description of a complete (interpolated) outgoing longwave radiation dataset. *Bull. Amer. Meteor. Soc.*, **77**, 1275–1277, https://doi.org/10.1175/1520-0477-77.6.1274.

Lin, I. I., and Coauthors, 2013: An ocean coupling potential intensity index for tropical cyclones. *Geophys. Res. Lett.*, **40**, 1878–1882, https://doi.org/10.1002/grl.50091.

——, and Coauthors, 2020: ENSO and tropical cyclones. *El Niño Southern Oscillation in a Changing Climate, Geophys. Monogr.*, Vol. 253, Amer. Geophys. Union, 377–408, https://doi.org/10.1002/9781119548164.ch17.

——, and Coauthors, 2021: A tale of two rapidly-intensifying supertyphoons: Hagibis (2019) and Haiyan (2013). Bull. *Amer. Meteor. Soc.*, **102**, E1645–E1664, https://doi.org/10.1175/BAMS-D-20-0223.1.

Liu, T., J. Li, C. Sun, T. Lian, and Y. Zhang, 2021: Impact of the April–May SAM on central Pacific Ocean sea temperature over the following three seasons. *Climate Dyn.*, **57**, 775–786, https://doi.org/10.1007/s00382-021-05738-4.

——, S. Masson, S. Behera, and T. Yamagata, 2007: Experimental forecasts of the Indian Ocean dipole using a coupled OAGCM. *J. Climate*, **20**, 2178–2190, https://doi.org/10.1175/JCLI4132.1.

——, R. Zhang, S. K. Behera, Y. Masumoto, F.-F. Jin, R. Lukas, and T. Yamagata, 2010: Interaction between El Niño and extreme Indian Ocean dipole. *J. Climate*, **23**, 726–742, https://doi.org/10.1175/2009JCLI3104.1.

——, W. Sasaki, and Y. Masumoto, 2012: Indian Ocean warming modulates Pacific climate change. *Proc. Natl. Acad. Sci. USA*, **109**, 18 701–18 706, https://doi.org/10.1073/pnas.1210239109.

Madden, R., and P. Julian, 1971: Detection of a 40–50 day oscillation in the zonal wind in the tropical Pacific. *J. Atmos. Sci.*, **28**, 702–708, https://doi.org/10.1175/1520-0469(1971)028<0702:DOADOI>2.0.CO;2.

——, and ——, 1972: Description of global-scale circulation cells in the tropics with a 40–50 day period. *J. Atmos. Sci.*, **29**, 1109–1123, https://doi.org/10.1175/1520-0469(1972)029<1109:DOGSCC>2.0.CO;2.

——, and ——, 1994: Observations of the 40–50-day tropical oscillation: A review. *Mon. Wea. Rev.*, **122**, 814–837, https://doi.org/10.1175/1520-0493(1994)122<0814:OOTDTO>2.0.CO;2.

Mainelli, M., M. DeMaria, L. Shay, and G. Goni, 2008: Application of oceanic heat content estimation to operational forecasting of recent Atlantic category 5 hurricanes. *Wea. Forecasting*, **23**, 3–16, https://doi.org/10.1175/2007WAF2006111.1.

Maloney, E. D., and D. L. Hartmann, 2001: The Madden–Julian oscillation, barotropic dynamics, and North Pacific tropical cyclone formation. *Part I: Observations. J. Atmos. Sci.*, **58**, 2545–2558, https://doi.org/10.1175/1520-0469(2001)058<2545:TMJOBD>2.0.CO;2.

Menne, M. J., B. E. Gleason, J. Lawrimore, J. Rennie, and C. N. Williams, 2017: Global Historical Climatology Network – Monthly temperature, version 4 (BETA). NOAA National Centers for Environmental Information, accessed 31 January 2024, https://doi.org/10.7289/V5XW4GTH.

Moreno, P. I., and Coauthors, 2018: Onset and evolution of southern annular mode-like changes at centennial timescale. *Sci. Rep.*, **8**, 3458, https://doi.org/10.1038/s41598-018-21836-6.

Münnich, M., and J. D. Neelin, 2005: Seasonal influence of ENSO on the Atlantic ITCZ and equatorial South America. *Geophys. Res. Lett.*, **32**, L21709, https://doi.org/10.1029/2005GL023900.

NIWA, 2023: Aotearoa New Zealand climate summary: February 2023 (issued 3 March 2023). Accessed 2 February 2024, https://niwa.co.nz/monthly/climate-summary-february-2023.

NOAA, 2023: Climate diagnostics bulletin, September 2023. NOAA, 87 pp., https://www.cpc.ncep.noaa.gov/products/CDB/CDB_Archive_pdf/PDF/CDB.sep2023_color.pdf.

Nobre, P., and J. Shukla, 1996: Variations of sea surface temperature, wind stress and rainfall over the tropical Atlantic and South America. *J. Climate*, **9**, 2464–2479, https://doi.org/10.1175/1520-0442(1996)009<2464:VOSSTW>2.0.CO;2.

Parvez, C. (@ChaudharyParvez), 2023: Residential building in Acapulco, Mexico that was shredded by Category 5 Hurricane Otis's extreme winds. Twitter/X, 28 October 2023, 10:40 p.m., https://twitter.com/ChaudharyParvez/status/1718457833468125236.

Raga, G. B., B. Bracamontes-Ceballos, L. Farfán, and R. Romero-Centeno, 2013: Landfalling tropical cyclones on the Pacific coast of Mexico: 1850–2010. *Atmósfera*, **26**, 209–220, https://doi.org/10.1016/S0187-6236(13)71072-5.

Ramage, C. S., 1971: *Monsoon Meteorology*. Academic Press, 296 pp.

Reinhart, B. J., and A. Reinhart, 2024: Hurricane Otis (EP182023). NHC Tropical Cyclone Rep., 39 pp., https://www.nhc.noaa.gov/data/tcr/EP182023_Otis.pdf.

Reynolds, R. W., N. A. Rayner, T. M. Smith, D. C. Stokes, and W. Wang, 2002: An improved in situ and satellite SST analysis for climate. *J. Climate*, **15**, 1609–1625, https://doi.org/10.1175/1520-0442(2002)015<1609:AIISAS>2.0.CO;2.

Ropelewski, C. F., and M. S. Halpert, 1989: Precipitation patterns associated with the high index phase of the Southern Oscillation. *J. Climate*, **2**, 268–284, https://doi.org/10.1175/1520-0442(1989)002<0268:PPAWTH>2.0.CO;2.

Saha, S., and Coauthors, 2014: The NCEP Climate Forecast System version 2. *J. Climate*, **27**, 2185–2208, https://doi.org/10.1175/JCLI-D-12-00823.1.

Saji, N. H., B. N. Goswami, P. N. Vinayachandran, and T. Yamagata, 1999: A dipole mode in the tropical Indian Ocean. *Nature*, **401**, 360–363, https://doi.org/10.1038/43854.

Schneider, T., T. Bischoff, and G. H. Haug, 2014: Migrations and dynamics of the intertropical convergence zone. *Nature*, **513**, 45–53, https://doi.org/10.1038/nature13636.

Schreck, C. J., 2015: Kelvin waves and tropical cyclogenesis: A global survey. *Mon. Wea. Rev.*, **143**, 3996–4011, https://doi.org/10.1175/MWR-D-15-0111.1.

——, 2016: Convectively coupled Kelvin waves and tropical cyclogenesis in a semi-Lagrangian framework. *Mon. Wea. Rev.*, **144**, 4131–4139, https://doi.org/10.1175/MWR-D-16-0237.1.

——, and J. Molinari, 2011: Tropical cyclogenesis associated with Kelvin waves and the Madden–Julian oscillation. *Mon. Wea. Rev.*, **139**, 2723–2734, https://doi.org/10.1175/MWR-D-10-05060.1.

——, K. R. Knapp, and J. P. Kossin, 2014: The impact of best track discrepancies on global tropical cyclone climatologies using IBTrACS. Mon. *Wea. Rev.*, **142**, 3881–3899, https://doi.org/10.1175/MWR-D-14-00021.1.

——, H.-T. Lee, and K. R. Knapp, 2018: HIRS outgoing longwave radiation —— Daily climate data record: Application toward identifying tropical subseasonal variability. *Remote Sens.*, **10**, 1325, https://doi.org/10.3390/rs10091325.

Shay, L. K., G. J. Goni, and P. G. Black, 2000: Effects of a warm oceanic feature on Hurricane Opal. *Mon. Wea. Rev.*, **128**, 1366–1383, https://doi.org/10.1175/1520-0493(2000)128<1366:EOAWOF>2.0.CO;2.

Trenberth, K. E., 1984: Signal versus noise in the Southern Oscillation. *Mon. Wea. Rev.*, **112**, 326–332, https://doi.org/10.1175/1520-0493(1984)1122.0.CO;2.

Vecchi, G. A., and B. J. Soden, 2007: Effect of remote sea surface temperature change on tropical cyclone potential intensity. *Nature*, **450**, 1066–1070, https://doi.org/10.1038/nature06423.

Ventrice, M. J., C. D. Thorncroft, and M. A. Janiga, 2012a: Atlantic tropical cyclogenesis: A three-way interaction between an African easterly wave, diurnally varying convection, and a convectively coupled atmospheric Kelvin wave. *Mon. Wea. Rev.*, **140**, 1108–1124, https://doi.org/10.1175/MWR-D-11-00122.1.

——, ——, and C. J. Schreck, 2012b: Impacts of convectively coupled Kelvin waves on environmental conditions for Atlantic tropical cyclogenesis. *Mon. Wea. Rev.*, **140**, 2198–2214, https://doi.org/10.1175/MWR-D-11-00305.1.

Villarini, G., G. A. Vecchi, T. R. Knutson, and J. A. Smith, 2011: Is the recorded increase in short duration North Atlantic tropical storms spurious? *J. Geophys. Res.*, **116**, D10114, https://doi.org/10.1029/2010JD015493.

Vincent, D. G., 1994: The South Pacific Convergence Zone (SPCZ): A review. *Mon. Wea. Rev.*, **122**, 1949–1970, https://doi.org/10.1175/1520-0493(1994)122<1949:TSPCZA>2.0.CO;2.

Vose, R. S., and Coauthors, 2021: Implementing full spatial coverage in NOAA's Global Temperature Analysis. *Geophys. Res. Lett.*, **48**, e2020GL090873, https://doi.org/10.1029/2020GL090873.

Waliser, D. E., and C. Gautier, 1993: A satellite-derived climatology of the ITCZ. *J. Climate*, **6**, 2162–2174, https://doi.org/10.1175/1520-0442(1993)006<2162:ASDCOT>2.0.CO;2.

Wang, B., 1994: Climatic regimes of tropical convection and rainfall. *J. Climate*, **7**, 1109–1118, https://doi.org/10.1175/1520-0442(1994)007<1109:CROTCA>2.0.CO;2.

——, and Q. Ding, 2008: Global monsoon: Dominant mode of annual variation in the tropics. *Dyn. Atmos. Ocean*, **44**, 165–183, https://doi.org/10.1016/j.dynatmoce.2007.05.002.

——, J. Liu, H. J. Kim, P. J. Webster, and S. Y. Yim, 2012: Recent change of the global monsoon precipitation (1979–2008). *Climate Dyn.*, **39**, 1123–1135, https://doi.org/10.1007/s00382-011-1266-z.

Wheeler, M., and G. N. Kiladis, 1999: Convectively coupled equatorial waves: Analysis of clouds and temperature in the wavenumber-frequency domain. *J. Atmos. Sci.*, **56**, 374–399, https://doi.org/10.1175/1520-0469(1999)056<0374:CCEWAO>2.0.CO;2.

Wheeler, M. C., and H. H. Hendon, 2004: An all-season real-time multivariate MJO index: Development of an index for monitoring and prediction. *Mon. Wea. Rev.*, **132**, 1917–1932, https://doi.org/10.1175/1520-0493(2004)132<1917:AARMMI>2.0.CO;2.

Wood, K. M., and E. A. Ritchie, 2015: A definition for rapid weakening in the North Atlantic and eastern North Pacific. *Geophys. Res. Lett.*, **42**, 10091–10097, https://doi.org/10.1002/2015GL066697.

——, and C. J. Schreck, 2020: Eastern North Pacific and central North Pacific basins [in "State of the Climate in 2019"]. *Bull. Amer. Meteor. Soc.*, **101** (8), S212–S214, https://doi.org/10.1175/BAMS-D-20-0077.1.

——, and ——, 2021: Eastern North Pacific and central North Pacific basins [in "State of the Climate in 2020"]. *Bull. Amer. Meteor. Soc.*, **102** (8), S233–S235, https://doi.org/10.1175/BAMS-D-21-0080.1.

——, and ——, 2022: Eastern North Pacific and central North Pacific basins [in "State of the Climate in 2021"]. *Bull. Amer. Meteor. Soc.*, **103** (8), S229–S231, https://doi.org/10.1175/BAMS-D-22-0069.1.

——, and ——, 2023: Eastern North Pacific and central North Pacific basins [in "State of the Climate in 2022"]. *Bull. Amer. Meteor. Soc.*, **104** (8), S239–S243, https://doi.org/10.1175/BAMS-D-23-0078.1.

Wu, J., F. Hanjie, L. Shuheng, Z. Wenxiu, S. Yang, S. He, and N. Keenlyside, 2024: Boosting effect of strong western pole of the Indian Ocean dipole on the decay of El Niño events. *npj Climate Atmos. Sci.*, **7**, 6, https://doi.org/10.1038/s41612-023-00554-5.

Yim, S. Y., B. Wang, J. Liu, and Z. W. Wu, 2014: A comparison of regional monsoon variability using monsoon indices. *Climate Dyn.*, **43**, 1423–1437, https://doi.org/10.1007/s00382-013-1956-9.

Zhang, C., 2005: Madden–Julian oscillation. *Rev. Geophys.*, **43**, RG2003, https://doi.org/10.1029/2004RG000158.

Zhao, J. W., R. F. Zhan, Y. Q. Wang, and H. M. Xu, 2018: Contribution of the Interdecadal Pacific oscillation to the recent abrupt decrease in tropical cyclone genesis frequency over the western North Pacific since 1998. *J. Climate*, **31**, 8211–8224, https://doi.org/10.1175/JCLI-D-18-0202.1.

——, ——, ——, S.-P. Xie, and Q. Wu, 2020: Untangling impacts of global warming and interdecadal Pacific Oscillation on long-term variability of North Pacific tropical cyclone track density. *Sci. Adv.*, **6**, eaba6813, https://doi.org/10.1126/sciadv.aba6813.

Zheng, Z.-W., I.-I. Lin, B. Wang, H.-C. Huang, and C.-H. Chen, 2015: A long neglected Rdamper in the El Nino–typhoon relationship: A 'Gaia-like' process. *Sci. Rep.*, **5**, 11103, https://doi.org/10.1038/srep11103.